

**$\beta$ -nucleated isotactic polypropylene  
with different thermomechanical histories  
investigated by synchrotron X-ray**

**Dissertation**

zur Erlangung des akademischen Grades  
Doktor-Ingenieur  
(Dr.-Ing.)

Vorgelegt

**Der Fakultät Maschinenwesen  
der Technischen Universität Dresden**

von

**Jianhong Chen  
Dipl.-Ing.**

geboren am 27.03.1983 in Fujian, China

Tag der Einreichung: 25.09.2014  
Tag der Verteidigung: 10.03.2015

Gutachter: Herr Prof. Dr. rer. nat. habil. G. Heinrich  
Herr Prof. Dr.-Ing. René Androsch

Vorsitzender der  
Prüfungskommission: Herr Prof. Dr.-Ing. Maik Gude

## Abstract

Isotactic polypropylene (iPP), as one of the most versatile commodity thermoplastic polymers, is a polymorphic material having several crystal modifications, among which the  $\beta$ -form exhibits higher performance including excellent impact strength and improved elongation at break. Up to now, the effective and convenient way to prepare the iPP with high content of  $\beta$ -phase has been successfully achieved by addition of certain  $\beta$ -nucleating agent. Since the coexistence of  $\beta$ -nucleating agent and flow (shear flow, extensional flow or mixed), which usually exists in common industrial processing, makes the crystallization process more complex, their combined effect on the structure evolution of polymers, especially in the early stage of crystallization is still not well understood. The mechanical properties of iPP depend strongly on its crystallinity, crystal orientation and morphology determined by the conditions during preparation. On the other hand, the mechanical properties of polymers can also be modulated by deformation processing, which is directly related to the deformation-induced structure transition. However, the transition mechanism of different crystal forms and structure-property correlation still remain unclear. In this thesis, time-resolved synchrotron X-ray scattering was firstly used for the in-situ study of the structural and morphological developments of  $\beta$ -nucleated iPP during shear-induced crystallization. It was found that the crystallization process was strongly influenced by the concentration of  $\beta$ -nucleating agent, shear rate and shear temperature. Then extension-induced crystallization was investigated by a novel melt draw experiment, where a different crystallization mechanism compared to the shear-induced crystallization was found. Subsequently,  $\beta$ -nucleated iPP samples with different thermomechanical histories were scanned by synchrotron X-ray microbeam to construct their overall morphological distributions, including distributions of crystallinity, lamellar thickness, orientation, etc. Finally, these morphology-identified samples were investigated by in-situ synchrotron X-ray measurements coupled with mechanical testing to follow the structure evolution during deformation at elevated temperature. It was found that the deformation behaviour of  $\beta$ -nucleated iPP was closely associated with its initial morphology, its subsequent variation during stretching as well as the stretching conditions including the stretching rate and stretching temperature. The current study would not only contribute to the development of crystallization and deformation theory but also be beneficial for the material design.

## Kurzzusammenfassung

Isotaktisches Polypropylen (iPP), als eines der vielseitigsten thermoplastischen Massenpolymere, ist ein polymorphes Material mit verschiedenen Kristallmodifikationen, bei denen die  $\beta$ -Form ein höheres mechanisches Eigenschaftsprofil einschließlich ausgezeichneter Schlagfestigkeit und verbesserter Bruchdehnung aufweist. Bisher wurde auf effektive und zweckmäßige Weise die Herstellung von iPP mit einem hohen Anteil der  $\beta$ -Phase durch Zugabe bestimmter  $\beta$ -Nukleierungsmittel erreicht. Da die Koexistenz von  $\beta$ -Nukleierungsmittel und Fließen (Scherfließen, Dehnfließen oder gemischt), die normalerweise in üblichen industriellen Verarbeitungsprozessen vorliegt, den Kristallisationsprozess komplexer macht, wird ihr kombinierter Einfluss auf die Strukturentwicklung von Polymeren, insbesondere in der frühen Phase der Kristallisation, noch nicht gut verstanden. Die mechanischen Eigenschaften von iPP hängen stark von Kristallinität, Kristallorientierung und Morphologie ab, die durch die Bedingungen während der Herstellung bestimmt werden. Andererseits können die mechanischen Eigenschaften von Polymeren auch durch Deformation, die direkt mit einem verformungsinduzierten Strukturübergang herbeiführt, verändert werden. Jedoch bleiben der Übergangsmechanismus von verschiedenen Kristallformen und die Struktur-Eigenschafts-korrelation noch unklar. In dieser Arbeit wurde die zeitaufgelöste Synchrotron-Röntgenstreuung erstmalig für die in-situ-Untersuchung der strukturellen und morphologischen Veränderungen von  $\beta$ -nukleiertem iPP während der scherinduzierten Kristallisation eingesetzt. Es wurde gefunden, dass der Kristallisationsprozess stark von der Konzentration des  $\beta$ -Nukleierungsmittels, der Schergeschwindigkeit und der Schertemperatur beeinflusst wird. Danach wurde dehninduzierte Kristallisation mittels eines neuartigen Schmelzzugversuches untersucht, wobei unterschiedlicher Kristallisationsmechanismus im Vergleich zu der scherinduzierten Kristallisation gefunden wird. Weiterhin wurden die  $\beta$ -nukleierten iPP-Proben mit unterschiedlichen thermomechanischen Vorgeschichten mittels eines Synchrotron-Röntgenmikrostrahls abgescannt, um orts aufgelöst ihre Morphologie zu erfassen, einschließlich der Verteilung der Kristallinität, lamellaren Dicke, Orientierung usw. Schließlich wurden diese Proben mit definierter Morphologie mittels in-situ Synchrotron-Röntgenstreuung in Verbindung mit mechanischen Tests untersucht, um die Strukturentwicklung während der Verformung bei erhöhter Temperatur zu verfolgen. Es wurde gefunden, dass das Verformungsverhalten von  $\beta$ -nukleiertem iPP stark von seiner ursprünglichen Morphologie, deren anschließender Veränderung während des Verstreckens sowie den Verstreckbedingungen einschließlich der Verstreckrate und Verstrecktemperatur abhängig war. Die vorliegende Arbeit soll nicht nur zur Entwicklung der Kristallisations- und Verformungstheorie beitragen, sondern auch hilfreich für das Materialdesign sein.



# Table of contents

<b>Table of contents.....</b>	<b>1</b>
<b>1 Introduction (outline and objectives).....</b>	<b>4</b>
<b>2 Semi-crystalline polymers: Scientific background and state of the art .....</b>	<b>7</b>
2.1 Quiescent crystallization of semi-crystalline polymer.....	7
2.2 Flow induced crystallization-literature review .....	9
2.3 Avrami theory in polymer crystallization .....	11
2.4 Deformation behaviour of semi-crystalline polymer .....	12
<b>3 <math>\beta</math>-nucleated isotactic polypropylene.....</b>	<b>16</b>
3.1 Structure of isotactic polypropylene .....	16
3.2 $\beta$ -nucleating agent.....	18
3.3 Mechanical properties.....	19
<b>4 Experimental.....</b>	<b>21</b>
4.1 Materials.....	21
4.2 Sample preparation .....	21
4.3 Rheo-Xray measurement.....	22
4.4 Morphological scan measurement.....	23
4.5 Tensile deformation measurement .....	24
4.6 Melt draw measurement.....	25
4.7 Polarized optical microscopy.....	26
<b>5 X-ray data evaluation .....</b>	<b>27</b>
5.1 Basic properties of X-rays .....	27
5.2 Crystallinity, $\beta$ -content and crystal size.....	28
5.3 Long period and lamella thickness .....	30
5.4 Orientation degree .....	30
<b>6 Results and discussion.....</b>	<b>31</b>
6.1 Crystallization under quiescent condition .....	31
6.1.1 Morphology of $\beta$ -nucleating agent.....	31
6.1.2 Crystallization kinetics under quiescent condition.....	31
6.1.3 Evolution of long period under quiescent condition .....	36
6.2 Shear induced crystallization.....	37
6.2.1 Influence of NJS concentration on the shear induced crystallization .....	37

6.2.1.1	Overall crystallization kinetics after step shear.....	37
6.2.1.2	Crystallization kinetics of $\alpha$ crystals.....	39
6.2.1.3	Crystallization kinetics of $\beta$ -crystals .....	40
6.2.1.4	Crystal orientation.....	41
6.2.1.5	Interaction of NJS particles with the polymer melt after step shear .....	44
6.2.1.6	Evolution of long period after application of shear.....	45
6.2.1.7	Proposed crystallization mechanism .....	46
6.2.2	Influence of shear rate on the crystallization.....	47
6.2.2.1	Overall crystallization kinetics .....	47
6.2.2.2	Crystallization kinetics of $\alpha$ -crystals .....	49
6.2.2.3	Crystallization kinetics of $\beta$ -crystals .....	50
6.2.2.4	Evolution of long period under various shear conditions .....	52
6.2.3	Influence of the temperature on the shear induced crystallization.....	53
6.2.3.1	Overall crystallization kinetics .....	53
6.2.3.2	The development of $\beta$ -crystals .....	54
6.2.3.3	The evolution of long period .....	58
6.3	Extension induced crystallization of $\beta$ -nucleated iPP .....	58
6.3.1	Morphology of NJS particles in the quiescent iPP melt.....	59
6.3.2	WAXS .....	59
6.3.3	SAXS .....	61
6.4	Morphological distributions of injection-moulded $\beta$ -iPP investigated by microbeam .....	65
6.4.1	Influence of concentration of $\beta$ -nucleating agent.....	66
6.4.1.1	Distributions of crystallinity.....	66
6.4.1.2	Distributions of long period and lamellar thickness.....	68
6.4.1.3	Distributions of orientation degree .....	69
6.4.2	Influence of thermomechanical history .....	69
6.4.2.1	Distributions of crystallinity.....	70
6.4.2.2	Distributions of long period and lamellar thickness.....	70
6.4.2.3	Distributions of orientation functions .....	71
6.5	Structural development of injection-moulded $\beta$ -iPP under deformation.....	72
6.5.1	Influence of concentration of $\beta$ -nucleating agent-preliminary results .....	72
6.5.2	Influence of thermomechanical history on the injection-moulded samples .....	82
6.5.2.1	Mechanical behaviour of injection-moulded samples under uniaxial stretching.....	82
6.5.2.2	In-situ WAXS analysis.....	83
6.5.2.3	In-situ SAXS analysis .....	86
6.5.3	In-situ WAXS and SAXS analysis of $\beta$ -iPP stretched with various stretching rates .....	89
6.5.3.1	In-situ WAXS analysis.....	89
6.5.3.2	In-situ SAXS analysis .....	91

6.5.4	Structure variation of tensile-deformed $\beta$ -iPP at elevated temperatures - A comparison between compression- and injection-moulded samples .....	92
6.5.4.1	Mechanical behaviour of injection- and compression-moulded samples under uniaxial stretching .....	93
6.5.4.2	Stretching at 70°C .....	94
6.5.4.3	Stretching at 110 °C .....	98
<b>7</b>	<b>Conclusion .....</b>	<b>102</b>
<b>8</b>	<b>Recommendation for further work .....</b>	<b>106</b>
<b>9</b>	<b>Reference .....</b>	<b>107</b>
	<b>Acknowledgments .....</b>	<b>118</b>
	<b>Publications and presentation .....</b>	<b>120</b>
	<b>List of figures .....</b>	<b>121</b>
	<b>List of tables .....</b>	<b>128</b>
	<b>Eidesstattliche Erklärung .....</b>	<b>129</b>

# 1 Introduction (outline and objectives)

Polymer crystallization is a kinetically controlled phase transition, in which flexible molecules of entangled melt are gradually arranged into ordered solid crystalline structure [1-6]. During quiescent crystallization, polymer melt usually crystallizes into spherulites which have well-defined crystal structure and architecture [2, 7, 8]. However, in normal polymer processing operations, such as injection moulding, extrusion, fiber spinning, and blowing moulding, etc., polymer melts are subjected to complicated flow fields (shear, extension or mixed). It has been well established that semi-crystalline polymers crystallized under flow fields exhibit an increased crystallization rate by orders of magnitude and different morphological development compared with that under quiescent condition [4, 9, 10]. In general, the flow fields promote the alignment of molecular chains along the flow direction, which reduces the entropy of polymer chains and induces the formation of oriented crystal nucleation precursors with a lower free energy [11, 12]. The lifetime of these flow-induced precursors is dependent on the intensity of the flow fields and crystallization conditions [13]. At a given temperature, the survival time is longer for precursors induced at higher shear rate. The initially formed structures often dictate the subsequent development of morphology. The morphological structure (such as size, shape, type and orientation of crystallites) formed during the flow-induced crystallization process governs the final physical properties (mechanical, optical, electrical, etc.) of semi-crystalline polymers. Thus in recent years, the study of flow-induced crystallization has drawn a considerable attention due to both industrial and scientific significance since it allows the control and prediction of final morphologies and properties of the semi-crystalline polymers by polymer processing [14].

Isotactic polypropylene (iPP), as one of the most versatile commodity thermoplastic polymers, is a polymorphic material having several crystal modifications such as monoclinic ( $\alpha$ ), trigonal ( $\beta$ ) and orthorhombic ( $\gamma$ ) types.  $\alpha$  type is thermodynamically stable.  $\beta$  type is metastable and can be established when the polymer crystallizes (i) in a temperature gradient, (ii) under strong shear and (iii) in the presence of specific heterogeneous nucleating agents. It has been reported that amongst all of these crystal types, the  $\beta$ -form exhibits higher performance including excellent impact strength and improved elongation at break, i.e. an enhanced ductility [15, 16]. Up to now, the most effective and convenient way to prepare the iPP with high content of  $\beta$ -phase has been successfully achieved by addition of certain  $\beta$ -nucleating agent.

It is reasonable to assume that the shear flow and nucleating agent may generate the synergistic increase of  $\beta$ -content in iPP, however, the  $\beta$ -content indeed decreases with increase of shear rate under relative high concentration of  $\beta$ -nucleating agent, which was attributed to the acceleration of nucleation of  $\alpha$ -crystals under flow and interaction between flow and nucleating agent. The higher the applied flow rate, the more  $\alpha$ -nuclei can be generated and thus the less content of  $\beta$ -phase formed

due to the competition of growth between  $\alpha$ - and  $\beta$ -crystals [12, 17]. Since the coexistence of flow and  $\beta$ -nucleating agent makes the crystallization process more complex, their combined effect on the structure evolution of polymers, especially in the early stage of crystallization is still not well understood. The local velocity gradient may increase by orders of magnitude in the vicinity of nucleating agent [13], where the polymer chains may be more effectively stretched and form more oriented nuclei, thus markedly change the environment around the nucleating agent compared with that under quiescent condition. To the best of our knowledge, how the  $\beta$ -nucleating agent would interact with those oriented polymer melt and nuclei still remains unclear. In addition, the  $\beta$ -nucleating agent may exhibit various morphologies in iPP matrix at different concentrations. It was reported that the shape of additives may strongly influence the amount of flow-induced oriented nuclei. Anisotropic additives may generate greater numbers of flow-induced nuclei due to its strong interactions with flow field compared with isotropic additives [18]. However, the possible mechanism involved still cannot be well elucidated.

In the current study, a commercial  $\beta$ -nucleating agent named NJ-Star NU100 (NJS) was used, which is an efficient nucleating agent for producing high content of  $\beta$ -phase also under industrial conditions. It was reported [19] that there is a critical concentration of 0.03 wt%, at which  $\beta$ -nucleated iPP exhibits highest ductility and toughness. We investigated the corresponding morphology of NJS in the iPP melt by optical microscopy and found that it exhibited needle-like shape. The sheet of iPP with this needle-shaped nucleating agent has been prepared by extrusion and injection moulding [20, 21]. It was found that needle-like  $\beta$ -nucleating agent aligned along the flow direction due to the hydrodynamic force. In addition, a peculiar growth behaviour of iPP crystals should be stressed, i.e. the chain axis (c-axis) of iPP molecules was aligned perpendicular to the flow direction. Although model for the crystalline and lamellar structure of this  $\beta$ -nucleated iPP has been proposed [20-22], it is still relatively unknown how the structure and morphology of the iPP develop during the flow-induced crystallization.

The mechanical properties of iPP depend strongly on its crystallinity, crystal orientation and morphology as determined by the conditions during preparation. On the other hand, the mechanical properties of polymers can also be modulated by deformation processing, which is directly related to the deformation-induced structure transition. Due to this, the study of structure and its correlation with the stress-strain behaviour of iPP stretched at elevated temperatures has attracted significant interest in polymer science.

The present study proceeds as follow: firstly, in-situ synchrotron WAXS and SAXS and polarized optical microscopy were used to investigate the structural and morphological developments during quiescent and shear-induced crystallization of iPP with 3 different concentrations (0.01, 0.03 and 0.1 wt %) of  $\beta$ -nucleating agent.

Secondly, to investigate the peculiar structural and morphological evolution of iPP with needle-shaped nucleating agent during flow-induced crystallization, a specific melt draw experiment was designed which should be able to realize high extension of molecular chains and high alignment of needle-shaped  $\beta$ -nucleating agent. By synchrotron X-ray scattering the extension induced crystallization process was investigated in-situ.

Thirdly, the  $\beta$ -nucleated iPP samples with different thermomechanical histories were scanned by synchrotron X-ray microbeam to construct their overall morphological distributions, including distributions of crystallinity, lamellar thickness and orientation, etc.

Finally, these morphology-identified samples were investigated by in-situ synchrotron X-ray measurements coupled with mechanical testing to follow the structure evolution during deformation at elevated temperature.

## 2 Semi-crystalline polymers: Scientific background and state of the art

### 2.1 Quiescent crystallization of semi-crystalline polymer

Polymer crystallization is a kinetically controlled phase transition, in which flexible molecules of entangled melt are gradually arranged into ordered solid crystalline structure [1-6, 23]. Many polymers normally can only crystallize partially with crystallinity typically ranging from 10% to 60%. This incomplete crystallization can be mainly attributed to kinetics obstruction originated from the molecular chain entanglements, which cannot be removed but just transferred into the amorphous region during solidification from the melt. This kinetics restriction results in the formation of periodic layer-like lamellar crystals with typical thickness of 10-50 nm and entangled amorphous phase in between forming the so-called semi-crystalline state [24]. Morphological structure (such as size, shape, type and orientation of crystallites) formed during the crystallization process governs the final physical properties (mechanical, optical, electrical, etc.) of semi-crystalline polymers. Thus it is of relevant industrial and scientific importance to understand the crystallization mechanism which is essential for designing semi-crystalline materials with desired properties.

During quiescent crystallization, polymer melt usually crystallizes into spherulites which have well-defined crystal structure and architecture [2, 7, 8]. After many years of intensive study and hot debate, the crystallization process is more or less, well understood. It has been widely accepted that the polymer crystallization follows the classical nucleation-growth theory. Depending on the role of external particles, the nucleation can proceed either by homogeneous nucleation or heterogeneous nucleation [25]. The former occurs spontaneously and randomly in the polymer melt, while the latter takes place mainly around some external particles.

In homogeneous primary nucleation step, density fluctuations in supercooled polymer melt would result in bundles/arrays of ordered chain segments. There is a size threshold for the formation of crystalline phase, which is resulted from the competition between the free energy gain of newly created volume and free energy cost due to the formation of new interfacial area [26]. The aggregates with size  $\zeta$  smaller than that of critical nucleus dissolve back into the polymer liquid phase, while the super-critical-sized aggregates remain stable and are termed as embryonic crystal nuclei. Thermodynamically, those surviving nuclei overcome the nucleation barrier in free energy and will spontaneously grow as free energy change,  $\Delta G$ , decreases with further increasing  $\zeta$ .

For many years, the two major kinetic theories concerning the crystal growth during polymer crystallization are the surface nucleation and growth model developed by Lauritzen and Hoffman (LH) [27-29] and the subsequent entropic barrier model suggested by Sadler and Gilmer (SG) [30, 31]. Both have considered that the crystal growth is mainly a stepwise process which directly occurs on the

lateral growth surface. Generally, these two models can be distinguished by the origin of the energy barrier [32]. In LH model, an energy barrier must be overcome when placing a molecule or a segment of long chain onto the growth surface. On the other hand, the SG model argued that a reversible process involving detachment and attachment of short-chain sequences exists at the growth front, which slows down the growth rate by invoking many possible configurations, only a few of which contribute to the crystal growth. Thus, the barrier controlling the growth kinetics in SG model is mainly entropic in nature [32].

In sharp contrast to the above models, recent experimental results [33-35] indicated that the formation of the polymer crystal is actually accompanied with a preordering process during the induction period before crystal nucleation. The ordered precursors formed during this process are induced by a spinodal decomposition mechanism and assist the subsequent crystal nucleation from the polymer melt. In addition, Strobl [3] proposed recently a new model for elucidating the polymer crystallization process, in which the formation and growth of lamellae is a multi-step process (Fig. 1). A mesomorphic precursor layer is always formed first and spontaneously thickens to a critical value, where it solidifies to produce a higher ordered granular crystal layer or block crystallites. Finally the merging of the blocks occurs towards inner perfection of lamellar structure. It is worth to mention that if the block crystallites were well aligned in one direction, a distinct cross pattern in small angle X-ray scattering (SAXS) may be obtained [36].

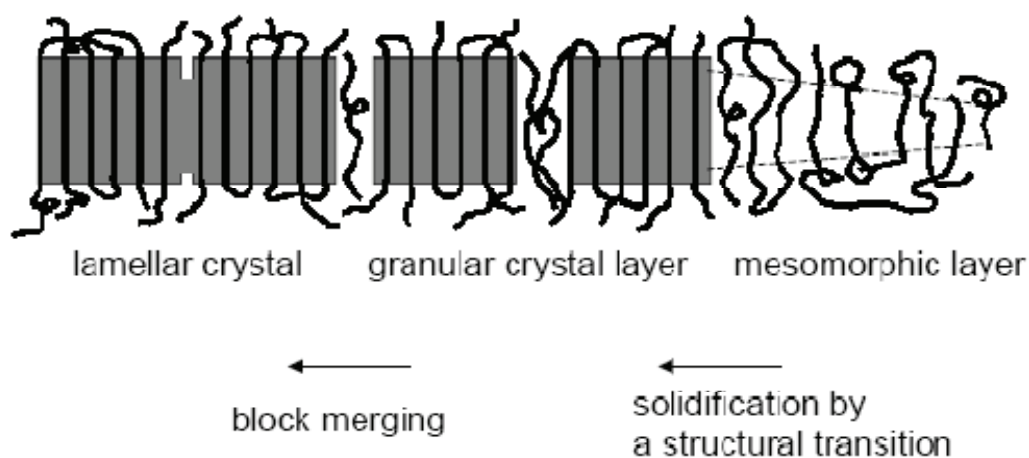


Fig. 1 Strobl's model for the formation of polymer crystallites

With the help of transmission optical microscope it can be observed that the randomly distributed crystal nuclei grow radially in all spatial directions and form spherulites which have spherical shape or spherical symmetry [8]. A spherulite is composed of bundles of folded chain lamellae – layerlike crystallites [37, 38], grown from a central nucleus and followed with continuous spraying apart and branching to fill space and generate a radially symmetrical structure [8, 26]. The size of a spherulite



can be ranged from several micrometers to millimeters, depending on the intrinsic structure of the polymer chain and the crystallization condition, such as crystallization temperature and cooling rate [39]. The lamellae are separated by the disordered amorphous phase. The molecular chains inside the lamellae are nearly or exactly oriented perpendicular to the radial direction of the spherulites. It is worth noting that there is a certain thickness distribution in lamellae [40, 41]. The thicker ones are associated with the primary lamellae whereas the thinner ones are secondary lamellae which are resulted from the secondary nucleation on the primary ones. The lamellar thickness is kinetically controlled and dependent on the crystallization conditions [3]. Usually, the lamellar thickness increases with increasing crystallization temperature. However, this elevated crystallization temperature always leads to a decrease in crystallization rate described by an exponential law.

## **2.2 Flow induced crystallization-literature review**

As mentioned above, quiescent melt usually crystallizes into spherulites with folded chain lamellae. However, in normal polymer processing operations, such as injection moulding, extrusion, fiber spinning, and blow moulding, etc., polymer melts are subjected to complicated flow fields (shear and extension). It has been well established that semi-crystalline polymers crystallized under flow fields exhibit an increasing crystallization kinetics by orders of magnitude and different morphological development comparing with that under quiescent condition [4, 9, 10]. So in recent years, the study of flow-induced crystallization has drawn a considerable attention due to both industrial and scientific significance since it allows the final morphologies and properties of the semi-crystalline polymers to be controlled and predicted during the polymer processing [14].

In general, the flow fields promote the alignment of molecular chains along the flow direction, which reduces the entropy of polymer chains and induces the formation of oriented crystal nucleation precursors in a lower free energy [11, 12]. The lifetime of these flow-induced precursors is dependent on the intensity of the flow fields and crystallization conditions [13]. It has been observed that these oriented precursors, when generated by flow fields at low crystallization temperature ( $T_c$ ), would break down into point-like ones at high  $T_c$  or gradually relax during the holding time [13, 42, 43]. On the other hand, it has been reported that these row nuclei can remain stable for a very long time under quiescent condition, even above the melting temperature of the crystals [11, 44]. At a given temperature, the survival time is longer for precursors induced at higher shear rate.

Anisotropic shish-kebab structure (Fig. 2), which is a very interesting structure formed in the flow field, is usually observed in the common polymer processing and may strongly improve the final properties of polymer products. Kalay et al. reported on the iPP with high level of molecular orientation produced by shear-controlled orientation injection moulding, which exhibited an 80% increase in Young's modulus and a 65% increase in tensile strength compared with that prepared by conventional injection moulding. The increase in the mechanical properties is mainly attributed to the formation of highly oriented shish-kebab morphology developed in shearing [45, 46].

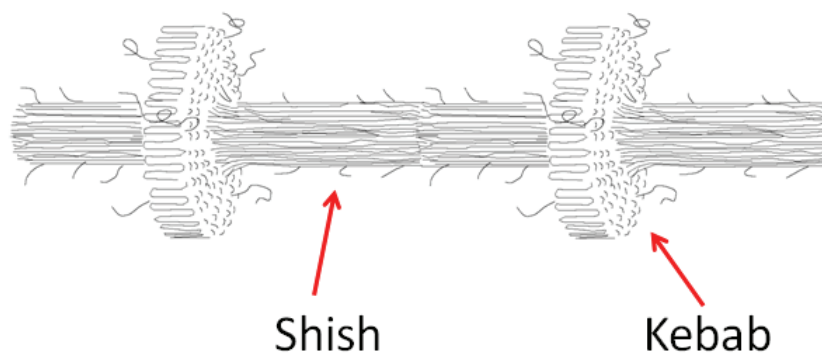


Fig. 2 A schematic illustration of shish-kebab structure. During flow induced crystallization, extended chains firstly crystallized giving rise to shishes, which were served as nucleation templates for the subsequent formation of folded-chain lamellae (kebabs) [47, 48]

Over the past few decades, many research studies on the development of shish-kebab superstructure during polymer processing have been carried out and can broadly be divided into two parts. One part was basically focused on the boundary conditions for the shish-kebab formation; the other part was focused on the formation mechanism of initial shish-kebab nucleus under flow [49]. Benefitting from recent development of advanced characterization techniques, such as time-resolved SAXS and WAXS, time-resolved SALS, rheo-optical measurements, and in-house developed setups, the critical flow conditions for the onset of oriented structure have been, more or less, well identified. Briefly, in order to initiate the shish-kebab structure, two conditions should be fulfilled: (1) the shear rate should be faster than the inverse Rouse time of longest molecular chain ( $\dot{\gamma} > 1/\tau_R$ ); (2) the applied mechanical work should be above a threshold value. Only when these two conditions are simultaneously satisfied, the molecular chains can be stretched by the flow and keep extended during subsequent crystallization [50].

Although the boundary conditions for shish-kebab formation have been identified, the mechanism of the initial shish formation, which is the core of the flow induced crystallization, is still under debate. In early studies, a widely accepted concept to explain the formation of shish-kebab structure was coil-stretch transition, which was first suggested by De Gennes in a study related to the reaction of solute polymer coil to strong flow field [51]. In brief, upon an external flow field, some long and flexible polymer coil may undergo a coil-stretch transition and those stretched polymer chains would aggregate to form extended fibrils (shishes) [11, 12, 49]. Subsequently, the other coiled chains could epitaxially crystallize on the fibrils to form periodically folded layer-like lamellae (kebabs) through processes of chain diffusion and adsorption [52]. This concept was firstly verified by Keller et al. by investigation of flow induced crystallization in various concentrated polymer solution [53-57]. They observed an abrupt change in birefringence at a critical strain rate which was attributed to onset of high chain extension associating with the coil-stretch transition and further pointed out that polymer chains with higher molecular weight, due to their longer relaxation time, can be more easily extended

under flow. These results are origin of Keller's well-known molecular model of shish-kebab, which was gradually adopted by the scientific community during last several decades [47]. Based on the observations that the shish-kebab morphologies of polymer melts formed under flow conditions are similar to that of dilute polymer solution, Keller further transplanted the shish-kebab model originated from the polymer solutions to the entangled polymer melts and suggested that the primary flow-induced nuclei in polymer melts, similar in polymer solutions, are mainly composed of chains with high molecular weight. Hsiao and co-workers followed the conceptual idea of Keller and even proposed that only the polymer chains with high molecular weight participate in the formation of shish, while that with low molecular weight does not [4]. However, this point of view was challenged by Kornfield et al., who investigated the deuterium-labeled iPP and found that the fraction of long chain molecules in shish matches that in the surrounding melt by the help of small angle neutron scattering experiment [58]. Yet this finding is not contradictory to the previous literatures finding that the longest molecular chains play the essential role of forming shish [59-61]. The long molecular chains may guide the neighbouring chains to join them in the shish formation [58]. It is well known that polymer chains with high molecular weight entangle and form a network structure in melt state. However, Keller did not rationalize the consequence of large numbers of chain entanglements existed in the long molecular chains. It is unlikely that the coil-stretch transition of individual chain may occur since it involves multiple steps of chain disentanglements which cannot take place under typical flow conditions [62]. A great deal of work has been done to modify the Keller's idea. For example, Penning et al. proposed that the shish originated from the stretched entangled network under flow field [63], which is also adopted by Han et al. [49, 64, 65] as well as Kanaya et al. [66] and further verified by Li et al [67-69]. The shish formation has been discussed controversially, since it is closely related to the crystallization and processing conditions, the structure of polymer itself, etc.

## 2.3 Avrami theory in polymer crystallization

As mentioned above, the morphology formed during the processing strongly determines the mechanical properties of polymers. To understand and ultimately control the formation process of crystal morphology, it is essential to understand the crystallization kinetics, since the kinetics of crystallization process defines the structure and properties of polymer materials [70]. The kinetics of polymer isothermal crystallization is usually described by the semi-empirical Avrami equation, which can be expressed as follows [45]:

$$\frac{X_t}{X_\infty} = 1 - \exp(-kt^n) \quad (1)$$

Where  $X_t$  and  $X_\infty$  are the crystallinity at time (t) and at infinite time ( $\infty$ ), respectively, k is the crystallization rate constant and n is Avrami exponent depending on the nucleation mechanism and growth geometry of crystallites. When the growth of crystallites is under homogeneous nucleation (also named sporadic or thermal nucleation), the n values of 2, 3 and 4 correspond to rodlike, disklike

and spherulike crystal growth geometry, respectively. On the other hand, in heterogeneous nucleation (also termed predetermined, instantaneous or athermal nucleation), the  $n$  values of 1, 2 and 3 represent the crystal growth geometry of rods, disks and spheres, respectively [60, 70-72]. It is worth to point out that non-integer values of Avrami exponent are often obtained in polymer crystallization from entangled melt, indicating the presence of mixed crystal growth geometry.

The Avrami equation has been widely used to characterize the crystal growth geometry in flow induced polymer crystallization with or without nucleating agent [12, 42, 52, 60, 69, 71-76]. Keum et al. showed that the Avrami exponent was found to be about 3 indicating 2-dimensional growth of kebab in sheared high-density polyethylene melts under thermal nucleation. However, Agarwal et al. found that the values of Avrami exponent ( $n \sim 1.8$  to  $2.8$ ) indicated a rod or disklike crystal growth geometry in the long chain branched iPP polymers under flow induced crystallization [71]. Chen et al. reported that shear increased the crystal growth dimensionality from two-dimensional lamellar growth to mixed two-dimensional lamellar growth and three-dimensional spherulitic growth geometries with Avrami exponent changing from around 2 to around 2.5 for iPP composites with 0.1 wt% carbon nanotubes [74]. On the other hand, Phillips et al. indicated that shear reduced the crystal growth dimensionality from 3-D to 2-D with Avrami exponent changing from 3 to 2 for iPP nucleated with 2 wt% amorphous isotactic polystyrene particles [72]. More recently, Li et al. put forward that with strain larger than fracture strain, the Avrami exponent  $n \leq 1.3$  indicated a fibrillar and disk-like crystal growth for iPP under extension flow induced crystallization. It was interesting that with strain far beyond fracture strain, the Avrami exponent can even be about 0.5 suggesting a diffusion controlled 1-D growth process [69]. The Avrami exponent of flow induced crystallization has been debated controversially since it is closely associated with crystallization and processing conditions, the concentration and aspect ratio of additives, etc.

It's worth mentioning that the Avrami equation (equation 1) is valid when  $X_t$  is small, i.e. at the early crystallization stage, however, would become invalid at the late crystallization stage due to the impingement effect.

## **2.4 Deformation behaviour of semi-crystalline polymer**

The mechanical properties of semi-crystalline polymers depend strongly on their crystallinity, the orientation of crystalline and amorphous phase and the morphology as determined by preparation conditions. On the other hand, the mechanical properties of the polymers can also be greatly improved by various deformation processing operations, among which stretching deformation is the most frequently used. During the stretching deformation of semi-crystalline polymers, a structure evolution usually occurs, which involves the variation of crystalline and amorphous phases, including strain-induced crystallization, crystal transition, chain orientation, fibril formation and cavitation, etc. Due of this, the study of structure transition and its correlation with the stress-strain behaviour of semi-crystalline polymer materials has attracted significant interest in polymer science.

Semi-crystalline materials can be shaped at temperature between  $T_g$  (glass transition temperature) and  $T_m$  (melting temperature) by the stretching deformation. The corresponding engineering stress-strain curve in this temperature range can be broadly divided into 2 regions: visco-elastic deformation and plastic deformation, which are separated by a maximum (yield point) at a few percent strain. Although deformation before this yield point apparently behaves elastically, stress relaxation due to molecular rearrangement in the amorphous phase actually occurs (viscoelasticity). After reaching the yield point, the stress drops and a neck forms in the specimen. Then the neck propagates further while the stress remains almost constant within an extensive elongation, a process usually referred to as cold drawing. However, it is worth to mention that in the true stress-strain curve the stress in the stage of neck formation and propagation will nearly continue to increase, which is associated with the quick reduction of cross-sectional area. With further elongation, the polymer strain hardens, which is originated from the strengthening of entangled polymer network, and then it breaks [77, 78].

Though the necking and cold drawing can be easily observed at macroscopic scale, the underlying mechanism at molecular scale responsible for the structure variations during this deformation process is still under much debate [79]. Many models have been proposed to elucidate the deformation mechanism of semi-crystalline polymers. Among them two general but distinct models have to be stressed. The first significant mechanism proposal was made by Peterlin [80], who concerned the molecular mechanism of drawing semi-crystalline polymers with spherulitic structure. According to Peterlin, the spherulites are basically composed of the folded chain lamellae separated by amorphous phase and interconnected by a few tie molecules. Upon stretching, the tie molecules align along the stretching direction and transfer the stress between the lamellae leading to the subsequent unfolding the chain sections and splitting the lamellae into small crystalline mosaic blocks, which then reorganize into a microfibrillar structure of high mechanical anisotropy. On the other hand, Flory and Yoon pointed out that due to the re-entry of molecular chains in the same crystalline layer during melt crystallization, profuse connections are existed between adjacent lamellae, which results in the partial melting of crystalline region during the cold drawing. The transition from lamellae to the oriented fibrillar structure thus involves melting of pre-existing lamellae and subsequent orientation-induced crystallization in the melt phase upon stretching [81]. Each of the above 2 models has respectively received extensive supports [82-85]. Recently, many investigations further proposed that both mechanisms coexisted during the stretching deformation of semi-crystalline polymers [23, 86-88]. It is suggested that in the course of deformation process fragmentation of crystalline lamellae takes place and then not only the reorientation of the crystalline blocks and reorganization of unfolded chains and extended tie molecules in amorphous phase into fibrillar structure follow, but also a melting-recrystallization of crystallites is possible. Although some progress in crystalline polymer deformation has been made, the detailed deformation mechanism is still an area of controversy [87, 88].

Semi-crystalline polymers often exhibit various crystalline structures. The crystal transition between different structures can also take place during the deformation process. For example, during drawing of nylon 6 fibers an apparent transition from  $\gamma$ -phase crystals to  $\alpha$ -phase crystals takes place, which is explained that the  $\gamma$ -phase crystals were destroyed during the drawing process and then converted into fiber structure of the  $\alpha$ -phase form [89]. Ran et al. investigate structure changes of iPP fibers during drawing experiments and found that the  $\alpha$ -form crystals were converted into the mesomorphic modification by drawing at ambient temperature. They suggested that the formation of the mesophase was triggered by pulling chains out from the  $\alpha$ -crystals upon stretching [90]. Kawakami et al. studied the in-situ structure development of amorphous poly (ethylene terephthalate) (PET) under uniaxial deformation and found that deformation induced the phase transition from original “slush” structure (amorphous + nematic) into stable triclinic crystalline structure [91]. In addition, strain-induced phase transition has also been widely reported in poly( $\omega$ -pentadecalactone) (PPDL), poly (L-lactic acid) (PLA) and PE [92-96].

It was found that the stretching temperature can strongly affect the deformation behaviour and structure formation of polymers. Some previous studies have been conducted to investigate the deformation behaviour of amorphous PLA at different stretching temperatures [94, 97, 98]. The results show that the crystallization rate and orientation degree of crystals at same strain rate were controlled by the stretching temperature. In addition, it was reported that both reorganization of crystalline blocks and strain-induced lamellar fragmentation and recrystallization were enhanced by increasing the stretching temperature [23, 87, 99]. On the other hand, the deformation rate plays an essential role in deciding molecular orientation and structure variation of polymers [93]. For example, Mahendrasingam et al. reported that the crystallization of polymers at different strain rate starts at different stages during extension process. When the strain rate is faster than the rate of chain retraction, the onset of crystallization is postponed until the end of the deformation process [97, 100]. Takahashi et al. pointed out that the crystal transition of polymers proceeded more efficiently at higher drawing rate during uniaxial stretching at constant tensile temperature [101]. It is widely believed that the polymer deformation behaviour and structure transition are the result of the synergistic effects of stretching temperature and strain rate.

During tensile drawing, the deformation-induced cavitation also plays a crucial role in the structure transformation of polymers [95, 102, 103]. The cavitation often appears at suitable stretching conditions and is visible as whitening at macroscopic scale during tensile deformation of polymers. Generally, the cavities are initiated around the yield point with ellipsoidal shape and alignment perpendicular to the stretching direction. The cavities propagate then quickly with their orientation gradually changing to the tensile direction during the subsequent necking and strain hardening [104]. The formation and growth of cavities are primarily responsible for the volume change during tensile drawing. Pawlak et al. reported that there was a competition between cavitation and activation of crystal plasticity during deformation. The cavitation occurred in polymers with crystals of higher plastic

resistance, whereas the plastic deformation dominated in polymers with lower plastic resistance [102]. The appearance of cavitation generally led to a variation of mechanical properties of polymers. The cavitation and its effect on the stretching stress depend on the species of materials, and intrinsic structure of materials as well as stretching conditions (stretching rate, strain, stretching temperature, etc.).

### 3 $\beta$ -nucleated isotactic polypropylene

#### 3.1 Structure of isotactic polypropylene

Polypropylene, as one of the most important thermoplastic polymers, has been widely used in various end-use applications because it has favourable price/performance ratio and can be modified to broaden its range of properties [105]. It is prepared by polymerizing propylene monomer. Its general chemical structure is illustrated in Fig. 3. The pendant methyl groups ( $\text{CH}_3$  in Fig. 3) attached to one half of the carbon atoms of the chain backbone has a strong effect on the characteristics of this polymer. The steric order of the methyl groups gives rise to three distinct stereoisomers: isotactic, syndiotactic and atactic, which are shown in Fig. 4 [106]. The polypropylene is called isotactic (iPP) when all methyl groups are located at the same side with respect to the chain backbone (Fig. 4 a). If the positions of methyl groups alternate, the polymer is syndiotactic (sPP) (Fig. 4 b). The polypropylene is termed atactic when the methyl groups are randomly positioned at the polymer backbone (Fig. 4 c). iPP is the most commercial polypropylene and is used in current study.

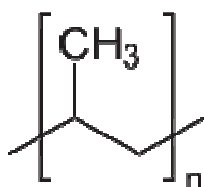


Fig. 3 General chemical structure of polypropylene

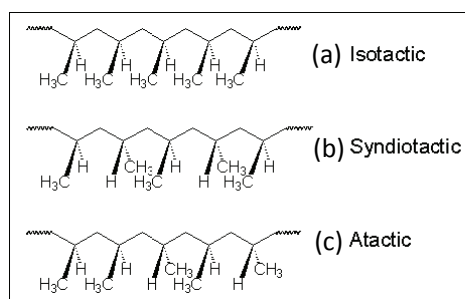


Fig. 4 Schematic illustration of chemical structure of 3 stereoisomers of polypropylene: (a) isotactic; (b) syndiotactic; (c) atactic

When crystallized from its melt, iPP always adopts a  $3_1$  helical conformation (3 monomer units per turn, as shown in Fig. 5) in the crystalline structure with the helix length of 0.66 nm. These helices can pack in different cell structures with the possible coexistence of helical right- and left-handed configurations (chirality) giving rise to different polymorphs of iPP, amongst which 3 crystalline forms have been identified, i.e.,  $\alpha$ ,  $\beta$  and  $\gamma$  crystal modifications [90, 107-109]. The crystalline structures of these 3 crystal modifications are illustrated in Fig. 6. The  $\alpha$ -modification (Fig. 6 a) exhibits a monoclinic unit cell [110] with parameters  $a = 0.665$  nm,  $b = 2.096$  nm,  $c = 0.65$  nm and  $\beta = 99.2^\circ$ . Each unit cell



contains 4 polymer chains with chain axes aligned parallel to the c-axis. The  $\beta$ -modification (Fig. 6 b) has a trigonal unit cell with parameter  $a = b = 1.103$  nm,  $c = 0.65$  nm [15, 111]. Three isochiral helices coexist in the unit cell. The  $\gamma$ -modification (Fig. 6 c) has a large orthorhombic unit cell with parameters  $a = 0.854$  nm,  $b = 0.993$  nm and  $c = 4.241$  nm [112]. It was the first identified crystal form exhibiting non-parallel chain-packing in a unit cell.

The  $\alpha$  type is thermodynamically stable and is by far most common [72]. The  $\beta$  type with low density and high degree of disorder is metastable and can be established when the polymer crystallizes (i) in a temperature gradient, (ii) under strong shear and (iii) in the presence of specific heterogeneous nucleating agents. The  $\gamma$ -iPP is relatively rare, however, it is favoured when iPP crystallizes under elevated pressure or the isotactic sequence length is interrupted [112-114].

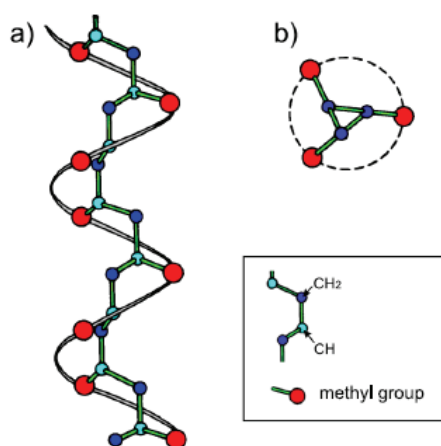


Fig. 5 Schematic illustration of  $3_1$  helix conformation of polypropylene; (a) side view, (b) top view (chain-axis projection) [115]

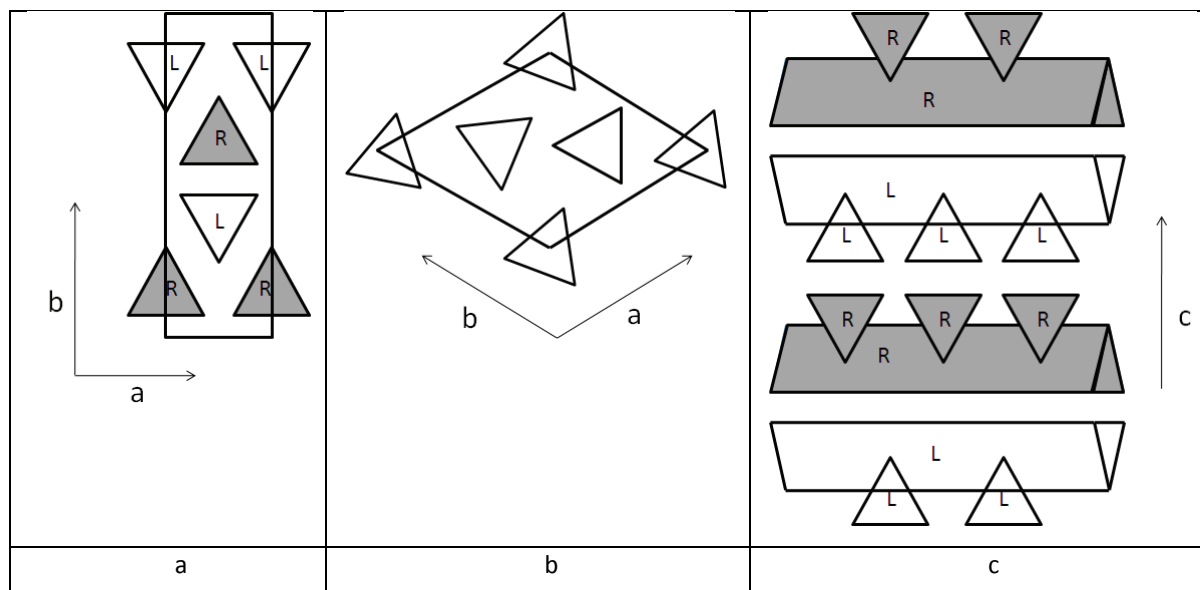


Fig. 6 Schematic illustration of different unit cells of iPP. (a)  $\alpha$ -phase, monoclinic, 4 chains per unit cell,  $a = 0.665$  nm,  $b = 2.096$  nm,  $c = 0.65$  nm and  $\beta = 99.2^\circ$ . (b)  $\beta$ -phase, trigonal, 3 chains per unit cell,  $a = b = 1.103$  nm,  $c = 0.65$  nm. The helices in above two phases are schematized in chain-axis projection and the triangles define the methyl carbon positions. (c)  $\gamma$ -phase structure with non-parallel chain packing, orthorhombic,  $a = 0.854$  nm,  $b = 0.993$  nm and  $c = 4.241$  nm. For a better presentation, the structure is projected along one of  $a$ - $b$  plane diagonals. Symbols R and L indicate the right- and left-handed helical chains, respectively [2].

### 3.2 $\beta$ -nucleating agent

It has been reported that from all of the crystal types of iPP, the  $\beta$ -form exhibits higher performance including excellent impact strength and improved elongation at break, i.e. an enhanced ductility [15, 16]. Up to now, the most effective and convenient way to prepare the iPP with high content of  $\beta$ -phase is adding certain  $\beta$ -nucleating agent. The available  $\beta$ -nucleating agents have been summarized by Varga [15] and they can be broadly divided into 3 categories: The first category is organic pigment, such as  $\gamma$ -trans-quinacridone (Red Pigment E3B) and Golden Yellow IGK; the second category includes a minority of aromatic ring compounds, such as  $N,N'$ -dicyclohexylterephthalamide,  $N,N'$ -dicyclohexyl-2,6-naphthalenedicarboxamide named NJ-Star NU100 (NJS); the third one includes compounds derived from certain group IIA metal salts or their mixtures with some specific dicarboxylic acids, such as LaC,  $\text{CaCO}_3$ , calcium salts of pimelic and suberic acid, and compounds of pimelic acid and calcium stearate [17, 21, 72, 116]. The selectivity of these nucleating agents can be explained by a two dimensional lattice matching theory. Key of this theory is that a reasonable epitaxial match, at least within 10%, exists between the repeat distance in the iPP unit cell and the corresponding nucleating agent surface inducing the epitaxial growth. It was found that the  $\beta$ -iPP (1 1 0) plane is the contact plane with  $\beta$ -nucleating agents. Nucleating agent with periodicity of around 0.65 nm (i.e.  $c$  axis periodicity of iPP) and an orthogonal geometry of the contact face are likely to induce the formation of  $\beta$ -iPP [117].

The commercial  $\beta$ -nucleating agent NJS, provided by Rika International Limited (Oldham, U.K.), was used in this thesis, which is an efficient nucleating agent for producing high content of  $\beta$ -phase also under industrial conditions. It was reported [19] that there is a critical concentration of 0.03 wt%, at which  $\beta$ -nucleated iPP, obtained under real processing conditions, exhibits highest ductility and toughness. However, it is worth to point out that NJS is not a selective  $\beta$ -nucleating agent, and also  $\alpha$ -iPP always forms in its presence. This behaviour of NJS was termed as dual nucleating ability [118]. This nucleating agent, with melting point of 400 °C, can be partially or completely dissolved in iPP melt depending on the final temperature of heating. The efficiency of  $\beta$ -nucleating agents strongly depends on the concentration and dispersion of the additives and the thermal treatment. Thus it is essential to control the crystallization conditions to obtain iPP with a defined crystalline structure [119].

The  $\beta$ -nucleating agent may exhibit various morphologies in iPP matrix at different concentrations. Special attention was paid to an anisotropic needle-like shape of  $\beta$ -nucleating agent in iPP melt [118]. The needle-like NJS may align along the flow direction at the extrusion process due to the hydrodynamic force [20, 21, 120, 121]. Then the  $\beta$ -crystals may grow epitaxially on the lateral planes of the oriented needle-like NJS crystals with their chain axis (c-axis) being perpendicular to the long axis of the latter. In this case, a peculiar growth behaviour of iPP crystals may appear, i.e. the c-axis of iPP molecules may be aligned perpendicular to the flow direction. This is the opposite orientation direction to a conventional product. The reason for this anomalous molecular orientation is possibly associated with the lattice matching manner. It was suggested that epitaxial matching exists between c-axis of iPP and the b-axis of NJS crystal, which are parallel to each other [122].

### 3.3 Mechanical properties

Compared with  $\alpha$ -iPP,  $\beta$ -iPP exhibits low crystal density, melting temperature and fusion enthalpy. In addition, the mechanical properties of  $\beta$ -iPP also differ significantly to that of  $\alpha$ -iPP [15]. Compared to  $\alpha$ -iPP, the  $\beta$ -iPP shows a low E-modulus and yield stress, but high ultimate tensile strength and elongation at break. The improvement in the latter may be attributed to the  $\beta$  to  $\alpha$  transition taking place during the necking which results in the formation of  $\alpha$ -phase with enhanced strength. The impact strength and toughness of  $\beta$ -iPP are also superior to  $\alpha$ -iPP. It was found that the toughness of  $\beta$ -iPP exceeds that of  $\alpha$ -iPP by 13% under static and 70% under dynamic condition, respectively. The upgraded toughness was related to the increased energy dissipation in the enlarged plastic zone [123]. In addition, the enhanced mechanical damping of  $\beta$ -iPP was also responsible for its pronounced toughness [15].

Huy et al. investigated the orientation behaviour of  $\alpha$ -iPP and  $\beta$ -iPP by rheo-optical Fourier transformed infrared spectroscopy and found that the  $\alpha$ -iPP preferred intralamellar slippage while the  $\beta$ -iPP favoured interlamellar slip and lamellar twisting during the uniaxial elongation [124]. This founding was supported by Lezak et al., who studied the plane-strain compression of  $\beta$ -iPP by X-ray and SEM [125]. Moreover, Li et al. investigated the deformation mechanism by WAXS and DSC. They

found that the  $\beta$ -phase was mechanically stable up to yielding point, while it began to transform to  $\alpha$ -phase with further stretching to necking, which indicated that local melting and crystallization took place during cold drawing [79]. In addition, by electronic microscopic method (SEM and TEM), they revealed that crazing, formed prior to necking, is the main cause of failure of  $\beta$ -iPP with highly perfect lamellae. The adjacent microcrazes would connect together and develop into large cracks [126]. Furthermore, Luo et al. demonstrated that sufficient connections between intercrystallites are the main reason for the pronounced toughness of iPP [127].

## 4 Experimental

### 4.1 Materials

The investigated polymer was a commercial iPP homopolymer, grade HD 120 MO, manufactured by Borealis (Linz, Austria) with weight-average and number-average molecular weights 365 kg/mol and 67.6 kg/mol, respectively [128] and a melt flow index of 8 g/10 min (at 230 °C and 2.16 kg).

The  $\beta$ -nucleating agent, N,N'-dicyclohexyl-2,6-naphthalenedicarboxamide (NJ-StarTR NU100, referred as NJS in this work), was provided by Rika International Limited (Oldham, U.K. ).

### 4.2 Sample preparation

The  $\beta$ -nucleated iPP was prepared by the following steps. Firstly a master batch was prepared by compounding molten iPP with 0.5 wt % of  $\beta$ -nucleating agent using a single screw extruder with a diameter of 19 mm and a length of 25D (Brabender) at 220 °C and a screw speed of 100 rpm. Then the master batch was compounded with iPP pellets using a co-rotating twin screw extruder ZSE 27 Maxx (Leistritz) with a screw diameter of 27 mm and a length of 36D. In this process an increasing temperature program from 200 °C to 220 °C, a screw speed of 200 rpm and a throughput of 10 kg/h were adjusted. Then the samples were injection-moulded into 80 x 80 mm sheets, by an injection moulding machine Ergotech 100/420-310 (Demag) and a cylinder temperature of 225 °C and a mould temperature of 40 °C. The concentrations of the nucleator were 0.01, 0.03 and 0.1 wt % and the samples were designated as Bpp1, Bpp2 and Bpp3, respectively (Tab. 1). The pure iPP without nucleating agent was also prepared under the same processing conditions for comparison.

Tab. 1  $\beta$ -nucleated iPP used in this study

Sample name	Concentration (wt %)
iPP	0
Bpp1	0.01
Bpp2	0.03
Bpp3	0.1

The thickness of the sheets can be 1 mm, 2 mm or 4 mm, depending on the experiment requirement. For melt draw experiment, 4 mm thick sheets were used to prepare dog-bone-like specimens with width of 5 mm and thickness of 4 mm. To carry out the shear induced crystallization, 19 mm disks were cut from 2 mm thick sheets. For tensile experiment, mini-dumbbell specimens were produced

from 1 mm thick sheets by CNC milling [78]. The specimens with their length along the injection direction were taken from 2 positions of sheets as indicated in Fig. 7. Sample in position 1 near the inlet with the distance of sample centre to the inlet about 18 mm underwent relatively higher shear rate and thus exhibited relatively higher degree of orientation comparing to the one in position 2 far from the inlet with the distance of sample centre to the inlet about 62 mm. For the morphological scan experiment, dog-bone specimens with thickness of 1 mm, gauge width of 1 mm and length of 10 mm were prepared from the 1 mm thick sheets. The specimens locate at the same position as tensile specimens with their length along the injection direction.

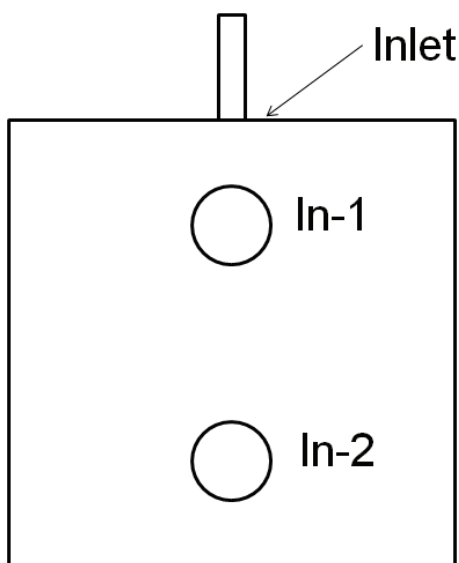


Fig. 7 The specimen positions in the injection moulding sheet

### 4.3 Rheo-Xray measurement

The synchrotron X-ray measurement for investigation of shear induced crystallization was carried out at beam-line BW4, DESY, Hamburg, Germany. The wavelength of the synchrotron radiation was 0.138 nm. Two dimensional WAXS and SAXS patterns were collected by using a Pilatus 300K pixel detector (Paul Scherrer Institute, Switzerland) for WAXS and a Mar CCD X-ray detector with a resolution of 2048 x 2048 pixels (pixel size = 0.0791 mm) for SAXS, respectively. The sample to detector distance was 153 mm for WAXS and 4012 mm for SAXS. The experimental arrangement is illustrated in Fig. 8. A Linkam CSS450 high temperature shear cell, which has been widely used in the field of in-situ rheo-X-ray studies [9, 11, 13, 14, 74, 129-132], was used to control the thermal history and shear field of sample. To avoid large absorption of X-ray, the original glass plates of the shear cell were replaced by Kapton windows. Flat disk-like samples with diameter and thickness of 19 mm and 2 mm, respectively, which were cut from the previous injection moulding specimens, were mounted between the two parallel windows of shear cell. The sample temperature was coincident with the controller imposed temperature which was demonstrated by an external thermocouple inserted into the polymer melt.

The thermal-shear profiles of the samples were set as follows: samples were first heated at a rate of 30 K/min from room temperature to 230 °C, compressed slowly to the required gap thickness of 1 mm and kept at this temperature for 5 min to erase previous thermal and mechanical history. Then the samples were cooled down at a rate of 30 K/min to the crystallization temperature, if there is no specific mention, of 138 °C. Upon reaching the crystallization temperature, one X-ray pattern prior shear was captured and subsequently, a shear pulse was applied with shear rates from 0 to 50 s<sup>-1</sup> and fixed shear duration of 5 s. After cessation of shear flow, the samples were isothermally crystallized at the shear temperature for about 280 s. At the end of the isothermal crystallization, the samples were cooled down to 80 °C at the cooling rate of about 20 °C/min. 2D-WAXS patterns with exposure period of 13 or 15 s and 2D-SAXS patterns with that of 18 or 20 s were continuously recorded immediately after cessation of shear. All of the X-ray patterns were corrected for background scattering, air scattering, and beam fluctuations.

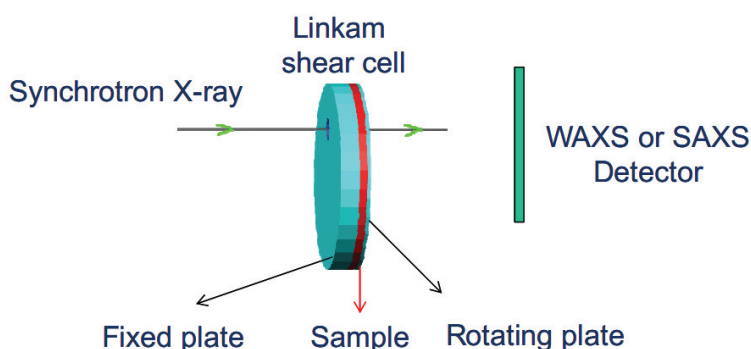


Fig. 8 Experimental setup, the fixed and rotating plate were made from kapton windows

#### 4.4 Morphological scan measurement

The morphological scanning measurement was carried out with the primary beam perpendicular to the injection direction and thickness direction of sample by vertically shifting the sample (Fig. 9). The synchrotron X-ray measurements were carried out at beamline P03 of Petra III, DESY, Hamburg, Germany (Fig. 10). The beam size was 20 x 20 μm<sup>2</sup> and the wavelength was 0.1069 nm. The exposure time was 0.5 s and the sampling rate was 0.33 s<sup>-1</sup>. Two-dimensional WAXS and SAXS patterns were collected using two separate detectors Pilatus 300K and Pilatus 1M (Paul Scherrer Institute, Switzerland), respectively, with a readout time of 3 ms. The sample to detector distance was 2600 mm for SAXS and 129.5 mm for WAXS. All of the X-ray patterns were corrected for background scattering, air scattering, and beam fluctuations. If not specially mentioned, the same X-ray scattering measurements were also applied to the subsequent tensile deformation measurement (section 4.5) and melt draw experiment (section 4.6)

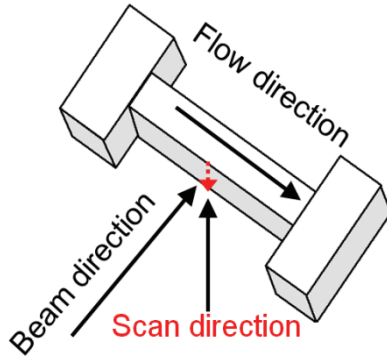


Fig. 9 Sketch of morphological scan measurement



Fig. 10 Petra III experimental hall Max-von-Laue (blue) provides the world most brilliant synchrotron radiation source through storage ring [133]

## 4.5 Tensile deformation measurement

Uniaxial tensile deformation was performed on a custom-made miniature tensile machine (Fig. 11) equipped with a heating device, which contained a porous ceramic material allowing generation of a homogenous heat convection [6]. The samples were symmetrically stretched at elevated temperatures from 70 to 110 °C under different stretching rates. A digital camera was used to follow in situ the deformation process of the sample without hindering the X-ray path. The strain  $\epsilon_t$  of the stretched sample was measured optically by observing the deformation of a grid pattern on the sample surface, with a mesh size of 0.35 mm, printed by using a self-made flexible ink. The centre of the specimen, which was irradiated by X-ray beam, was left blank. The samples were normally stretched to a strain of about 3.7.

The specimens were assumed to be incompressible, so the true stress  $\sigma_t$  can be calculated by Eq. (2), where  $F$  is the measured force and  $A$  is the initial cross section of the specimen.



$$\sigma_t = F \times (1 + \varepsilon_t)/A \quad (2)$$

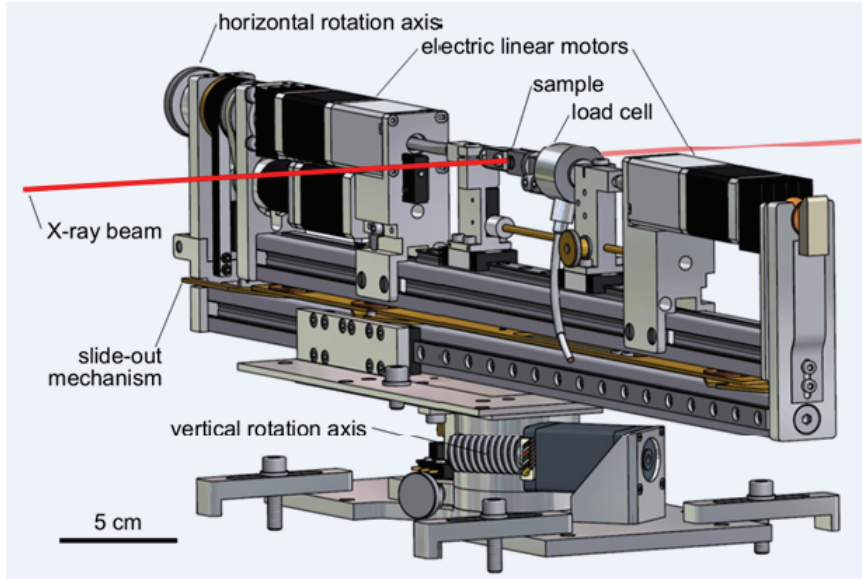


Fig. 11 Custom-made miniature tensile machine used in the synchrotron X-ray measurement [134]

## 4.6 Melt draw measurement

Melt draw experiment was performed on the same custom-made miniature tensile machine as described above. The experimental setup was illustrated in Fig. 12. The sample was firstly heated up to 210 °C at maximum heating rate of about 50 K/min and kept there for 5 min to erase the previous thermal and mechanical history. In order to prevent the sagging of the sample, the sample was held by a non-sticking support. After isothermal heat treatment at 210 °C, the sample was cooled down to the draw temperature of 138 °C at a cooling rate of about 40 K/min and held there for 2 min to achieve the thermal equilibrium. Then the supercooled sample was uniaxially drawn by 30 mm with a velocity of 3.9 mm/s, which corresponded to a strain rate of  $0.9 \text{ s}^{-1}$  and a strain of 700%. The strain was estimated by the displacement of ink marks pre-printed on the sample surface. The sample was held until the crystallization finished and was finally rapidly cooled down to the room temperature.

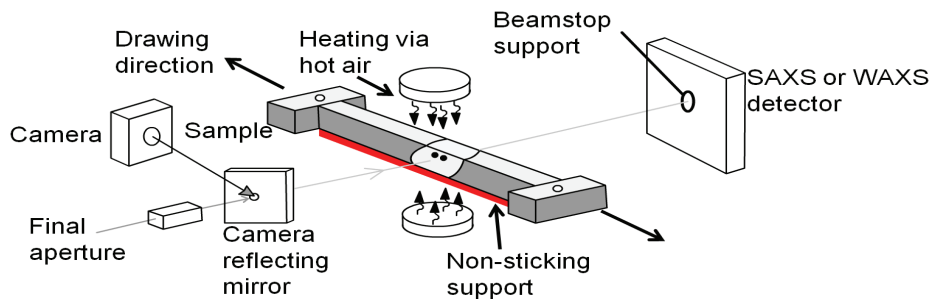


Fig. 12 Experimental setup for melt drawing

## **4.7 Polarized optical microscopy**

In-situ rheo-optical measurements were performed on an Olympus BH2 optical microscope (Japan), where samples were sandwiched between two original parallel quartz glass plates. The crystallization behaviour and optical morphology of the sample were observed with the aid of a digital camera Olympus DP71 under polarized light during shear-induced crystallization.

## 5 X-ray data evaluation

### 5.1 Basic properties of X-rays

In current thesis, in-situ wide angle X-ray scattering (WAXS) and small angle X-ray scattering (SAXS) are used to characterize phase behaviour, phase transition and structure formation of  $\beta$ -nucleated iPP during the flow (shear and extension)-induced crystallization as well as the deformation process. X-rays are short-wave electromagnetic radiation discovered by W.C. Roentgen in 1895. Their wavelengths, ranging from 0.01 to 10 nm, are commensurate with both the atomic sizes and shortest interatomic distances observed in polymer materials. When X-rays interact with a substance, they can be absorbed or scattered. The absorption leads to the dissipation of X-ray, while the scattering may change the direction of incident X-rays. During the scattering, the wavelength of X-ray may change or not change. The scattering with changed wavelength is termed as inelastic scattering or Compton scattering, while the scattering with unchanged wavelength is called elastic scattering. The effect of Compton scattering at low scattering angle is not essential and can be generally neglected in current thesis (scattering angle less than  $23^\circ$ ). Therefore, in the first approximation only elastic scattering leads to the diffraction from periodic structure and is taken into account in current scattering experiments [135].

X-ray scattering appears at differences in electron density, periodically distributed in the crystal lattices. A schematic illustration of scattering principle, which is based on the well-known Bragg's model, is shown in Fig. 13. Two parallel incident X-rays with identical wavelength and phase are scattered from a series of crystallographic planes. The path difference of incident and scattered X-rays between two neighbouring planes is  $|AO| + |BO|$  which is associated with interplanar distance  $d$ . The constructive interference is observed when Bragg condition is fulfilled, i.e.

$$n \cdot \lambda = 2d \cdot \sin \theta \quad (3)$$

where  $n$  is order of scattering and is taken as 1 in all calculations,  $\lambda$  is wavelength of incident X-rays, and  $2\theta$  is the scattering angle.

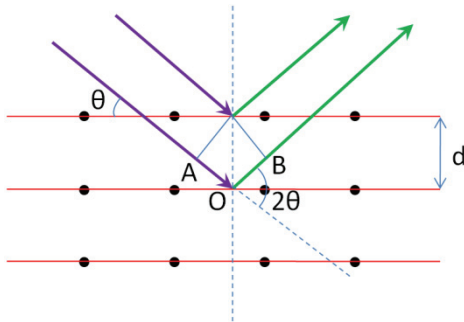


Fig. 13 Geometrical illustration of Bragg's model using 2D lattice

The corresponding angular distribution of the intensity reflects the structure of investigated material. However, the intensity is conventionally plotted as a function of the momentum transfer,  $q$ , which is associated with  $2\theta$  and is defined as

$$q = 4\pi \cdot \lambda^{-1} \cdot \sin \theta \quad (4)$$

Combining equations (3) and (4) produces

$$d = 2\pi/q \quad (5)$$

Eq. (5) indicates that the characteristic distance can be probed by a measurement at a given value of  $q$  [136]. The inverse relationship between structure in real-space ( $d$ ) and scattering in  $q$ -space suggests that Bragg's model is not solely valid in crystalline system, but applied to first order for different types of scattering at all length scales including WAXS and SAXS [136].

Combination of WAXS and SAXS techniques enables the structure in the range of a few angstroms to several hundred nanometers to be detected. Thus it is possible to follow the structure variation, including the crystallinity, crystal type, orientation of crystal, crystal size, lamellar structure, long period, crazes and voids, etc. It is expected that new insights about crystallization and deformation mechanism may be acquired during the flow-induced crystallization and deformation process, which are beneficial for optimization of material development.

## 5.2 Crystallinity, $\beta$ -content and crystal size

Assuming that sheared, melt-drawn and stretched samples have cylindrical rotation symmetry around shear, drawing and stretching direction, respectively, a 2D X-ray pattern can contain the complete information reflecting the intensity distribution in reciprocal space and can be used to calculate the fraction of each phase. To investigate the changes of crystallinity with time, the WAXS patterns were firstly azimuthally integrated and then a self-written peak-fitting procedure in PV-wave was used to separate the peaks in the WAXS profiles by Gaussian fit. The overall crystallinity index was calculated by Eq. (6), dividing the total crystalline peak areas by the total scattering area including crystalline and amorphous phase.

$$X_c = \frac{\sum A_{cryst}}{\sum A_{cryst} + A_{amorph}} \quad (6)$$

During the shear-induced and extension-induced crystallization, the content of  $\gamma$ -crystals can be neglected and the formed crystals are mainly the  $\alpha$ - and  $\beta$ -crystals. The relative amount of the  $\beta$ -crystals  $K_\beta$  was evaluated by the following empirical equation (7) proposed by Turner-Jones [137].  $A_\beta$

(3 0 0) is the area of the (3 0 0) reflection peak of the  $\beta$ -iPP,  $A_\alpha$  (1 1 0),  $A_\alpha$  (0 4 0), and  $A_\alpha$  (1 3 0) are the areas of the (1 1 0), (0 4 0), and (1 3 0) reflection peaks of the  $\alpha$ -iPP, respectively.

$$K_\beta = \frac{A_\beta(300)}{A_\beta(300) + A_\alpha(110) + A_\alpha(040) + A_\alpha(130)} \quad (7)$$

However, for injection moulding sample, certain  $\gamma$ -phase was found in the outer layer of iPP sheet and cannot be neglected in the morphological scan experiment. In this case, 3 kinds of crystal modifications usually coexisted in the iPP and the content of  $\beta$ -phase was minor. The relative amount of the  $\gamma$ -crystals  $K_\gamma$  was estimated also using the Turner-Jones method [137]:

$$K_\gamma = \frac{A_\gamma(117)}{A_\gamma(117) + A_\alpha(130)} \quad (8)$$

The Eq. (7) was then modified by the following equation:

$$K_\beta = \frac{A_\beta(300) \times (1 - K_\gamma)}{A_\beta(300) + (A_\alpha(110) + A_\alpha(040) + A_\alpha(130)) \times (1 - K_\gamma)} \quad (9)$$

The relative crystallinity of the  $\beta$ -form crystals  $X_\beta$ ,  $\gamma$ -form crystals  $X_\gamma$  and  $\alpha$ -form crystals  $X_\alpha$ , respectively were given by:

$$X_\beta = X_c \cdot K_\beta \quad (10)$$

$$X_\gamma = X_c \cdot K_\gamma \quad (11)$$

$$X_\alpha = X_c - X_\beta - X_\gamma \quad (12)$$

The crystal size was calculated from the full width at half-maximum (FWHM) of the fitted crystalline peaks according to the Debye-Scherrer equation [87]:

$$L_{hkl} = \frac{K\lambda}{\beta_{1/2} \cos \theta} \quad (13)$$

Here  $L_{hkl}$  represents the mean crystallite size in the normal direction of the (h k l) reflection plane and  $\beta_{1/2}$  is the FWHM of the diffraction peak (h k l) in radians. The shape factor K was set as 0.9 for polymer systems [89, 93, 138].

### 5.3 Long period and lamella thickness

The long period, spacing between adjacent crystalline lamellae layers, can be estimated from circular averaged 1-D SAXS data by using the following Eq. (14) [9, 96] derived from the Bragg's law:

$$L_B = \frac{2\pi}{q_{max}} \quad (14)$$

Where  $q_{max}$  represents the peak position in Lorentz corrected scattering intensity plot. Combining with the crystallinity obtained from WAXS, one can estimate the lamellar thickness ( $L_c$ ) distribution of  $\beta$ -nucleated iPP by Eq. (15) [114]

$$L_c = L_B \cdot X_c \quad (15)$$

### 5.4 Orientation degree

From the WAXS pattern, the crystalline orientation can be estimated using the Hermans' orientation function [139] defined as follows:

$$f_H = \frac{3 \langle \cos^2 \varnothing \rangle - 1}{2} \quad (16)$$

where  $\varnothing$  is the angle between the normal to the (0 4 0) reflection plane and the reference axis (a direction perpendicular to flow direction in 2D-WAXS pattern). The term  $\langle \cos^2 \varnothing \rangle$  is defined as

$$\langle \cos^2 \varnothing \rangle = \frac{\int_0^{\pi/2} I(\theta) \cos^2(\theta) \sin(\theta) d\theta}{\int_0^{\pi/2} I(\theta) \sin(\theta) d\theta} \quad (17)$$

with the intensity  $I(\theta)$  obtained from the scattering at the azimuthal angle  $\theta$  of the (0 4 0) reflection ring in 2D-WAXS pattern. The  $f_H$  has a value of unity when the reflection plane is parallel to the flow direction ( $\varnothing = 0^\circ$ ), a value of -0.5 when the reflection plane is perpendicular to the flow direction ( $\varnothing = 90^\circ$ ) and a value of 0 when the reflection plane has no preferred orientation.

## 6 Results and discussion

### 6.1 Crystallization under quiescent condition

#### 6.1.1 Morphology of $\beta$ -nucleating agent

The morphology of  $\beta$ -nucleating agent in the iPP melt during cooling is shown in Fig. 14, which was captured by optical microscopy under quiescent condition, immediately after the temperature reaching 138°C. As can be seen, in the case of Bpp1, the  $\beta$ -nucleating agent seemed totally dissolved in the polymer melt and there was no NJS recrystallized from the melt. The black point should be related to the impurity. In the case of Bpp2, needle like crystals with aspect ratio of about 10 were formed and they should be related to the recrystallization of NJS during cooling. In the case of Bpp3, it seems that there were a lot of non-dissolved isotropic particles of NJS in the melt.

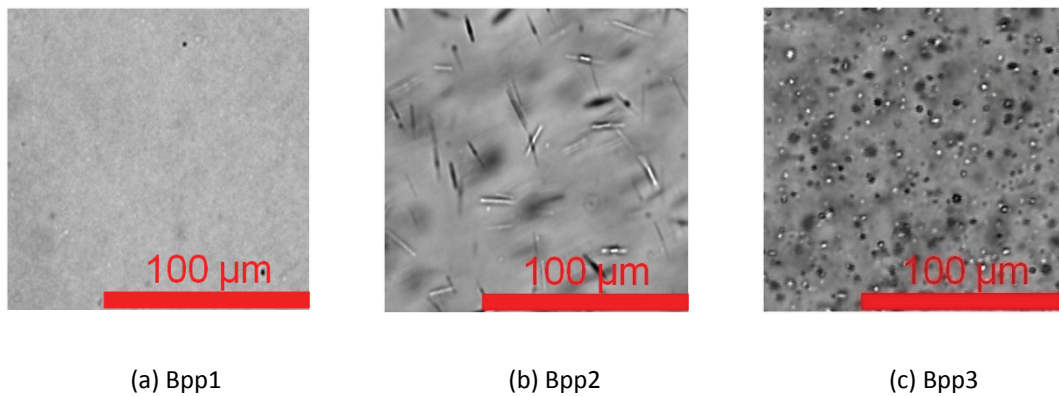


Fig. 14 Morphology of  $\beta$ -nucleating agent at different concentrations in the iPP melt (0.01 (a), 0.03 (b) and 0.1 wt% (c))

#### 6.1.2 Crystallization kinetics under quiescent condition

Fig. 15 shows the evolution of crystallinity for iPP samples containing different concentrations of  $\beta$ -nucleating agent during the quiescent isothermal crystallization at 138 °C.

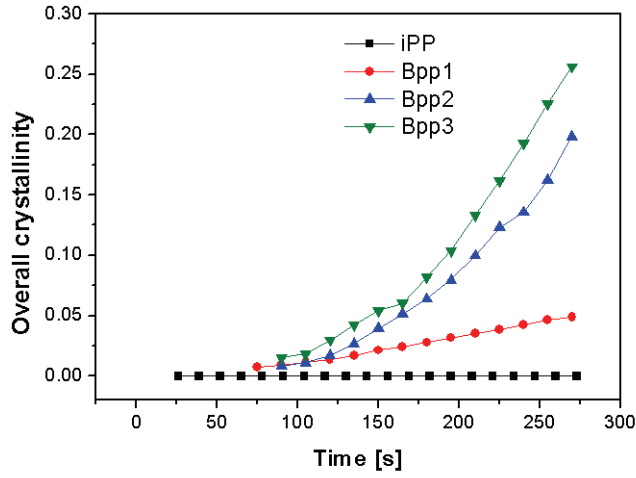


Fig. 15 The overall crystallinity as a function of time during the quiescent crystallization at 138 °C

It can be seen that no crystallization in pure iPP was detected by X-ray during the given crystallization process and the addition of nucleating agent obviously accelerated the crystallization. The Avrami equation (Eq. (1)) was widely used to study the isothermal crystallization of polymer material [45]. For small values of  $X_t$ , the exponential function can be approximated by a Taylor series as  $\exp(-kt^n) \approx 1 - kt^n + \dots$ , thus the Avrami equation can be approximated in this region as

$$\frac{X_t}{X_\infty} \approx kt^n \quad (18)$$

or

$$\ln(X_t) \approx \ln(X_\infty \cdot k) + n \cdot \ln(t) \quad (19)$$

Hence, the Avrami exponent  $n$  and a constant  $A = X_\infty \cdot k$  can be obtained from the gradient and intercept, respectively, of the plot  $\ln(X_t)$  vs.  $\ln(t)$ . Fig. 16 shows the double-logarithmic Avrami plot for the different iPP samples. From Fig. 16, it can be seen that the Avrami exponents of both Bpp2 and Bpp3 are close to 3, indicative of 3-dimensional heterogeneous crystal growth, while Avrami exponent of Bpp1 is 1.5, indicating the occurrence of quasi rod-like crystal growth, which will be explained later.



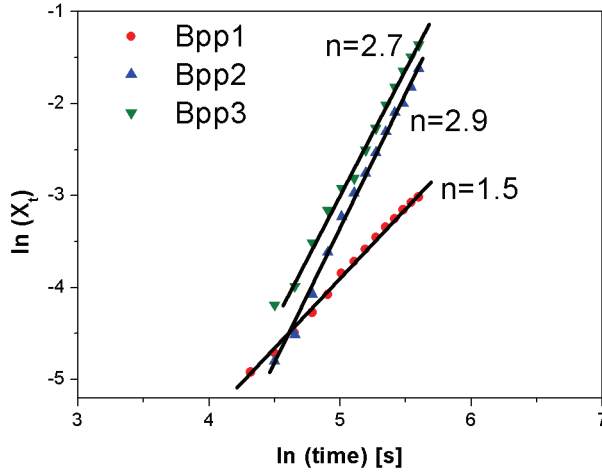


Fig. 16 Avrami plots of  $\ln(X_t)$  vs  $\ln(t)$  for quiescent isothermal crystallization of iPP containing different concentrations of  $\beta$ -nucleating agent at 138°C

The initially formed structure usually dictates the subsequent morphology development and as consequence, determines the final properties of polymer material. Hence, the current study was focused on the crystallization at the initial stage and the isothermal crystallization was performed only in a short time, during which the crystallization is incomplete. To roughly compare the crystallization rates of different samples at the initial stage, an average crystallization rate  $G$  is introduced, which is defined as

$$G = \frac{X(t_{ref})}{t_{ref}} \quad (20)$$

where  $X(t_{ref})$  and  $t_{ref}$  are the reference crystallinity and time at the end of given isothermal crystallization, respectively (for Bpp1, Bpp2 and Bpp3  $t_{ref} = 270$  s, and for iPP  $t_{ref} = 273$  s). The values of crystallization rate  $G$  of different iPP samples were listed in Tab. 2. It can be seen that the overall crystallization rate increased, as expected, with increasing concentration of  $\beta$ -nucleating agent under quiescent isothermal crystallization.

Tab. 2 Kinetics parameters for iPP samples containing different concentrations of  $\beta$ -nucleating agent during isothermal crystallization

Sample	Shear rate (/s)	n			$G \times 10^4 (s^{-1})$		
		Overall	$\alpha$	$\beta$	Overall	$\alpha$	$\beta$
iPP	0	-	-	-	0	0	0
Bpp1	0	1.5	-	1.5	1.8	0	1.8
Bpp2	0	2.9	2.2	3.8	7.4	4.0	3.4
Bpp3	0	2.7	2.4	3.0	9.5	3.5	6.0
iPP	50	1.0	1.0	1.8	1.8	1.7	0.1
Bpp1	50	1.2	0.93	1.4	4.9	2.0	2.9
Bpp2	50	1.7	1.7	2.0	7.6	7.0	0.6
Bpp3	50	1.6	1.6	1.9	13.2	12.4	0.8

After the isothermal crystallization, the samples were cooled to 80 °C, at which the iPP samples can be regarded as completely solidified. The corresponding crystallization states at 80 °C for different iPP samples are listed in Tab. 3, from which it can be seen that the  $\beta$ -crystal fractions (i.e.,  $K_\beta$  value) of these three  $\beta$ -nucleated iPP samples were all above 60% under quiescent crystallization, indicating that the  $\beta$ -nucleating ability of NJS was relatively high. Generally, in the solid state the fraction of  $\beta$ -crystals increased with increasing  $\beta$ -nucleating concentration. Surprisingly, Bpp1 exhibited highest  $\beta$ -crystal fraction (nearly equal to 100%) during isothermal crystallization, which can be seen from the evolution of  $K_\beta$  value with time in Fig. 17, though Bpp1 contains minimal  $\beta$ -nucleating agent. This should be related to the finely dissolved NJS, which crystallized during the holding time and self-assembled into very fine dendrite-like crystals with a radial multidirectional framework [118, 127]. Those newly formed crystals have very high selectivity which helps induce the formation of nearly pure  $\beta$ -crystals at the beginning of crystallization. Fig. 18 shows a PLM micrograph of Bpp1 quiescently crystallized at 138 °C. It can be noticed that many fibril-like crystalline units were induced by the specific crystal structure of  $\beta$ -nucleating agent, which should be the reason that the obtained Avrami exponent was around 1.5 for Bpp1 (Tab. 2). Comparing to Bpp1, the  $K_\beta$  values of Bpp2 and Bpp3 were

relatively low which may be attributed to the pre-existed NJS particles with dual nucleating ability inducing both  $\alpha$ - and  $\beta$ -crystals. During the isothermal crystallization, their  $\beta$ -crystal fractions increased with time indicating that the  $\beta$ -nucleating ability was enhanced with time leading to the accelerated formation of  $\beta$ -nuclei. It was also possible that the growth rate of  $\beta$ -crystals was faster than that of  $\alpha$ -crystals at the set crystallization temperature.

Tab. 3 Crystallization states at 80 °C for iPP samples containing different concentrations of  $\beta$ -nucleating agent. Firstly, the samples were isothermally crystallized at 138 °C for 280 s and then cooled to 80 °C, at which the crystallization was basically complete.

Sample	Shear rate (/s)	Overall crystallinity	$\alpha$ -crystallinity	$\beta$ -crystallinity	$K_{\beta}$ value	Orientation degree
iPP	0	0.55	0.55	0	0	
Bpp1	0	0.50	0.19	0.31	0.62	
Bpp2	0	0.55	0.20	0.35	0.63	
Bpp3	0	0.57	0.16	0.41	0.72	
iPP	50	0.59	0.44	0.15	0.25	0.023
Bpp1	50	0.55	0.19	0.35	0.64	0.16
Bpp2	50	0.53	0.44	0.094	0.18	0.24
Bpp3	50	0.48	0.45	0.036	0.075	0.22

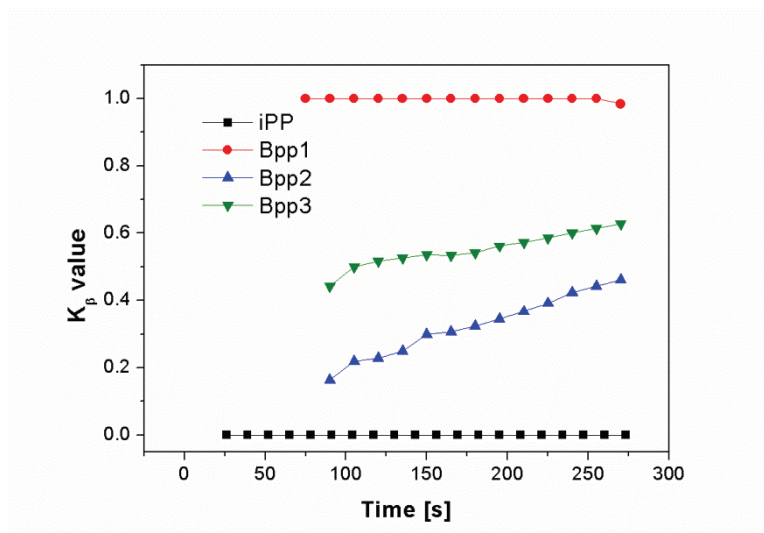


Fig. 17 The  $K_{\beta}$  (relative amount of  $\beta$ -crystals) value as a function of time during the quiescent crystallization at 138 °C

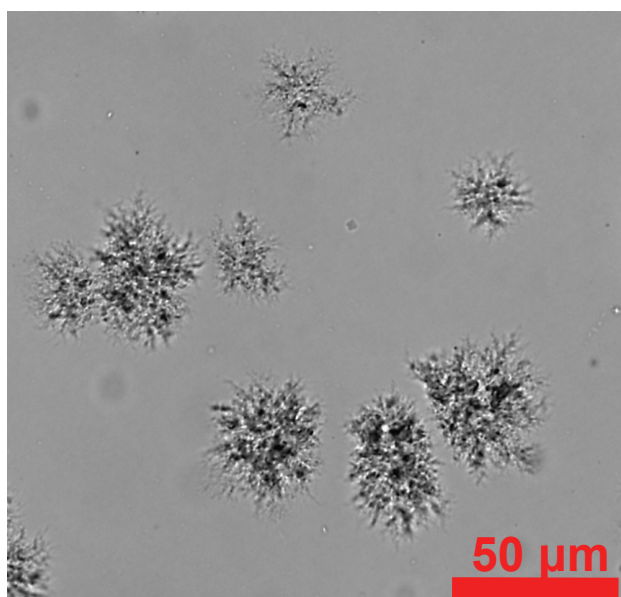


Fig. 18 PLM micrograph of Bpp1, quiescently crystallized at 138°C,  $t_c = 1.5$  min

### 6.1.3 Evolution of long period under quiescent condition

Fig. 19 shows the long period changes with time for the  $\beta$ -nucleated iPP (note: the data of pure iPP are omitted since no lamellar structure can be detected during this given isothermal crystallization process). In general, Bpp1 exhibited the highest value of long period at the initial crystallization, which can be attributed to the formation of nearly pure  $\beta$ -crystals having long lamellar distance compared to that of  $\alpha$ -crystals [12, 19]. The long period of Bpp3 was higher than the Bpp2, which can also be ascribed to the higher content of  $\beta$ -crystals in the Bpp3. Generally, the long period of Bpp1 decreased

with time which may be explained by formation of secondary lamellae on the primary lamellar stacks or insertion of newly formed lamellar stacks into the existing lamellar structure [9, 42]. In contrast, in the overall range (excluding the initial part) the long period of Bpp2 and Bpp3 tended to increase slightly with time, which may be mainly ascribed to the increase of  $\beta$ -content during crystallization. Although from current result we may not know the evolution of long period for pure iPP at this temperature, it is reasonable to assume that the long period of iPP at the later stage of isothermal crystallization should be less than that of Bpp2 [12].

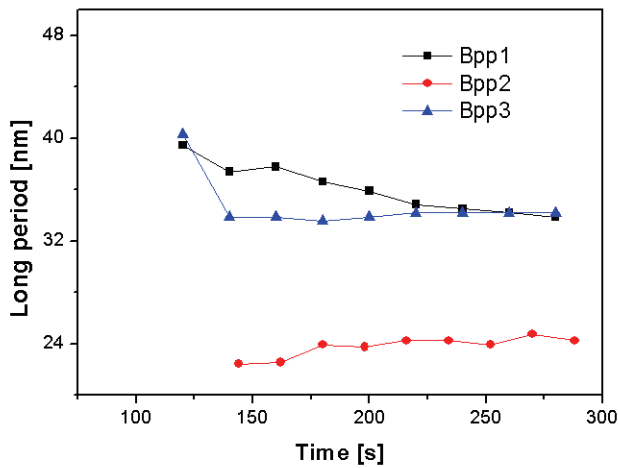


Fig. 19 The long period as a function of time during the quiescent crystallization at 138 °C

## 6.2 Shear induced crystallization

### 6.2.1 Influence of NJS concentration on the shear induced crystallization

#### 6.2.1.1 Overall crystallization kinetics after step shear

Fig. 20 shows the changes of crystallinity of different iPP samples after application of shear (for comparison, the quiescent data are also added). The corresponding Avrami plot is illustrated in Fig. 21 and the kinetic parameters are summarized in Tab. 2. It can be seen from Tab. 2 that after step shear the overall Avrami exponent of iPP was about 1 indicating a rod-like crystal growth due to the development of shear-induced linear primary nuclei at the initial crystallization [71]. In addition, the Avrami exponent of three  $\beta$ -nucleated iPP samples was reduced with Bpp1 having  $n$  about 1.2 indicative of rod-like crystal growth geometry, and Bpp2 having  $n \sim 1.7$  as well as Bpp3 having  $n \sim 1.6$  suggestive of mixed rod-like and disk-like growth. As can be seen from the Tab. 2, the overall rate parameter  $G$  for pure iPP, Bpp1 and Bpp3 markedly increased after application of shear indicating the acceleration of crystallization kinetics, while for Bpp2 it increased only slightly indicating the shear increased little if any crystallization rate. Shear and the addition of particles have been suggested to

generate a synergistic increase in the number of active nuclei, thus increase polymer crystallization rate. However, our result showed that the kinetics of shear induced crystallization was complicated especially at the presence of nucleator. The reason for the nearly unchanged crystallization rate of Bpp2 will be explained later. If we check the evolution of  $K_\beta$  value with time (Fig. 22), it can be seen that all of the  $K_\beta$  values of  $\beta$ -nucleated iPP sample decreased compared with that of quiescent condition, this result was corresponding to [12, 17]. To elucidate this phenomenon, individual crystallinity as a function of time was analyzed.

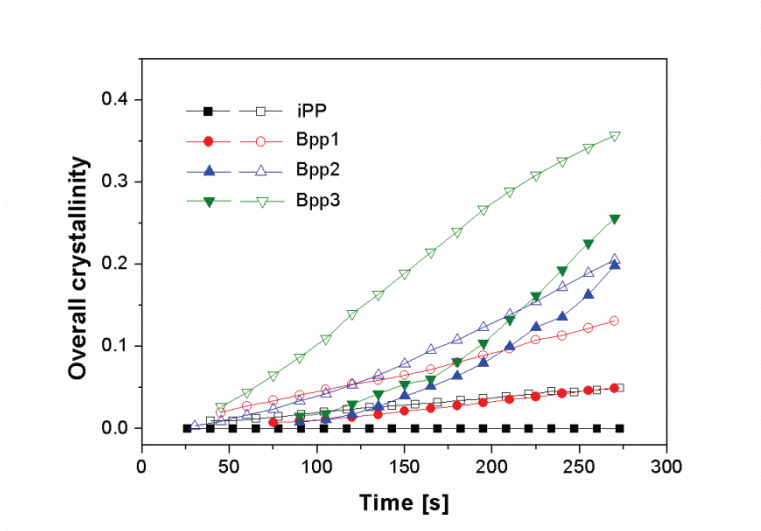


Fig. 20 The overall crystallinity of iPP with different concentrations of  $\beta$ -nucleating agent as a function of time during the quiescent crystallization (solid symbols) and flow-induced crystallization with shear rate of 50 /s (open symbols) at 138 °C

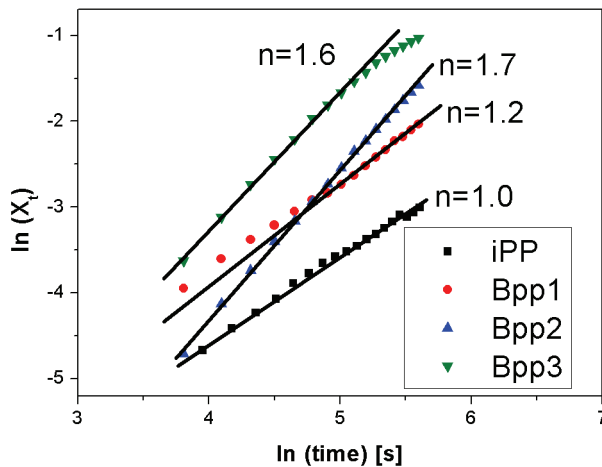


Fig. 21 Avrami plots of  $\ln(X_t)$  vs  $\ln(t)$  for shear-induced crystallization of iPP containing different amounts of  $\beta$ -nucleating agent at 138 °C

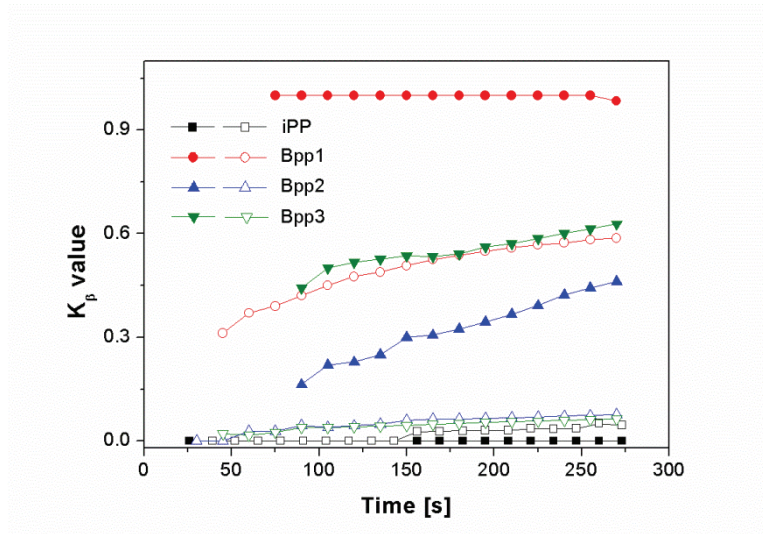


Fig. 22 The  $K_{\beta}$  value (relative amount of  $\beta$ -crystals) of iPP with different concentrations of  $\beta$ -nucleating agent as a function of time during the quiescent crystallization (solid symbols) and flow-induced crystallization with shear rate of 50 /s at 138 °C (open symbols)

### 6.2.1.2 Crystallization kinetics of $\alpha$ crystals

Fig. 23 illustrates the evolution of  $\alpha$ -crystallinity with time. In the case of pure iPP, no  $\alpha$ -crystal was detected by WAXS during the quiescent isothermal crystallization. With application of shear,  $\alpha$ -crystals appeared and grew with time due to the effect of shear on the iPP melt itself which generated a certain number of  $\alpha$ -crystal precursors. From Fig. 23 it can also be seen that the development of  $\alpha$ -crystallinity of iPP nucleated with 0.01 wt % NJS (Bpp1) was almost coincident with pure iPP, not only during quiescent crystallization but also during shear induced crystallization, indicating that the totally dissolved  $\beta$ -nucleating agent at lower concentration did not influence the  $\alpha$ -crystallization kinetics, or in other words, the development of  $\alpha$ -crystals of Bpp1 at 138 °C was mainly due to iPP polymer itself. For both pure iPP and Bpp1 the Avrami exponent of  $\alpha$ -crystals was close to 1 indicative of rod-like crystal growth geometry (Tab. 2). On the other hand, solid nucleating particles existed in the melt of iPP nucleated with NJS at higher concentrations of 0.03 wt% (Bpp2) and 0.1 wt% (Bpp3). Due to their dual nucleating ability, these solid particles can provide a large number of heterogeneous nucleation sites for the nucleation and growth of  $\alpha$ -crystals. As a result, under quiescent condition the  $\alpha$ -crystallization rate of Bpp2 and Bpp3 was higher than that of pure iPP (Tab. 2). The application of external shear flow further accelerated the crystallization of  $\alpha$ -crystals with the acceleration effect for Bpp3 being more pronounced than that for Bpp2 (Tab. 2). The  $\alpha$ -crystal dimensionality of both Bpp2 and Bpp3 changed from quasi-spherulitic to more disklike growth, due to the Avrami exponent varying from about 2.3 to about 1.7 (Tab. 2). In addition to the effect of shear on the iPP melt itself, the increase of  $\alpha$ -crystallization rate can also be attributed to the interaction between melt and solid  $\beta$ -nucleating agent under shear flow [12, 18]. The shear effect will be enhanced around the particles.

The molecular chains will be strongly stretched and form stable nuclei which surround the particle. Such interaction tended to be enhanced with the increasing concentration of  $\beta$ -nucleating agent.

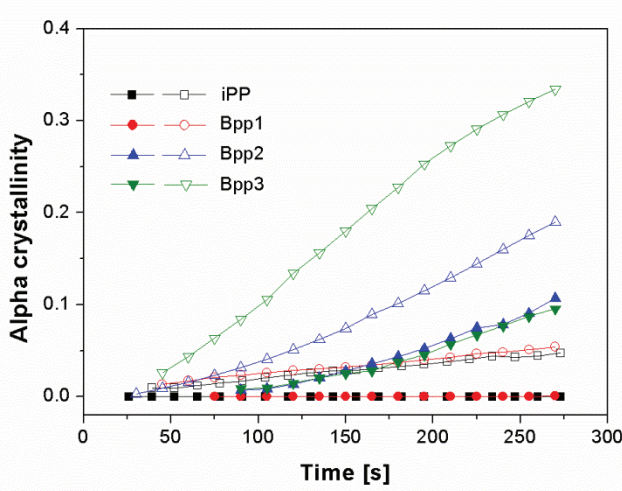


Fig. 23 The  $\alpha$ -crystallinity of iPP with different concentrations of  $\beta$ -nucleating agent as a function of time during the quiescent crystallization (solid symbols) and flow-induced crystallization with shear rate of 50 /s at 138 °C (open symbols)

### 6.2.1.3 Crystallization kinetics of $\beta$ -crystals

The development of  $\beta$ -crystallinity for iPP samples containing different concentrations of  $\beta$ -nucleator is shown in Fig. 24. For pure iPP the application of shear flow resulted in the formation of a few amount of  $\beta$ -crystals, which were formed after emergence of  $\alpha$ -crystals. The formation of  $\beta$ -crystals can be attributed to the  $\alpha$  to  $\beta$  growth transition taking place on the surface of the primary shear-induced  $\alpha$ -row nuclei [15]. For Bpp1 it can be seen that the  $\beta$ -crystallization rate (Tab. 2) increased after applying shear indicating the occurrence of the  $\alpha$  to  $\beta$  growth transition or an enhanced  $\beta$ -nucleating efficiency of NJS under shear. In the case of Bpp2 and Bpp3 it can be seen that both  $\beta$ -crystallization rates were strongly decreased comparing to quiescent condition, indicating that shear hindered the development of  $\beta$ -crystals. This should be the reason for the nearly unchanged overall crystallization rate of Bpp2. On the other hand, the increase of overall crystallization rate of Bpp3 was mainly attributed to shear induced crystallization of  $\alpha$ -crystals. It seemed that the higher  $\beta$ -nucleating ability was preferred at quiescent condition. According to Huo [17] and Hsiao [12], the nucleating property of  $\beta$ -nucleating agent actually has not changed after application of shear. The strong decrease of  $\beta$ -crystallization rate may be related to the change of environment around the particles of  $\beta$ -nucleating agent, which will be elucidated in detail later.



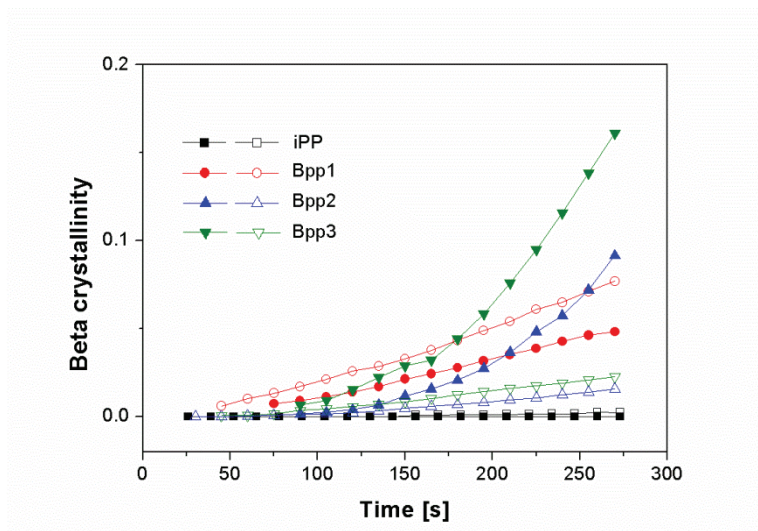


Fig. 24 The  $\beta$ -crystallinity of iPP with different concentrations of  $\beta$ -nucleating agent as a function of time during the quiescent crystallization (solid symbols) and flow-induced crystallization with shear rate of 50 /s at 138 °C (open symbols)

#### 6.2.1.4 Crystal orientation

Under shear flow the molecular chains may be stretched and form crystals with certain degree of orientation. Fig. 25 shows the evolution of orientation degree, calculated from  $\alpha$ -(0 4 0) reflection, with time for iPP nucleated with different concentrations of NJS after application of shear flow. It can be seen that all samples exhibited high orientation degree about 0.95 at the beginning of crystallization. For iPP and Bpp1 the degree of orientation decreased much slower during the isothermal crystallization compared with the samples of Bpp2 and Bpp3. It can also be observed that sheared iPP and Bpp1 exhibited similar evolution trend of orientation degree of  $\alpha$ -crystals. This result was consistent with the development of  $\alpha$ -crystallinity of both samples (Fig. 23), indicating that  $\beta$ -nucleating agent at low concentration affected little if any the shear-induced crystallization of  $\alpha$ -crystals. This finding is different with Huo et al. [17], who suggested that the dispersed additives at low concentration would restrain the formation of oriented  $\alpha$ -nuclei and then causes the induced  $\beta$ -phase crystallinity to decrease.

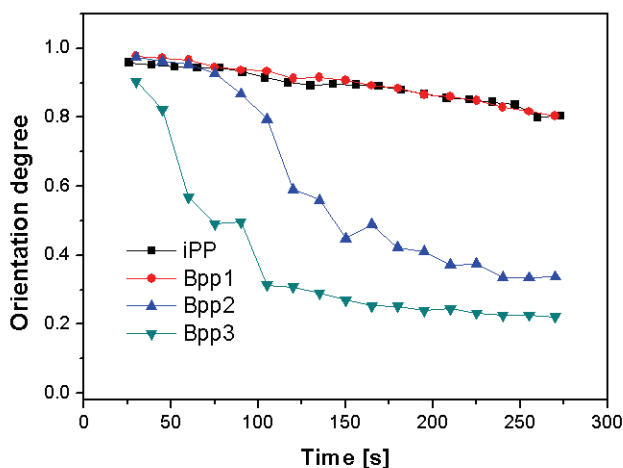


Fig. 25 The orientation degree, calculated from (0 4 0) reflection, of iPP with different concentrations of  $\beta$ -nucleating agent as a function of time during flow-induced crystallization with shear rate of 50 /s at 138 °C

Though the addition of small amount of  $\beta$ -nucleating agent did not change the crystallization of  $\alpha$ -crystals, it did not mean that it lost its effectiveness and had no influence on the orientation behaviour of  $\beta$ -crystals. Fig. 26 shows the 2D-WAXS patterns for sheared iPP nucleated with different concentrations of NJS at the end of given isothermal crystallization at 138 °C. Six circles from inside to outside represent the diffractions of  $\alpha$ -(1 1 0),  $\beta$ -(3 0 0),  $\alpha$ -(0 4 0),  $\alpha$ -(1 3 0),  $\beta$ -(3 1 1)/ $\alpha$ -(1 1 1) and  $\alpha$ -(0 4 1), respectively. It is quite clearly observed from the figure that for pure iPP (Fig. 26 a) the (3 0 0) reflection of  $\beta$ -crystals was arc-like indicating the formation of oriented  $\beta$ -crystals induced by the shear-induced  $\alpha$ -row nuclei, while for Bpp1 (Fig. 26 b), the (3 0 0) reflection exhibited almost isotropic, indicating the spontaneous growth of  $\beta$ -crystals during the shear induced crystallization. Combining with the notable increase of  $\beta$ -crystallinity of Bpp1 after application of shear flow (Fig. 24), the following scenario can be envisaged: before applying shear, the totally dissolved  $\beta$ -nucleating agent in Bpp1 was already saturated. The application of shear may accelerate the nucleation and growth of  $\beta$ -nucleating agent. As a result, those advanced formed fine crystals of  $\beta$ -nucleating agent may promote the nucleation and growth of  $\beta$ -crystals without specific orientation during crystallization. In addition, the  $\beta$ -crystal dimensionality of sheared Bpp1 is mixed rod-like and disk-like growth with Avrami exponent  $n$  about 1.4, similar to that of quiescent one ( $n$  about 1.5) (Tab. 2).

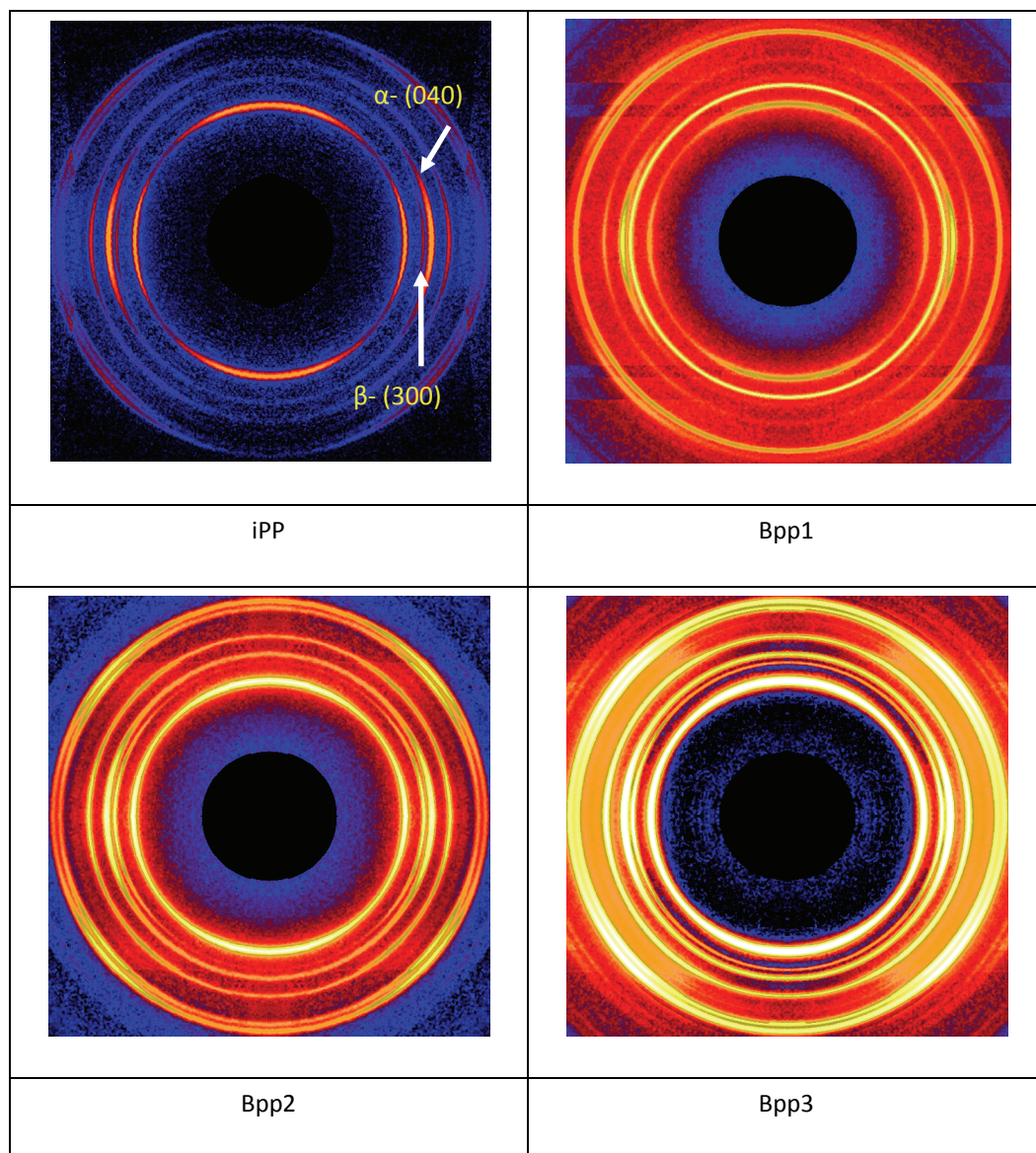


Fig. 26 2D-WAXS patterns for sheared iPP nucleated with different concentrations of NJS at the end of given isothermal crystallization at 138 °C. For enhancing the scattering contrast a modification was applied here, i.e., by subtraction of the original pattern with the pattern just prior to the application of shear

For sheared Bpp2 and Bpp3 the degree of orientation decreased quickly at the beginning of crystallization (Fig. 25). The existence of  $\beta$ -nucleating particles made the strain environment of iPP melt complicated. On the one hand the flow intensity may be significantly increased around the particles resulting in the formation of more nuclei [13, 132] and thus acceleration of crystallization kinetics (Fig. 23 and Tab. 2). On the other hand, molecular chains may change their initial streamline when passing by the particles. This may lead to the formation of nuclei with orientation deviated from the flow direction resulting in reduction of overall degree of orientation. In addition, the faster decrease of overall orientation degree may also be associated with the faster relaxation rate of

row/thread-like nuclei induced by the particles under shear flow. Those nuclei contained larger amount of lower molecular weight chains, which tended to relax quickly and formed point-like nuclei to induce isotropic crystal growth [74, 132]. Although the degree of orientation decreased quickly in the presence of  $\beta$ -nucleating particles, it did not mean that the  $\beta$ -nucleating agent was not beneficial for improving molecular alignment during processing. From Tab. 3, it can be seen that in the final solid state the degree of orientation of iPP containing  $\beta$ -nucleating particles (Bpp2 with 0.24 and Bpp3 with 0.22) was higher than that without  $\beta$ -nucleating particles (pure iPP with 0.023 and Bpp1 with 0.16). Although pure iPP and Bpp1 exhibited high degree of orientation during the isothermal period, their crystallinity is relatively low even at the end of isothermal crystallization. During cooling a large amount of isotropic nuclei may be formed which strongly reduced the overall degree of orientation. The relatively high orientation degree of Bpp2 and Bpp3 in final solid state indicated that the nucleating agent particles indeed promote the alignment of molecular chains along the flow direction during the processing. In addition, it can also be observed that in the overall range the orientation degree of Bpp2 was higher than that of Bpp3, not only during the isothermal crystallization, but also in the final solid state (Tab. 3). This result was consistent with Phillips et al. [132] and indicated that the anisotropic shape of  $\beta$ -nucleating agent in Bpp2 was much more effective to align the molecular chains along the flow direction compared to the isotropic one in Bpp3. The stronger alignment effect of anisotropic particles should also be the underlying reason that greater numbers of nuclei were generated during shear induced crystallization as reported by Byelov et al. [18]. In addition, it is worth pointing out that after application of shear, no  $\beta$ -crystals formed in Bpp2 at the beginning of crystallization and only the  $\alpha$ -crystals formed (Fig. 22), which highly oriented in the flow direction (Fig. 25). This result is different with Hsiao et al. [12], who reported that  $\beta$ -crystals always formed firstly in  $\beta$ -nucleated iPP during shear induced crystallization.

#### **6.2.1.5 Interaction of NJS particles with the polymer melt after step shear**

As can be obviously seen in Fig. 26 c, the (3 0 0) reflection of Bpp2, similar to pure iPP, was arc-like and the scattering mainly focused at the equator, which was different with that of Bpp1. It is worth to point out that the oriented  $\beta$ -crystals should be primarily induced by the oriented  $\alpha$ -row nuclei and not the  $\beta$ -nucleating agent itself. The reason is as follows: under shear flow the needle-like  $\beta$ -nucleating agent would preferentially orient with their long axis along the flow direction. According to Yamaguchi et al. [20, 21], if  $\beta$ -crystals directly grow, like that under quiescent condition, on the surface of the oriented  $\beta$ -nucleating agent, their c-axis would orient perpendicular to the long axis of needle-like  $\beta$ -nucleating agent crystals, i.e., the flow direction. As a result, a specific WAXS pattern can be acquired, i.e., six distinct spots should display on the (3 0 0) reflection [20, 21], which, however, were not observed in current study. In addition, the Avrami exponents of  $\beta$ -crystals of both Bpp2 ( $n \sim 2.0$ ) and Bpp3 ( $n \sim 1.9$ ) were close to that of pure iPP ( $n \sim 1.8$ ) (Tab. 2) further implying that the nucleation mechanism of  $\beta$ -crystals in iPP containing  $\beta$ -nucleating particles was similar to that in pure iPP. Thus, the effect of  $\beta$ -nucleating agent itself can be substantially excluded on inducing the formation of the

oriented  $\beta$ -crystals. The property or structure of the  $\beta$ -nucleating agent did not change after shear [12, 17]. The strongly reduced effectiveness of NJS in inducing the formation of  $\beta$ -crystals may be related to the change of environment around the  $\beta$ -nucleating agent particles. Under shear, a large amount of oriented  $\alpha$ -nuclei formed around the  $\beta$ -nucleating agent. The resultant  $\alpha$ -crystals grew rapidly and formed possibly an encapsulated network surrounding the  $\beta$ -nucleating agent thus inhibiting the formation of  $\beta$ -crystals on the surface of  $\beta$ -nucleating agent. In addition, it is also possible that under isothermal condition new fine  $\beta$ -nucleating agent crystals can hardly be formed at the presence of preformed particles. The concentration of  $\beta$ -nucleating agent outside the particles maybe saturated for the large particles and was beneficial for the further growth of pre-existed particles, however, unsaturated for the fine nuclei with large surface area to volume ratio and hence high solubility in the polymer melt. Thereby, after step shear it was inadequate for the formation of new small nuclei to promote the nucleation and growth of  $\beta$ -crystals, which was different with the case of Bpp1. The situation of (3 0 0) reflection of Bpp3 (Fig. 26 d) was similar to that of Bpp2 (Fig. 26 c). Though Bpp3 contained particles with isotropic shape, the formation of oriented  $\beta$ -crystals still can be mainly attributed to the oriented  $\alpha$ -row nuclei. Both the inhibition of growth of  $\beta$ -crystals on the pre-existed NJS particles and deficiency of new fine NJS nuclei after step shear should also be the reasons for the little content of  $\beta$ -crystals in the solid state with Bpp3 exhibiting even less  $\beta$ -crystal content than Bpp2 (Tab. 3), indicating that the development of  $\beta$ -crystals was retarded with increasing concentration under shear.

#### **6.2.1.6 Evolution of long period after application of shear**

Fig. 27 shows the long period changed with time for different samples during the shear induced crystallization. The long period of pure iPP was around 25.5 nm, which should be higher than that under quiescent condition according to Hsiao et al. [12, 140], who reported that shear may increase the distance between lamellar stacks. The Bpp1 exhibited larger long period than pure iPP which may be attributed to the higher  $\beta$ -content formed during the crystallization. On the other hand, the  $\alpha$ -crystals were dominant in the sheared Bpp2 and Bpp3 during isothermal crystallization (Fig. 22), however, the long period in Bpp2 and Bpp3 was large compared to that in pure iPP, which was possibly associated with the formation of highly stretched molecular chains surrounded the particles directing the subsequent formation of lamellae with increased stacks distance. In addition, after application of shear, the long period of both Bpp1 and Bpp3 was decreased, while that of Bpp2 was slightly increased compared with that under quiescent condition (Fig. 19) indicating that shear strongly changed the stacking manner of lamellae during the isothermal crystallization. The decrease of long period of both Bpp1 and Bpp3 can be mainly attributed to the reduced content of  $\beta$ -crystals, while the increase of long period of Bpp2 was mainly ascribed to the highly stretched polymer chains as mentioned above.

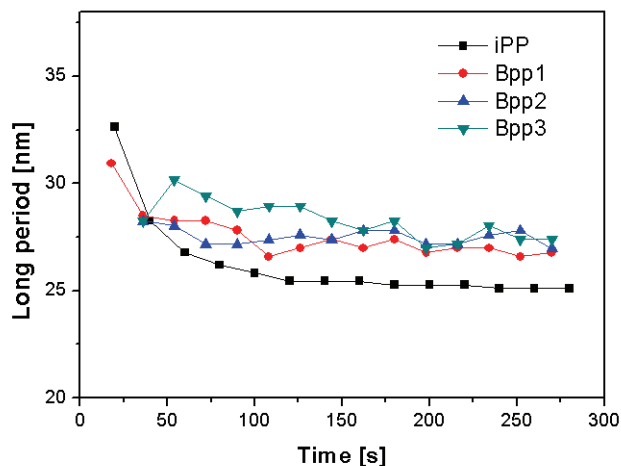


Fig. 27 The long period of iPP with different concentrations of  $\beta$ -nucleating agent as a function of time during flow-induced crystallization with shear rate of 50 /s at 138 °C

#### 6.2.1.7 Proposed crystallization mechanism

Fig. 28 shows the proposed crystallization mechanism of iPP with  $\beta$ -nucleating agent particles under the influence of shear. Before applying shear, the molecular chains and particles were randomly distributed in the polymer melt (Fig. 28 a). Upon imposition of shear, molecular chains and anisotropic particles were oriented in the flow direction. In the vicinity of particles, the velocity gradient was much higher than that far away from the particles. As a consequence, the molecular chains were highly stretched and much more  $\alpha$ -row nuclei were generated around the particles (Fig. 28 b). Those nuclei grew very fast into  $\alpha$ -crystals and possibly impacted each other to form an encapsulated network which strongly retarded the  $\beta$ -nucleating efficiency of this nucleating agent (Fig. 28 c: note: for simplification the relaxation of the row nuclei and the possible branches of lamellae were ignored). During the shear-induced crystallization, it is possible that some  $\beta$ -crystals grew epitaxially on the oriented row-nuclei. However, their content was limited due to the quick development of  $\alpha$ -crystals.

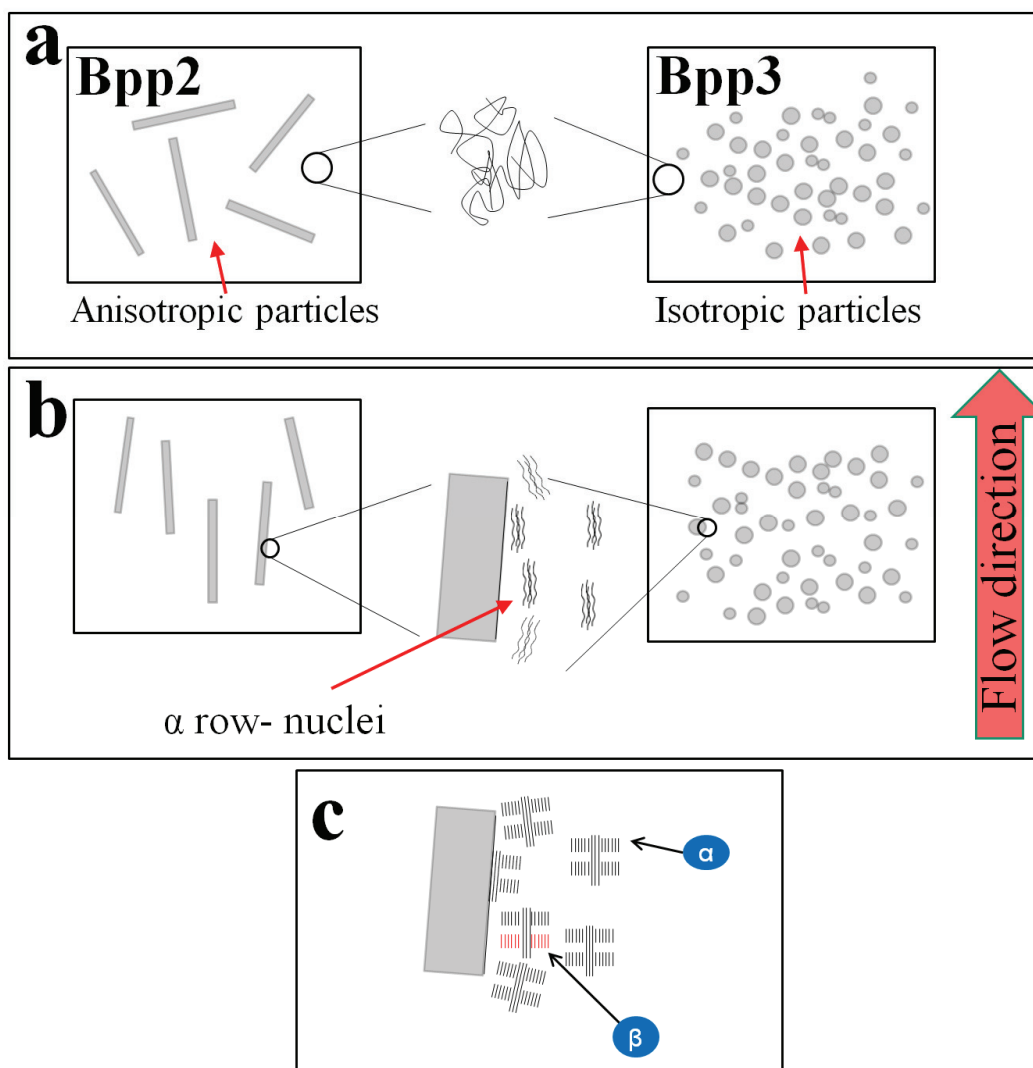


Fig. 28 Crystallization process for iPP with  $\beta$ -nucleating particles under shear. (a) before application of shear, both the  $\beta$ -nucleating agent particles and molecular chains were randomly distributed; (b) after applying shear, a lot of oriented  $\alpha$ -row nuclei were formed near but not necessary on the surface of oriented anisotropic particles and unoriented isotropic particles; (c) The nuclei mainly grow into  $\alpha$ -crystals, however, little  $\beta$ -crystals may also be formed by the  $\alpha$  to  $\beta$  growth transition

## 6.2.2 Influence of shear rate on the crystallization

### 6.2.2.1 Overall crystallization kinetics

The variation of the shear rate usually changes the alignment of molecular chains in the polymer melt and thus influences the subsequent kinetic and thermodynamic behaviours as well as development of crystalline morphology. Fig. 29 illustrates the development of overall crystallinity of Bpp2 sample during shear induced crystallization at shear rates ranging from 2 to 50  $\text{s}^{-1}$ , and the corresponding



crystallization kinetics parameters are listed in Tab. 4. As can be seen, generally the overall crystallization rate increased with increasing shear rate from 2 to 50  $\text{s}^{-1}$ . In addition, it can be found that the higher the shear rate was imposed, the lower the value of overall Avrami exponent became. This indicated that the dimensionality of crystal growth geometry basically decreased with increasing shear rate.

However, compared to quiescent crystallization, the overall crystallization rate decreased after applying step shear of 2 and 10  $\text{s}^{-1}$ . This indicated that the nucleating ability of NJS decreased under relatively low shear. Actually, as known, both flow and nucleating agent can accelerate the crystallization process. However, from our results, it seemed that shear flow may also reduce the crystallization rate under certain conditions. To elucidate this phenomenon, individual crystallinity as a function of time needs to be further studied.

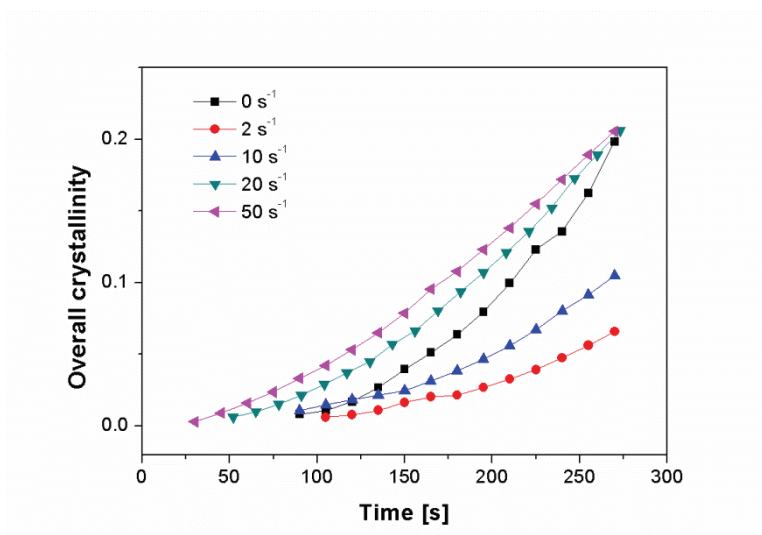


Fig. 29 The overall crystallinity of Bpp2 as a function of time during shear-induced crystallization with different shear rates from 0 to 50  $\text{s}^{-1}$  at 138 °C



Tab. 4 Kinetics parameters for Bpp2 during isothermal shear-induced crystallization with shear rates ranging from 0 to 50 s<sup>-1</sup>

Shear rate (s <sup>-1</sup> )	n			G x 10 <sup>4</sup> (s <sup>-1</sup> )		
	Overall	$\alpha$	$\beta$	Overall	$\alpha$	$\beta$
0	2.9	2.2	3.8	7.4	4.0	3.4
2	2.8	2.5	3.5	2.4	1.6	0.8
10	2.5	2.3	4.1	3.9	3.5	0.4
20	2.1	2.1	2.2	7.6	6.3	1.2
50	1.7	1.7	2.0	7.6	7.0	0.6

#### 6.2.2.2 Crystallization kinetics of $\alpha$ -crystals

Fig. 30 shows the evolution of  $\alpha$ -crystallinity with time. The corresponding kinetics parameters are listed in Tab. 4. As can be seen, the crystallization rate of  $\alpha$ -crystals, similar to the overall crystallization rate, increased with increasing shear rate from 2 to 50 s<sup>-1</sup>. It was surprising that the  $\alpha$ -crystallization rate was even lower than that under quiescent condition when the shear rate was low ( $\leq 10$  s<sup>-1</sup>). Previous results have revealed that the shear always accelerated the crystallization of  $\alpha$ -crystals, since the shear may align the molecular chains along the shear direction and promote the formation of  $\alpha$ -nuclei. The decline of  $\alpha$ -crystallization rate should be attributed to the reduction of nucleation ability of NJS under shear. The presence of nucleating agent provided additional surface, which had good epitaxial match with the lattice of the crystalline polymer and thus facilitated the nucleation process. The application of shear may change the conformation of molecular chains adsorbed at the nucleating agent surface and as a consequence, change the interfacial free energy and nucleating rate of nucleating agent as well.

The Avrami exponent of quiescent crystallization with a value of 2.2 indicated a quasi 2-D crystal growth geometry, which was consistent with Varga et al. [118], who reported that the  $\alpha$ -crystals mainly crystallized on the lateral surface of needle-like NJS. With increasing shear rate (from 2 to 50 s<sup>-1</sup>), the value of Avrami exponent gradually decreased from 2.5 to 1.7, indicating that the growth geometry of  $\alpha$ -crystals changed from mixed 2-D and 3-D to mixed 1-D and 2-D.

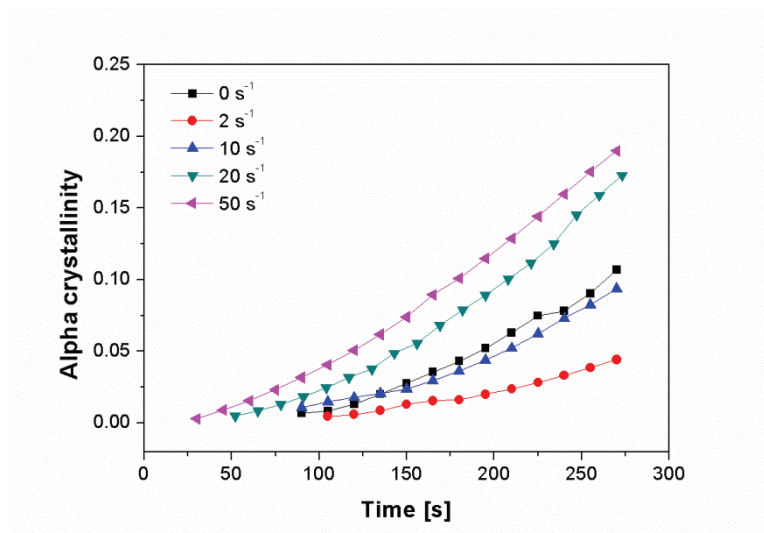


Fig. 30 The  $\alpha$ -crystallinity of Bpp2 as a function of time during shear-induced crystallization with different shear rates from 0 to 50  $\text{s}^{-1}$  at 138 °C

### 6.2.2.3 Crystallization kinetics of $\beta$ -crystals

The development of  $\beta$ -crystallinity for Bpp2 under various shear conditions is illustrated in Fig. 31. The corresponding kinetics data are also listed in Tab. 4. It can be seen that after the application of shear, the  $\beta$ -crystallization rate was strongly decreased compared to that under quiescent condition in all cases, indicating that the development of  $\beta$ -crystals was restrained during shear induced crystallization. The reason can be mainly attributed to the reduction of  $\beta$ -nucleating ability of NJS under shear. In addition, with increasing shear rate, more and more oriented  $\alpha$ -nuclei may be generated which surrounded the NJS particles and thus further inhibited the formation of  $\beta$ -crystals on the surface of NJS particles. The highest crystallization rate of  $\beta$ -crystals during the shear induced crystallization was under a shear rate of 20  $\text{s}^{-1}$ . This result is consistent with Huo et al. [17], who reported that the shear rate of 20  $\text{s}^{-1}$  may induce the highest  $\beta$ -content under low  $\beta$ -nucleating concentrations (less than 0.05 wt %).

From Tab. 4 it can be found that even under shear rate of 10  $\text{s}^{-1}$ , the value of the  $\beta$ -Avrami exponent remained high ( $n = 4.1$ ) and was close to that under quiescent condition ( $n = 3.8$ ), indicating that the  $\beta$ -crystals were mainly induced by  $\beta$ -nucleating agent when the shear rate was lower than 10  $\text{s}^{-1}$ . When the shear rate further increased (20 and 50  $\text{s}^{-1}$ ), the value of  $\beta$ -Avrami exponent decreased to around 2.0, indicating that the growth geometry of  $\beta$ -crystals was gradually changing from spherulitic to disklike and the  $\beta$ -crystals were mainly induced by the oriented  $\alpha$ -row-nuclei.

In Tab. 5 crystallization states at 80 °C for Bpp2 after application of various shears are listed. It can be seen that the  $\beta$ -contents of sample underwent low intensity of shear (shear rate = 2  $\text{s}^{-1}$ ) was similar to that under static crystallization, indicating that at the low shear rate,  $\beta$ -nucleating effectivity retained

during cooling, although the  $\beta$ -development was suppressed during the given isothermal crystallization process. In addition, it is seen that the higher the shear rate was, the lower the  $\beta$ -content became.

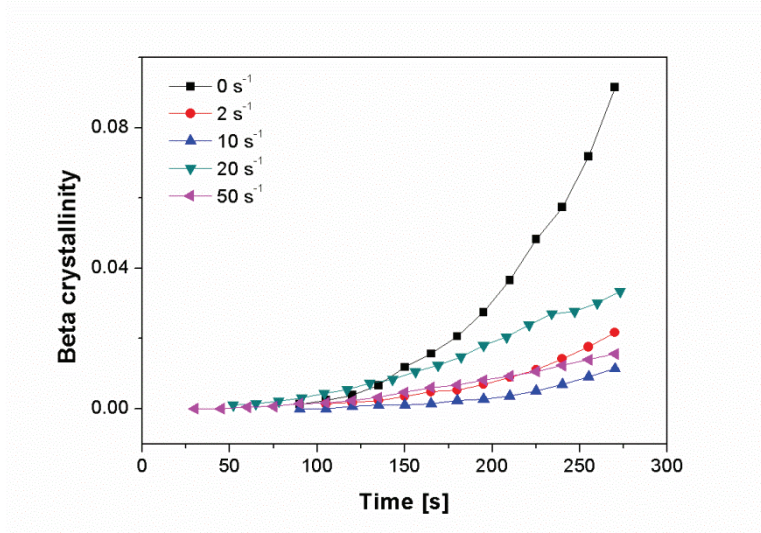


Fig. 31 The  $\beta$ -crystallinity of Bpp2 as a function of time during shear-induced crystallization with different shear rates from 0 to 50 s<sup>-1</sup> at 138 °C

Tab. 5 Crystallization states at 80 °C for Bpp2 after various shear steps. Firstly, the samples were isothermally crystallized at 138 °C for 280 s and then cooled to 80°C, at which the crystallization was basically complete.

Shear rate	Overall crystallinity	$\alpha$ -crystallinity	$\beta$ -crystallinity	$K_{\beta}$ value
0	0.55	0.20	0.35	0.63
2	0.54	0.17	0.36	0.68
10	0.52	0.32	0.20	0.38
20	0.57	0.40	0.17	0.30
50	0.53	0.44	0.094	0.18

#### 6.2.2.4 Evolution of long period under various shear conditions

Fig. 32 shows the development of long period for Bpp2 under various shear conditions. The long period reflects the average distance between the adjacent lamellae.  $\alpha$ - and  $\beta$ -crystalline lamellae coexisted in those  $\beta$ -nucleated iPP with the  $\beta$ -lamellar distance being larger than  $\alpha$ -one [12, 19]. It can be seen from Fig. 32 that under low shear rate of  $2\text{ s}^{-1}$ , the long period was comparable to that of the unsheared sample. As the shear rate increased, the long period tended to increase slightly. Indeed, after application of shear the  $\beta$ -content generally reduced compared with that under static condition (Fig. 33). The increase of long period should not be attributed to the variation of  $\beta$ -phase and should be mainly associated with the shear effect. The higher the shear rate, the higher the orientation of molecular chains and the induced row-nuclei. The lamellar distance may probably increase with increasing orientation degree of row-nuclei. Similar results have been reported by Zhao et al. [14], who have found that the long period and lamellae thickness of poly (ether ether ketone) increased with increasing shear rate under isothermal crystallization. They pointed out that the high shear rate was beneficial for the formation of thick and stable lamellae.

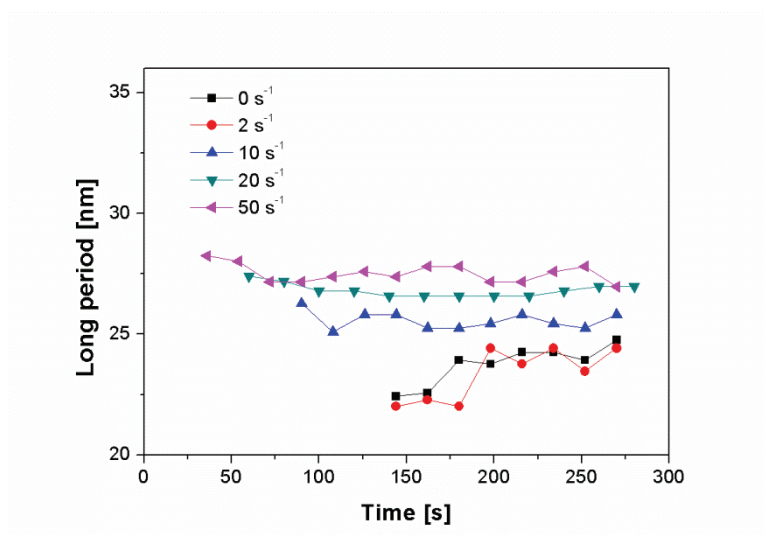


Fig. 32 The development of long period for Bpp2 as a function of time during shear-induced crystallization with different shear rates from 0 to  $50\text{ s}^{-1}$  at  $138\text{ }^{\circ}\text{C}$

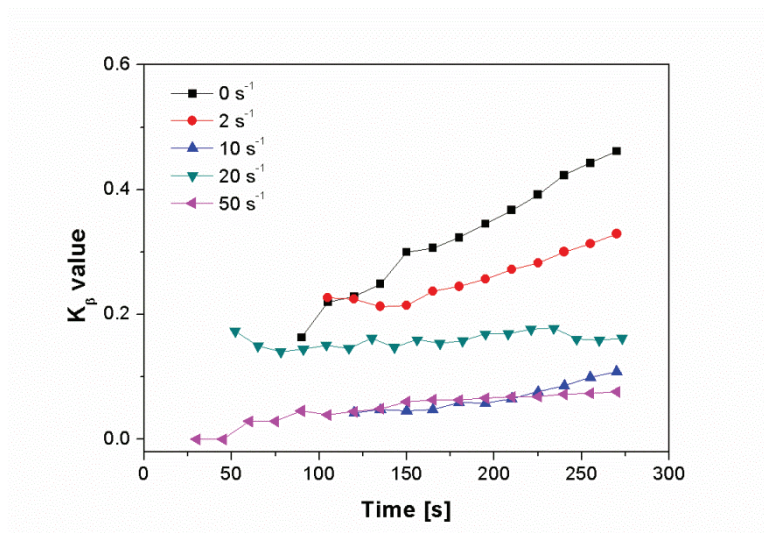


Fig. 33 The  $K_{\beta}$  value of Bpp2 as a function of time during shear-induced crystallization with different shear rates from 0 to 50  $\text{s}^{-1}$  at 138 °C

## 6.2.3 Influence of the temperature on the shear induced crystallization

### 6.2.3.1 Overall crystallization kinetics

The crystallization temperature plays a crucial role in the crystallization process of polymers. Fig. 34 shows the development of overall crystallinity of Bpp2 under various temperatures after step shear with shear rate of 50  $\text{s}^{-1}$ . The corresponding kinetics parameters are summarized in Tab. 6. No crystallization was detected by WAXS during the isothermal crystallization at 150 °C, and obviously, the crystallization rate increased with decreasing temperature. In addition, the value of Avrami exponent decreased with decreasing temperature, indicating that the dimensionality of crystal growth geometry basically decreases with decreasing temperature. It was expected that with decreasing temperature the reptation time of molecular chains increased leading to the increase of the crystal orientation which resulted in the decrease of crystal dimensionality.

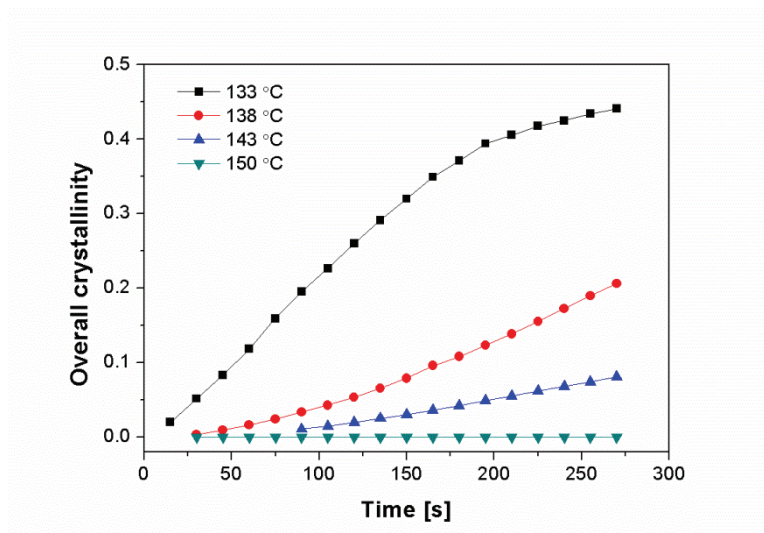


Fig. 34 The overall crystallinity of Bpp2 as a function of time during shear-induced crystallization under different temperatures ranging from 133 to 150 °C, shear rate = 50 s<sup>-1</sup>

Tab. 6 Kinetics parameters for Bpp2 during isothermal sheared-induced crystallization with shear rate of 50 s<sup>-1</sup> at different temperatures

Temperature (°C)	n			G x 10 <sup>4</sup> (s <sup>-1</sup> )		
	Overall	α	β	Overall	α	β
133	1.3	1.2	1.7	16	13	2.9
138	1.7	1.7	2.0	7.6	7.0	0.6
143	1.8	1.8	-	3	3	0
150	-	-	-	0	0	0

### 6.2.3.2 The development of β-crystals

Fig. 35, Fig. 36 and Fig. 37 respectively show the corresponding development of  $K_\beta$  value,  $\alpha$ - and  $\beta$ -crystallinity for Bpp2 under various temperatures after shearing the sample for 5 s with a shear rate of 50 s<sup>-1</sup>. It can be seen that at 143 °C no  $\beta$ -crystals were formed during the given isothermal crystallization. Absence of  $\beta$ -crystals can be mainly attributed to the relatively high crystallization temperature of 143 °C which was above the critical  $\beta$  to  $\alpha$  transition temperature of 141 °C [15] and

thus suppressed the formation of  $\beta$ -crystals. With decreasing temperature, the  $K_\beta$  value tended to increase indicating that the lower temperature was in favour of formation of  $\beta$ -crystals. However, the content of  $\beta$ -crystals was minor, not only during the given isothermal crystallization, but also in final solid state (Tab. 7). The  $\alpha$ -crystals formed at 143 °C were highly oriented, which was proved by the 2D-WAXS pattern at the end of given isothermal crystallization at 143 °C (Fig. 38 a), and were mainly induced by shear and the interaction between melt and nucleating agent under shear flow. After application of shear, a certain amount of oriented  $\alpha$ -nuclei formed around the NJS particles. The resulting  $\alpha$ -crystals grew and formed possibly an encapsulated network surrounding the  $\beta$ -nucleating agent thus inhibited the formation of  $\beta$ -crystals during the subsequent cooling. As a consequence, very small amount of  $\beta$ -crystals existed in the solid state (Tab. 7). The corresponding 2D-WAXS pattern is shown in Fig. 38 b. It is seen that the (3 0 0) reflection is arc-like and positioned at the equator (also see the azimuthal plot in Fig. 38 d) indicating that the formation of the  $\beta$ -crystals was mainly attributed to the  $\alpha$  to  $\beta$  growth transition occurred on the surface of shear induced  $\alpha$ -nuclei. In addition, in Tab. 7 it can be noticed that the  $K_\beta$  value for Bpp2, after isothermal crystallization at 150 °C, was larger than that at 143 °C. This is possibly associated with the faster relaxation of oriented molecular chains under higher temperature. The corresponding 2D-WAXS pattern at the solid state is shown in Fig. 38 c. It can be seen that there are 6 peaks on the (3 0 0) reflection (Fig. 38 e) indicating that certain  $\beta$ -crystals directly grew on the surface of NJS particles, which oriented preferentially in the shear direction. Although  $\beta$ -nucleating ability of NJS retained to a certain extent, the application of shear still strongly restricted the formation of  $\beta$ -crystals during the subsequent cooling process.

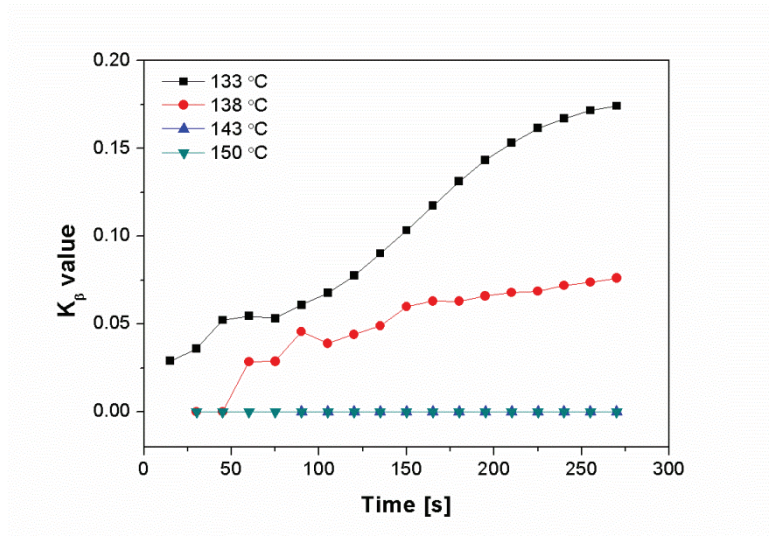


Fig. 35 The  $K_\beta$  value of Bpp2 as a function of time during shear-induced crystallization under different temperatures ranging from 133 to 150 °C, shear time = 5 s, shear rate = 50  $s^{-1}$



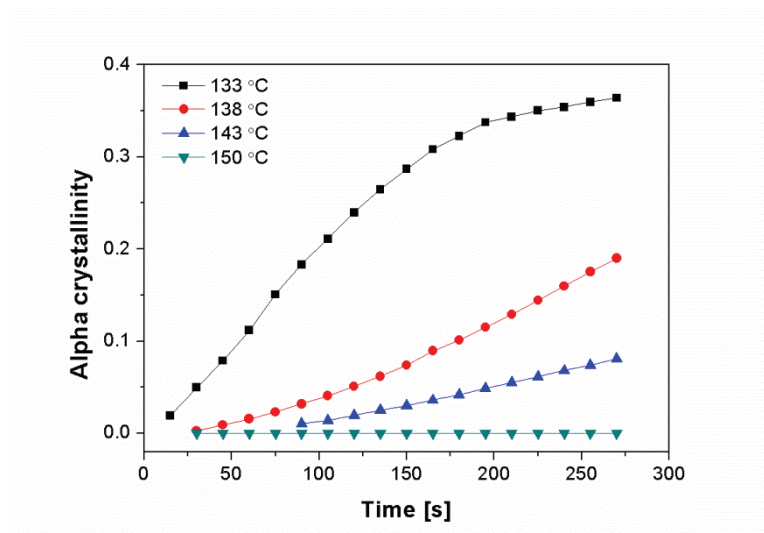


Fig. 36 The  $\alpha$ -crystallinity of Bpp2 as a function of time during shear-induced crystallization under different temperatures ranging from 133 to 150 °C, shear time = 5 s, shear rate =  $50 \text{ s}^{-1}$

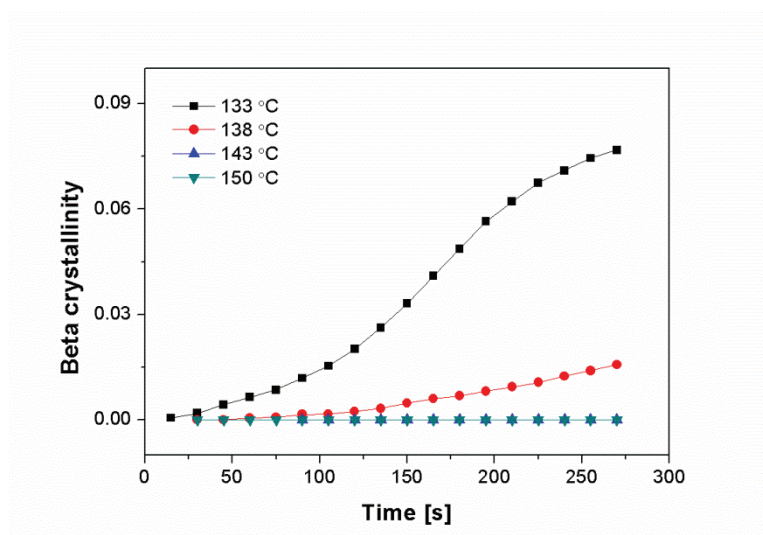


Fig. 37 The  $\beta$ -crystallinity of Bpp2 as a function of time during shear-induced crystallization under different temperatures ranging from 133 to 150 °C, shear time = 5 s, shear rate =  $50 \text{ s}^{-1}$



Tab. 7 Crystallization states at 80 °C for Bpp2 after shearing the sample for 5 s with a shear rate of 50 s<sup>-1</sup> at various temperatures. Firstly, the samples were isothermally crystallized at a given temperature for 280 s and then cooled to 80 °C, where the crystallization was basically complete.

Crystallisation temperature	Crystallinity	$\alpha$ -crystallinity	$\beta$ -crystallinity	$K_\beta$ value
133	0.51	0.42	0.092	0.18
138	0.53	0.44	0.094	0.18
143	0.52	0.49	0.025	0.048
150	0.47	0.40	0.063	0.14

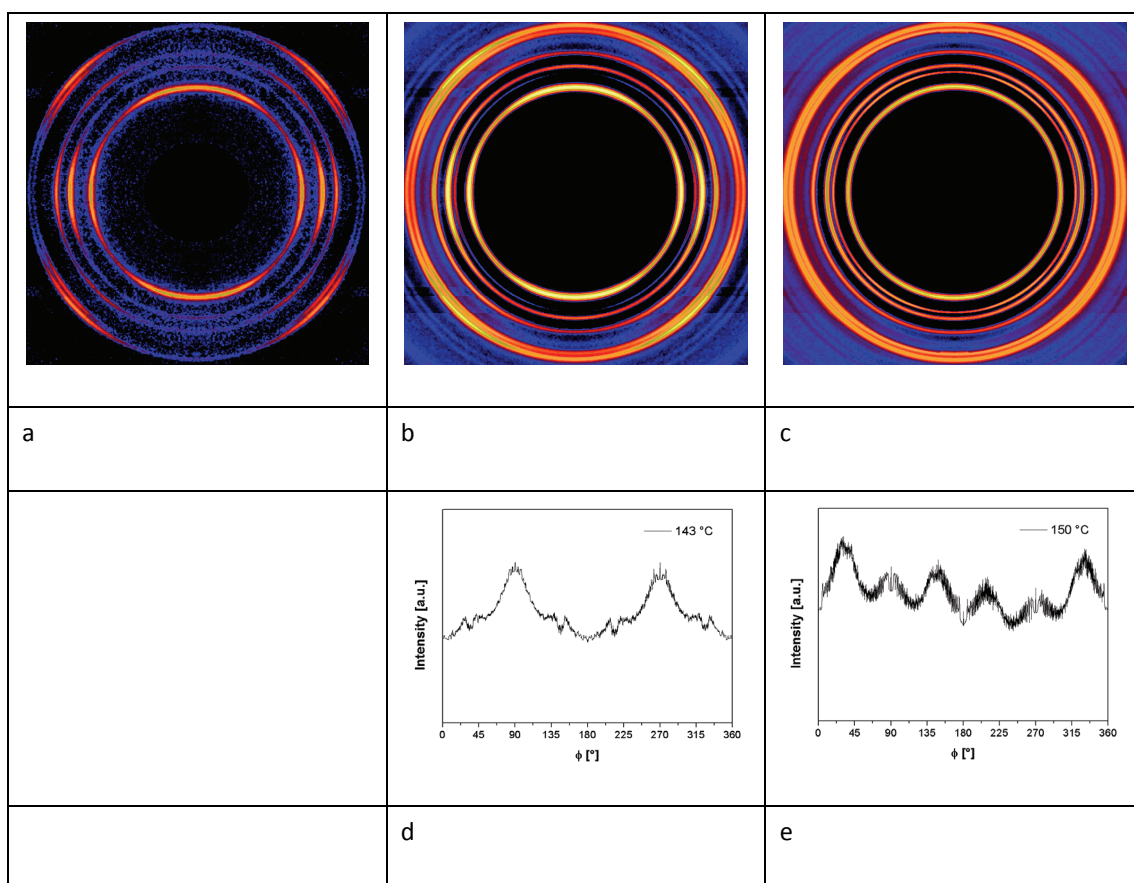


Fig. 38 Selected 2D-WAXS patterns for sheared Bpp2. For enhancing the scattering contrast a modification was applied here, i.e., by subtraction of the original pattern with the pattern just

prior to the application of shear. (a) at the end of given isothermal crystallization at 143 °C; (b) at the solid state after isothermal crystallization at 143 °C; (c) at the solid state after isothermal crystallization at 150 °C; (d) azimuthal plot of (3 0 0) reflection for 2D-WAXS pattern in (b); (e) azimuthal plot of (3 0 0) reflection for 2D-WAXS pattern in (c)

### 6.2.3.3 The evolution of long period

Fig. 39 shows the development of long period for Bpp2 during shear induced crystallization under various temperatures. It can be seen that the long period at 143 °C was higher than that at other two temperatures. It was expected that the long period increased with increasing temperature, since more stable (thicker) crystalline lamellae tended to be formed at higher crystallization temperature [141]. The long period at 138 °C was more or less stable with value of about 27.5 nm during the given isothermal crystallization process. On the other hand, the long period at 133 °C firstly decreased from 30 nm to about 26 nm and then gradually increased to about 29 nm, higher than that at 138 °C. It is well known that the long period tended to decrease during the isothermal crystallization which was explained by formation of secondary lamellae on the primary lamellar stacks or insertion of new formed lamellar stacks into the existing lamellar structure [9, 42]. The reason for the current unusual remarkable increase of long period remains unclear; however, it is probably associated with the increase of  $\beta$ -content during the crystallization at 133 °C (Fig. 35).

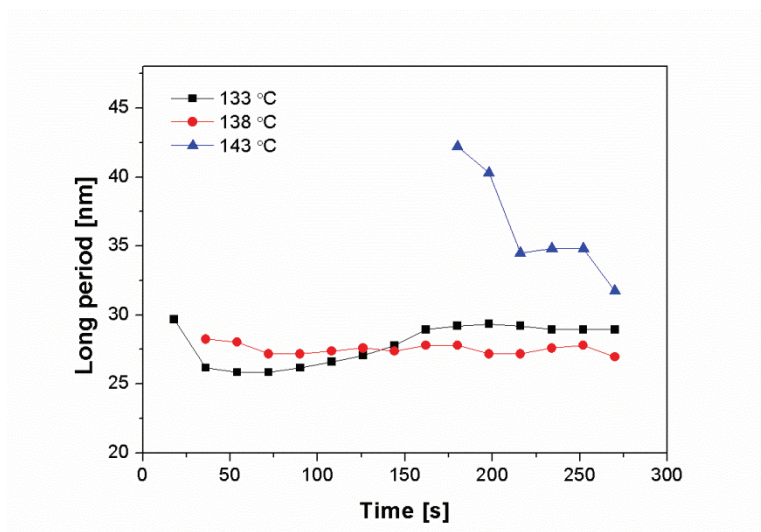


Fig. 39 The development of long period for Bpp2 as a function of time during shear-induced crystallization under different temperatures ranging from 133 to 143 °C, shear time = 5 s, shear rate = 50 s<sup>-1</sup>

## 6.3 Extension induced crystallization of $\beta$ -nucleated iPP

Shear flow was usually considered as ‘weak’ flow, which cannot effectively stretch the molecular chains. It has been demonstrated that the extensional flow (or elongation flow) was much more

effective for orienting the polymer chains and accelerating the crystallization than shear flow [142]. Inspired from the fiber spinning process, in which extensional flow is dominant, a novel melt draw experiment was designed which should be able to realize a high extension of molecular chains. By combination with synchrotron X-ray scattering the development of the specific structure of the  $\beta$ -nucleated iPP during extension induced crystallization process is possible to be investigated in-situ, which should be beneficial for the better understanding and ultimately controlling the formation process of crystal morphology in polymer processing.

### 6.3.1 Morphology of NJS particles in the quiescent iPP melt

The  $\beta$ -nucleating agent used in this study can be partially or completely dissolved in the iPP melt depending on the final temperature of heating. The morphology of investigated NJS in the quiescent iPP melt is shown in Fig. 40, which was taken immediately after the temperature reaching drawing temperature of 138 °C during cooling. It can be seen that some NJS recrystallized and formed needle like crystals with length around 15  $\mu\text{m}$  and diameter around 2  $\mu\text{m}$  in the melt.

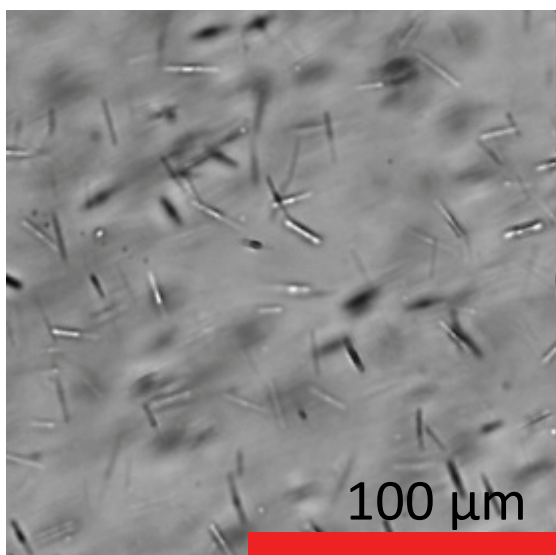


Fig. 40 Needle-like  $\beta$ -nucleating agent crystals in iPP melt (0.03 wt %) at 138 °C

### 6.3.2 WAXS

Fig. 41 shows the selected WAXS patterns of Bpp2, after drawing to 700 %. Different to pure iPP (Fig. 42), it can be seen that during crystallization, 6 well-defined spots appeared at the (3 0 0) diffracting plane of  $\beta$ -crystals, including 2 additional symmetrically-equivalent (120) and (210) planes [21]. Such pattern indicated that the chain axis (c-axis) of  $\beta$ -crystals was oriented perpendicular to the drawing direction [21, 138]. The  $\beta$ -nucleating agent used in this study existed in needle-like crystals in iPP melt. During drawing, the needle-like  $\beta$ -nucleating agent aligned along the extensional direction due to the

hydrodynamic force. Then the  $\beta$ -crystals grew epitaxially on the lateral planes of the oriented needle-like  $\beta$ -nucleating agent with their c-axis perpendicular to the long axis of the latter. The epitaxially grown lamellae were thus perpendicular to the extensional direction and they exhibited cuboid-shape, which was also found by Zhou [143] in an AFM study. Fig. 43 shows the corresponding evolution of overall crystallization with time, it can be seen that the crystallization kinetics of Bpp2 is significantly faster than that of pure iPP indicating that the addition of the  $\beta$ -nucleating agent strongly accelerate the crystallization process.

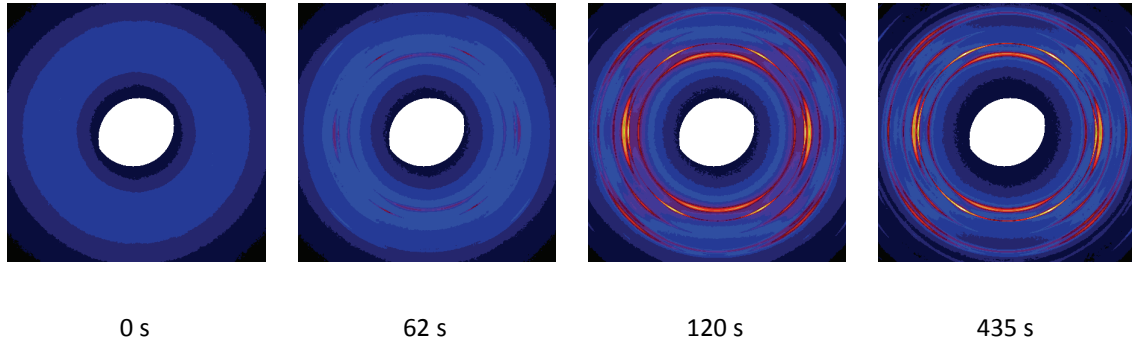


Fig. 41 Selected WAXS patterns of Bpp2 after drawing at 138 °C. Drawing direction is vertical

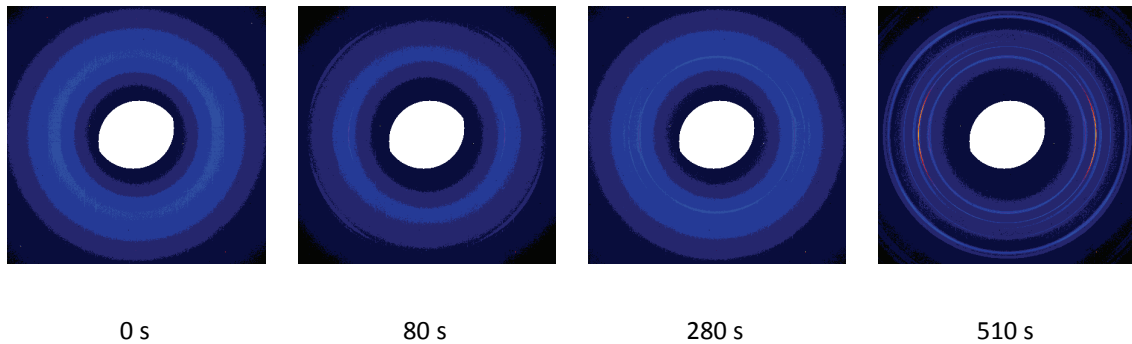


Fig. 42 Selected WAXS patterns of iPP after drawing at 138 °C. Drawing direction is vertical

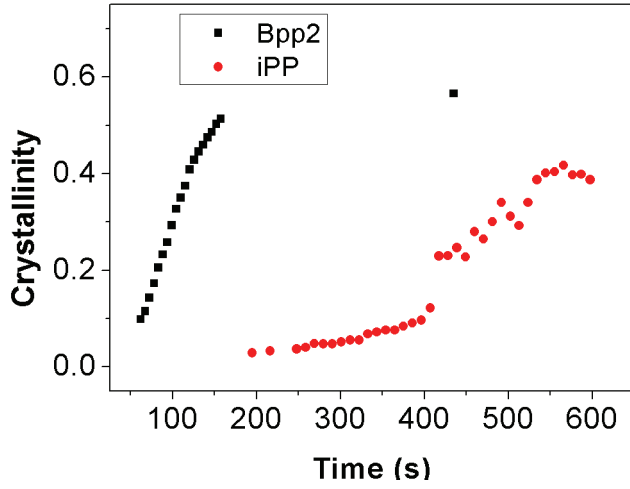


Fig. 43 Overall crystallinity over time for Bpp2 and iPP after drawing at 138 °C

### 6.3.3 SAXS

Fig. 44 presents the selected SAXS patterns of Bpp2, treated in the same way as above. Directly after drawing (8 s), a streak appeared at the equator, which may be related to the emergence of fibrillar nuclei, bundles of extended molecular chains (shish), aligned along the extensional direction. Ruland streak method [144] was used to analyze the equatorial streak in SAXS pattern. This method was originally designed for analyzing the longitudinal voids in polymer and carbon fibers, however, it was successfully applied in the estimation of the size and misorientation of shish structure in polymer melt [75, 129, 132, 140]. In this method, a series of azimuthal scans were performed from center out along the equator and modelled by Gaussian or Lorentz function. The integral width ( $B_{obs}$ ) (peak area / peak height) of each azimuthal profile is a function of the length  $\langle L_{scatter} \rangle$  and the misorientation width ( $B_{\phi}$ ) of the scatter. If a Gaussian function is suitable to fit the azimuthal distributions, it follows:

$$B_{obs}^2 = \frac{4\pi^2}{\langle L_{scatter} \rangle^2 q^2} + B_{\phi}^2 \quad (21)$$

If a Lorentz function is adequate to describe the azimuthal distributions, then the relation becomes:

$$B_{obs} = \frac{2\pi}{\langle L_{scatter} \rangle q} + B_{\phi} \quad (22)$$

In this study, all the azimuthal distributions can be fitted with Lorentz functions well.  $\langle L_{scatter} \rangle$ , i.e., the length of shish, in Bpp2 at 8 s obtained from Eq. (22) was roughly about 90 nm. In contrast to the nucleated iPP, no equatorial streak was observed in the pure iPP (Fig. 45). However, this does not mean that the extended chain crystals did not exist in the pure iPP melt. Maybe it was due to the lower density of extended chain crystals and they were farther apart, thus they cannot be observed by

the SAXS [140]. The shish generated in the Bpp2 was mainly associated with the interaction between needle-like  $\beta$ -nucleating agent particle and the polymer chains under extensional flow and was reasonably assumed to be formed primarily in the vicinity of the oriented  $\beta$ -nucleating agent due to the enhanced velocity gradient around the particles.

Then at 32 s (Fig. 44), while the equatorial streaks remained almost unchanged, two additional scattering peaks appeared in stretching direction, implying that some lamellar assemblies with relatively large lateral dimensions were formed perpendicular to the drawing direction. Such lamellar assemblies should grow epitaxially on the fibrillar nuclei and form subsequently stacks of lamellae (kebabs) which were usually observed during extension induced crystallization of iPP.

From 32 to 205 s, the scattering intensity increased with crystallization and the scattering primarily concentrated on both meridian and equator indicating the presence of well-oriented lamellar structure. The increase in scattering intensity of the meridional peak should be related to the formation and development of kebabs as well as cuboid-like  $\beta$ -lamellae aligned perpendicular to the extensional direction as discussed above. The evolution of equatorial streaks may possibly be associated with the development of cuboid-like  $\beta$ -lamellae, the growth of shish [131] and formation of branched lamellae (daughter lamellae) grew epitaxially on the kebabs (parent lamellae) [145]. From WAXS pattern (Fig. 41) it can be inferred that the angle between c-axis of parent and daughter lamellae was about  $80^\circ/100^\circ$ . If daughter lamellae are dominant in the equatorial scattering, four lobes can be seen  $10^\circ$  deviated from the equator in SAXS pattern [146]. But from SAXS patterns shown in Fig. 44, it can be seen that the scattering concentrated at equator, which indicated that the equator scattering was mainly resulted from the shish or  $\beta$ -lamellae. At 205 s, a distinct four-spot pattern can be seen. During cooling to room temperature, such pattern remained nearly unchanged. On the other hand, during whole crystallization process, only two-spot pattern was observed in pure iPP (Fig. 45). This indicated that the  $\beta$ -nucleating agent played an essential role in the formation of such four-spot pattern.

Fig. 46 shows the changes of long period  $L_B$  for pure iPP (only meridian) and Bpp2 (both meridian and equator) with time. It can be seen that for Bpp2 the long period at the equator was around 30 nm. Considering the size of shish kebab, the average distance between shishes should be far beyond the long period value. Thus, the scattering in equator should be mainly attributed to the cuboid-like  $\beta$ -lamellae aligned perpendicular to the extensional direction. The long period in equator direction decreased from 32 nm to 28 nm during crystallization, indicating the formation of secondary lamellae on the primary lamellar stacks or insertion of new formed lamellar stacks into the existing lamellar structure [9, 42].

Fig. 47 shows the evolution of integrated intensities of meridian and equator for Bpp2 after drawing at 138 °C using the following expressions:

$$I_{equator} = \int_{0.084}^{1.43} \int_0^{30} I(q, \varphi) d\varphi dq \quad (23)$$

and

$$I_{meridian} = \int_{0.084}^{1.43} \int_{30}^{90} I(q, \varphi) d\varphi dq \quad (24)$$

It can be seen that the intensities of both meridian and equator increased rapidly at the initial stage in this  $\beta$ -nucleated iPP. In the meridional direction, from about 110 s, it met a plateau, while in the equatorial direction the intensities increased further until about 150 s. To elucidate this phenomenon, individual crystallinity as a function of time was analyzed as shown in Fig. 48. It can be seen that from about 110 s, the growth of  $\alpha$  crystals met a plateau, while  $\beta$ -crystals grew further. Thus, the consistence of both WAXS and SAXS results further demonstrated that the equatorial scattering was mainly attributed to the  $\beta$ -lamellae.

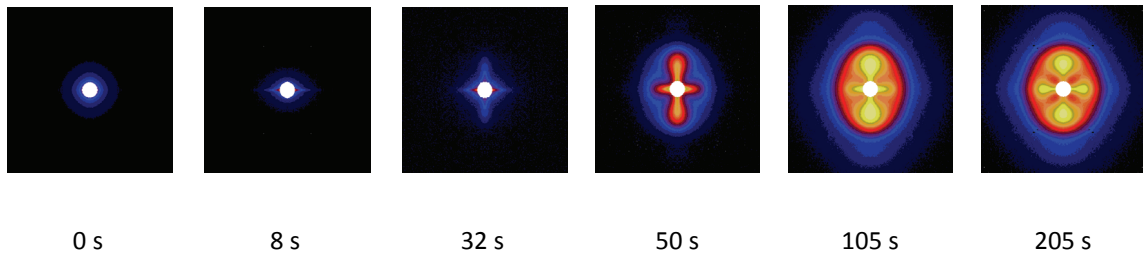


Fig. 44 Selected SAXS pattern of Bpp2 after drawing. Drawing direction is vertical

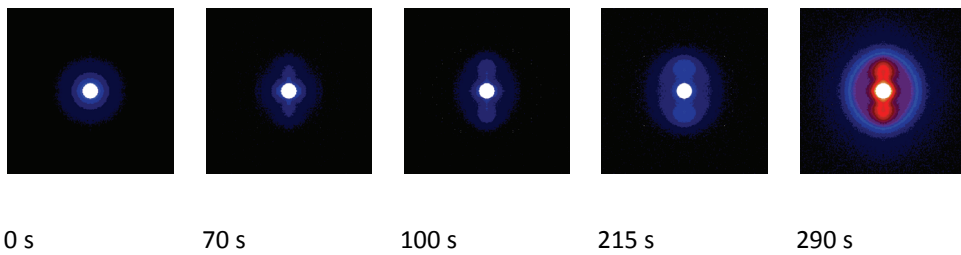


Fig. 45 Selected SAXS pattern of pure iPP after drawing. Drawing direction is vertical

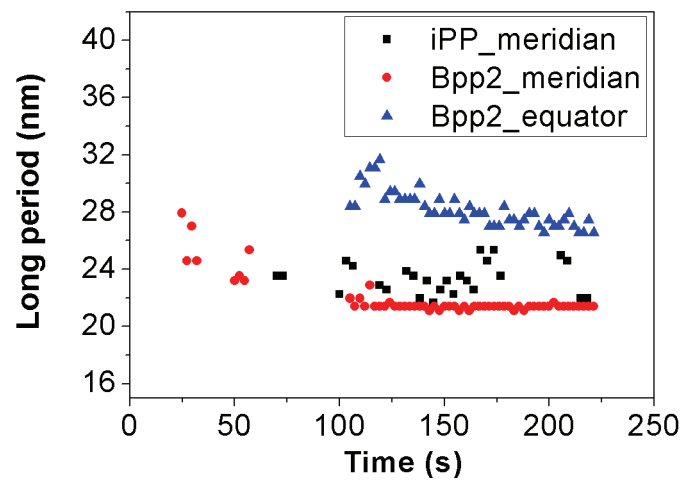


Fig. 46 Changes of long period with time

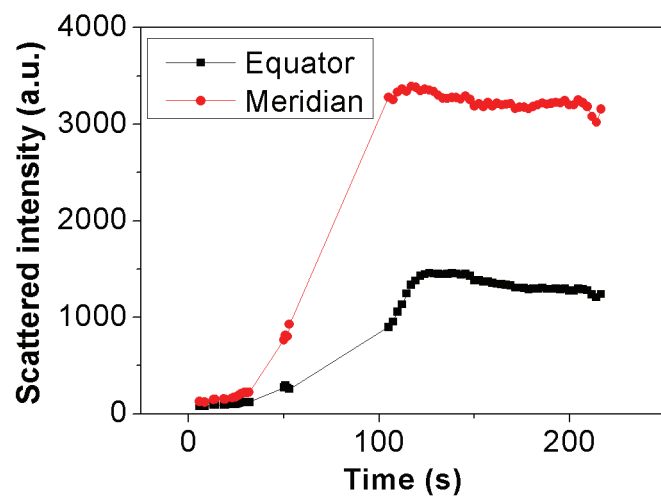


Fig. 47 Changes of integrated scattered intensity in equatorial and meridional direction for Bpp2



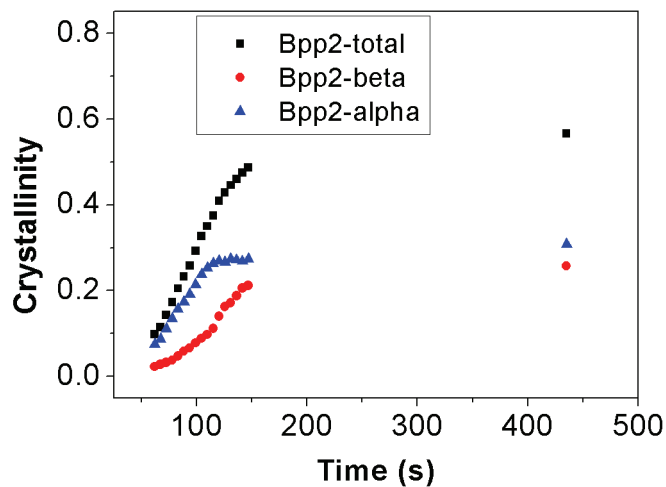


Fig. 48 Overall and individual crystallinity over time for Bpp2 after drawing at 138 °C

## 6.4 Morphological distributions of injection-moulded $\beta$ -iPP investigated by microbeam

In above sections 6.2 and 6.3 we discussed the flow induced crystallization mainly at isothermal temperature and relatively moderate flow fields. However, in the common polymer processing, such as injection moulding, extrusion etc., the molten polymers are often exposed to much more complicated flow fields and temperature gradients. As an example of injection moulding, 3 distinct layers exist in the iPP sheet, i.e., a highly oriented nonspherulitic skin, a shear-nucleated intermediate layer, and a core layer (Fig. 49) [46, 147]. The very thin skin layer is mainly composed of amorphous phase due to the rapid cooling, while the core layer consists predominantly of spherulitic structure due to the low cooling and shear-strain rates which allow a good relaxation of molecular chains. The shear zone or shear layer, which undergoes extremely high shear rates, separates the skin and core layer and it is the most important layer determining the shear-induced properties. The deformation behaviour of semi-crystalline polymers is strongly dependent on the morphology formed during processing. To better understand the deformation mechanism of  $\beta$ -nucleated iPP prepared by common injection moulding, it is necessary to understand the morphological distributions in different layers, including crystallinity, fractions of different types of crystals, the size of crystals and the orientation functions. Such a study will also be useful for controlling the surface properties such as hardness, adhesion, wear resistance, impact resistance, permeability and reflectivity [145, 148, 149].

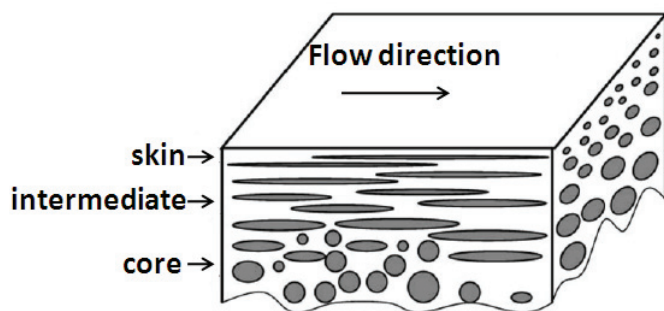


Fig. 49 Schematic illustration of the skin-core morphology of injection-moulded sample [147]

Conventional X-ray scattering cannot be used to investigate the morphological distribution across the thickness direction since its beam size is so big that both the shear layer and core layer are simultaneously illuminated. Thanks to the microbeam with beam size of 20 X 20  $\mu\text{m}$  at MINAXS beamline, Petra III in Hamburg, the beam can be precisely positioned to characterize the crystalline structures in different layers.

#### 6.4.1 Influence of concentration of $\beta$ -nucleating agent

The overall crystallinity, orientation degree as well as the different crystalline phases across the sample cross section for the iPP samples at position 1 nucleated with various concentrations of nucleating agent are shown in Fig. 50.

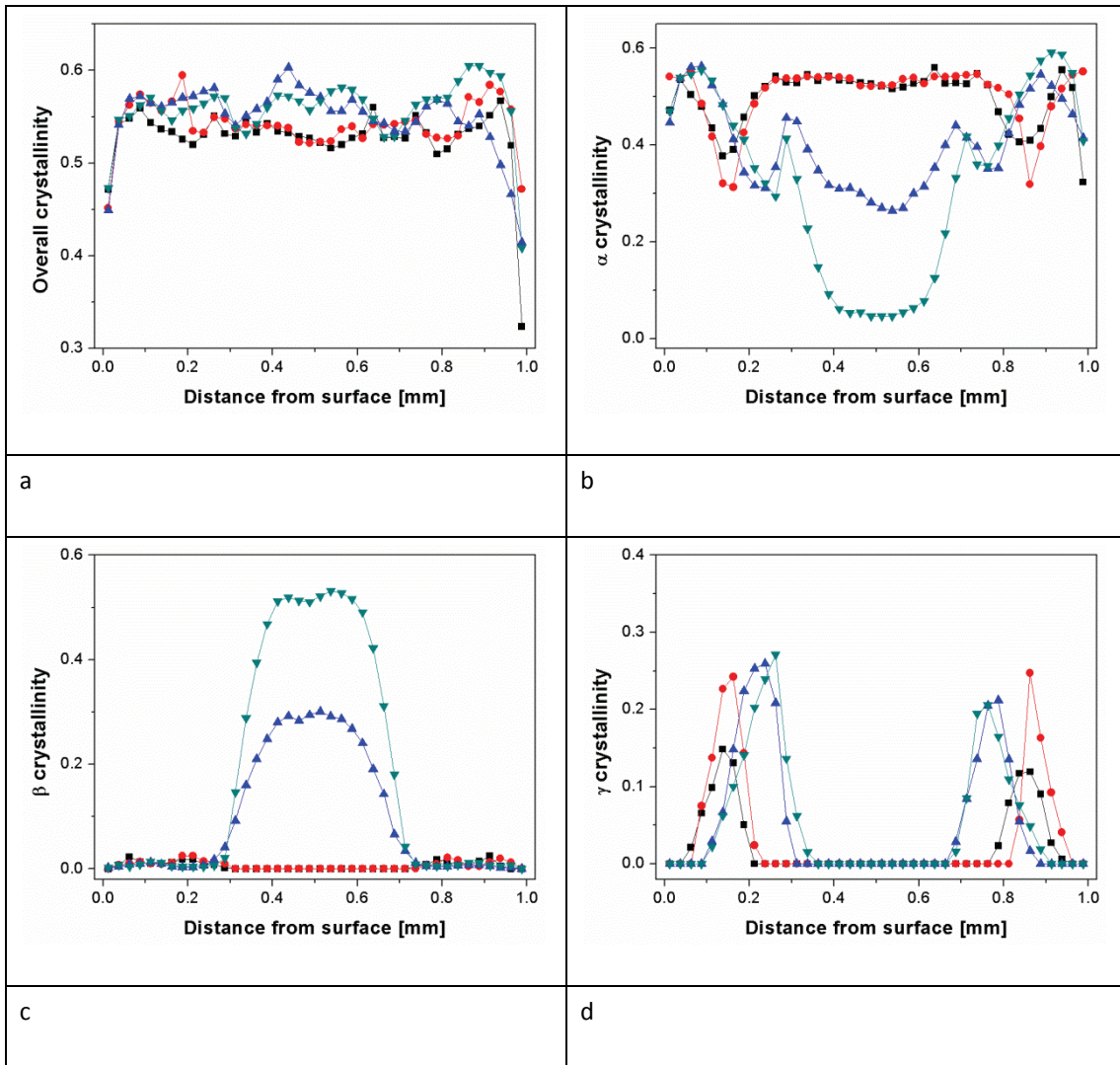
##### 6.4.1.1 Distributions of crystallinity

Fig. 50 a shows the overall crystallinity distribution, it can be seen that all of the samples exhibited low crystallinity at the surface area, which was attributed to the quick cooling rate. The value of overall crystallinity fluctuated a little bit apart from the surface, however, remained relatively constant. The corresponding individual  $\alpha$ -,  $\beta$ -, and  $\gamma$ -crystallinity distributions are presented in Fig. 50 b-d. Comparing these results, one may observe the following:

1. At low concentrations of  $\beta$ -nucleating agent (pure iPP and Bpp1), the core was solely composed of  $\alpha$ -crystals. The absence of  $\beta$ -crystals in core layer of Bpp1 indicated that the few amount of  $\beta$ -nucleating agent did not induce the formation of  $\beta$ -crystals. This was possible since crystallization of the fine dissolved  $\beta$ -nucleating agent in the iPP melt may be strongly delayed during the quick cooling process. With increasing NJS concentration, the  $\beta$ -crystallinity increased at the expense of  $\alpha$ -phase in the core layer (Bpp2 and Bpp3 in Fig. 50 b and c). The  $\beta$ -crystallinity gradually increased from around 0.3 mm apart from the surface and reached maximum at the centre indicating that the molecular chains changed to coiled state from 0.3 mm due to the lower shear and cooling rates allowing a good relaxation of molecular chains.

2. The  $\beta$ -crystallinity at the skin and in the shear layer was very low, even in Bpp3 with highest  $\beta$ -nucleating agent concentration (Fig. 50 c). This was reasonable since the shear rate at these two layers was extremely high which induced large amount of oriented  $\alpha$ -crystals and thus inhibited the formation of  $\beta$ -crystals.

3. The very high shear effect at the shear layer also led to formation of  $\gamma$ -crystals (Fig. 50 d). Compared with pure iPP, the addition of  $\beta$ -nucleating agent resulted in a higher content of  $\gamma$ -form crystals in the shear layer of the injection-moulded samples and made the  $\gamma$ -crystallites locate at the position farther to the surface. It seemed that the presence of  $\gamma$ -phase may be an indicator for the position of shear layer [114].



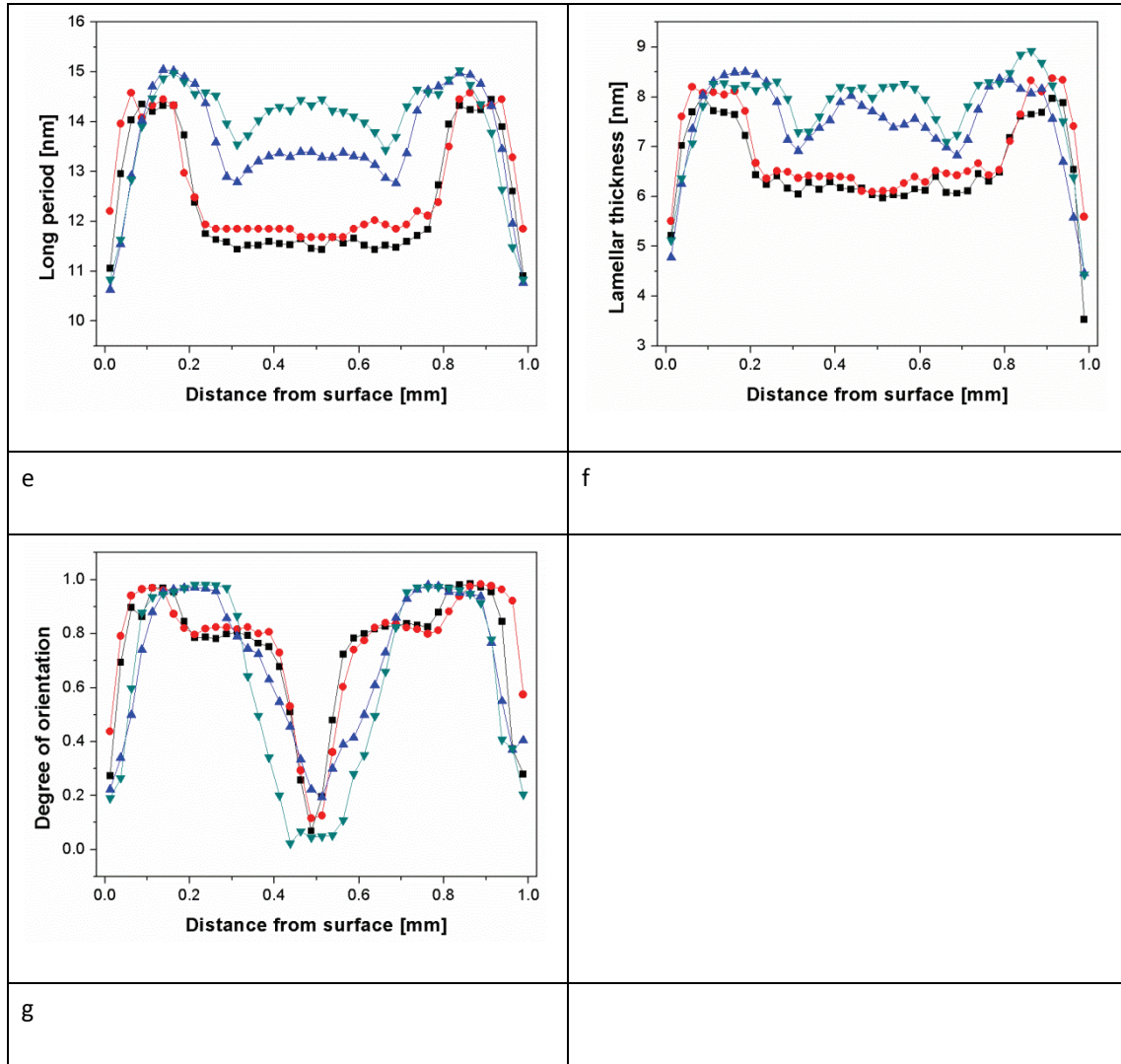


Fig. 50 Distributions of overall crystallinity (a),  $\alpha$ -crystallinity (b),  $\beta$ -crystallinity (c),  $\gamma$ -crystallinity (d), long period (e), lamellar thickness (f) and orientation degree (g) for iPP samples at position 1 within an injection-moulded iPP plate with different amount of nucleating agent: Pure iPP (■), Bpp1 (●), Bpp2 (▲) and Bpp3 (▼)

#### 6.4.1.2 Distributions of long period and lamellar thickness

The long period and lamellar thickness distributions are shown in Fig. 50 e and f, respectively. As can be seen all samples exhibited a low value of both long period and lamellar thickness at the surface, where less crystallites were formed due to fast cooling rate. The long period and lamellar thickness gradually increased to a maximum in the shear region and then decreased in the transition area between shear region and core region. The long period and lamellar thickness of Bpp2 and Bpp3 were larger than that of pure iPP and Bpp1 in the shear region, indicating that the presence of nucleating agent particles promoted the alignment of molecular chains and induced more oriented nuclei. Thus overall crystallization occurred at higher temperature leading to the formation of thicker lamellae in the shear layer. The long period increased with increasing concentration of  $\beta$ -nucleating agent at the

core layer. This was reasonable since the  $\beta$ -nucleating agent may promote the formation of  $\beta$ -crystals at high crystallization temperature leading to increase the lamellar stacking distance. The lamellar thickness shared the similar tendency with the long period at the core layer indicating that the addition of  $\beta$ -nucleating agent was beneficial for the formation of thick and stable  $\beta$ -crystals. In addition, it can be observed that the distribution of long period and lamellar thickness was relatively flat for iPP without or with little nucleating agent (iPP and Bpp1) at the core region indicating that the molecular chains of  $\alpha$ -crystals shared similar thermomechanical history at this region. On the other hand, for iPP with high concentration of  $\beta$ -nucleating agent, the distributions of long period and lamellar thickness exhibited inverted U-shape at the core region, which can be mainly attributed to the change of  $\beta$ -content as shown in the Fig. 50 c.

#### 6.4.1.3 Distributions of orientation degree

Fig. 50 g shows the distributions of orientation functions for iPP nucleated with various concentrations of  $\beta$ -nucleating agent. In all of the samples, the orientation degree increased, starting at a low value at the surface, where less ordered crystallites were formed due to fast cooling, to a maximum in the shear region, after which it generally decreased to a low value in the core region. Special attention was paid to the shear layer, where the orientation degree was very high (close to 1) for all of the samples. Combining with the Fig. 50 b and c, it can be concluded that in  $\beta$ -nucleated iPP prepared by traditional injection moulding the outer layer (skin + shear layer) was dominated by highly oriented  $\alpha$ -form crystals, while the core layer was rich in  $\beta$ -crystals, when the concentration of beta nucleating agent was larger than 0.03 wt%. In addition, it is clearly noticed that the shoulder at the maximum for Bpp2 and Bpp3 are wider than that for pure iPP and Bpp1, indicating that the presence of  $\beta$ -nucleating particles significantly widened the shear layer.

#### 6.4.2 Influence of thermomechanical history

Two samples were selected to investigate the thermomechanical history on the morphological distributions of  $\beta$ -nucleated iPP: the first one was named Bpp2-in-1 and the second one Bpp2-in-2, both taken from the Bpp2 injection-moulded sheet. The main difference between these two samples was that the former, located near the inlet, underwent relatively high shear rate compared to the latter one, located far from the inlet.

Fig. 51 shows the linear WAXS intensity profiles of Bpp2 at position 1 and 2, both taken at 0.22 mm away from the surface of the injection-moulded plates. It can be seen that there was a distinct  $\gamma$ -(1 1 7) peak in Bpp2-in-1 while no obvious  $\gamma$ -(1 1 7) peak was observed in Bpp2-in-2. A similar situation was observed in other regions of Bpp2-in-2. This indicates that little if any  $\gamma$ -phase was formed in Bpp2-in-2 due to the relatively low shear rate. Due of this, the  $\gamma$ -content in the shear layer was approximately taken as 0.

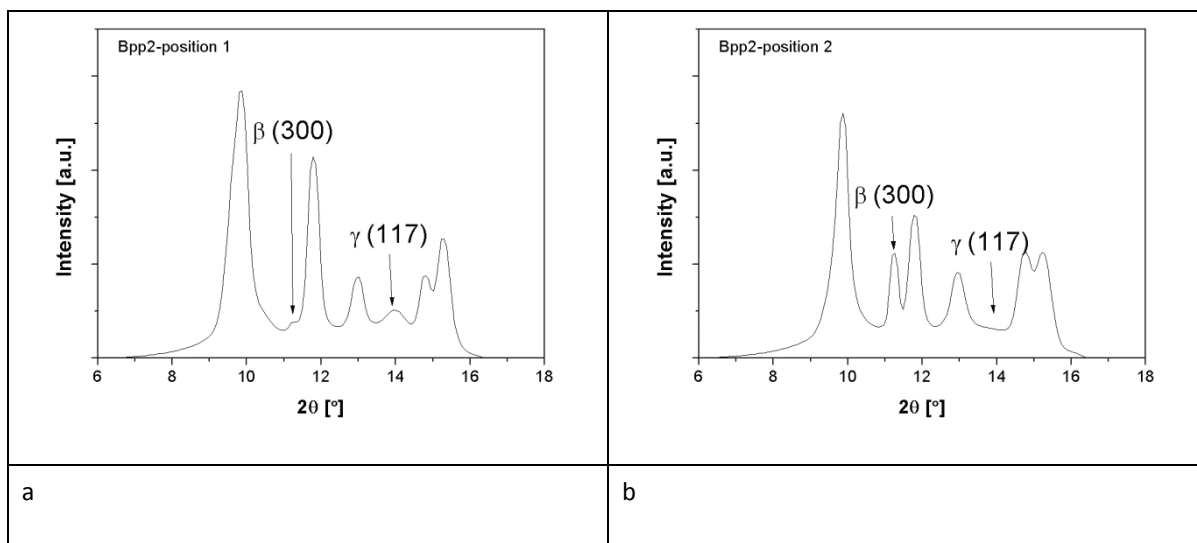


Fig. 51 Linear WAXS intensity profiles of Bpp2 at position 1 (a) and 2 (b), both taken at 0.22 mm away from the surface of the injection-moulded plates

#### 6.4.2.1 Distributions of crystallinity

Fig. 52 shows the morphological distributions of Bpp2-in-1 and Bpp2-in-2. It can be seen from Fig. 52 that the crystallinity of both samples was more or less constant over a broad range, although there was marked shear and temperature gradient across sample cross section. The individual crystallinity distributions are shown in Fig. 52 b-d. By comparing the results one may observe the following:

1. The  $\alpha$ -phase dominated at the surface in both samples.
2. The  $\beta$ -phase in Bpp2-in-1 distributed narrower than that in Bpp2-in-2. This was reasonable since the higher shear rate in the former was beneficial for the formation of highly oriented  $\alpha$ -phase in the shear layer, while the lower shear rate in the latter allowed more molecular chains relax into random coiled state which was beneficial for inducing the formation of  $\beta$ -crystals by  $\beta$ -nucleating agent
3. Compared to Bpp2-in-1, there was no  $\gamma$ -phase in Bpp2-in-2.

#### 6.4.2.2 Distributions of long period and lamellar thickness

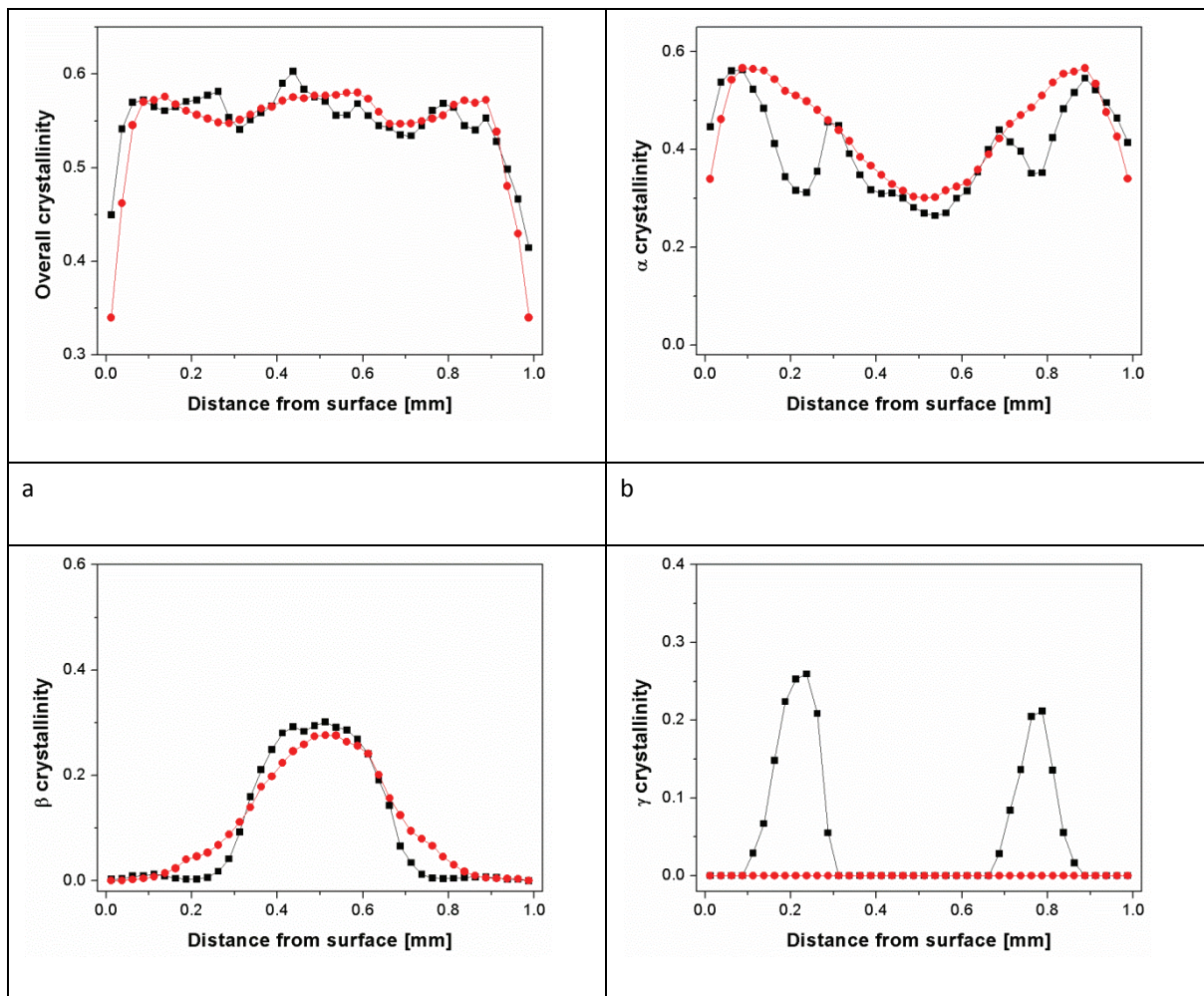
The long period and lamellar distributions for these two samples are shown in Fig. 52 e and f. It was seen that both samples exhibited similar distribution. However, it can be seen that Bpp2-in-1 possessed larger long period and lamellar thickness at the shear layer, indicating that higher shear rate was beneficial for the formation of thicker lamellae. This can be explained as follow: the higher shear rate can more effectively promote the alignment of molecular chains and induce more nuclei and thus increase crystallization temperature leading to formation of thicker lamellae with increased stacking distance. On the other hand, one may observe that the long period and lamellar thickness of Bpp2-in-2 at the core layer were larger than that of Bpp2-in-1. As can be seen in Fig. 52 b-d, the individual



crystallinity distributions for both samples were similar in the core region. The difference of long period and lamellar thickness may be attributed to the different crystallization temperatures, i.e., the crystallization temperature for Bpp2-in-2 was higher than that for Bpp2-in-1. This was possibly explained as follows: due to the higher shear rate, the crystallization rate of Bpp2-in-1 was faster than that of Bpp2-in-2 at the skin and shear region, which may possibly lead to faster cooling rate in the core region.

### 6.4.2.3 Distributions of orientation functions

Fig. 52 g shows the distributions of orientation functions for these two samples. As can be seen, both samples exhibited similar orientation function distributions. However, the orientation degree of Bpp2-in-1 was higher than that of Bpp2-in-2 in shear layer, and the shoulder at the maximum for the former was significantly wider than that for the latter, indicating that higher shear rate was beneficial for the formation of wider shear layer.



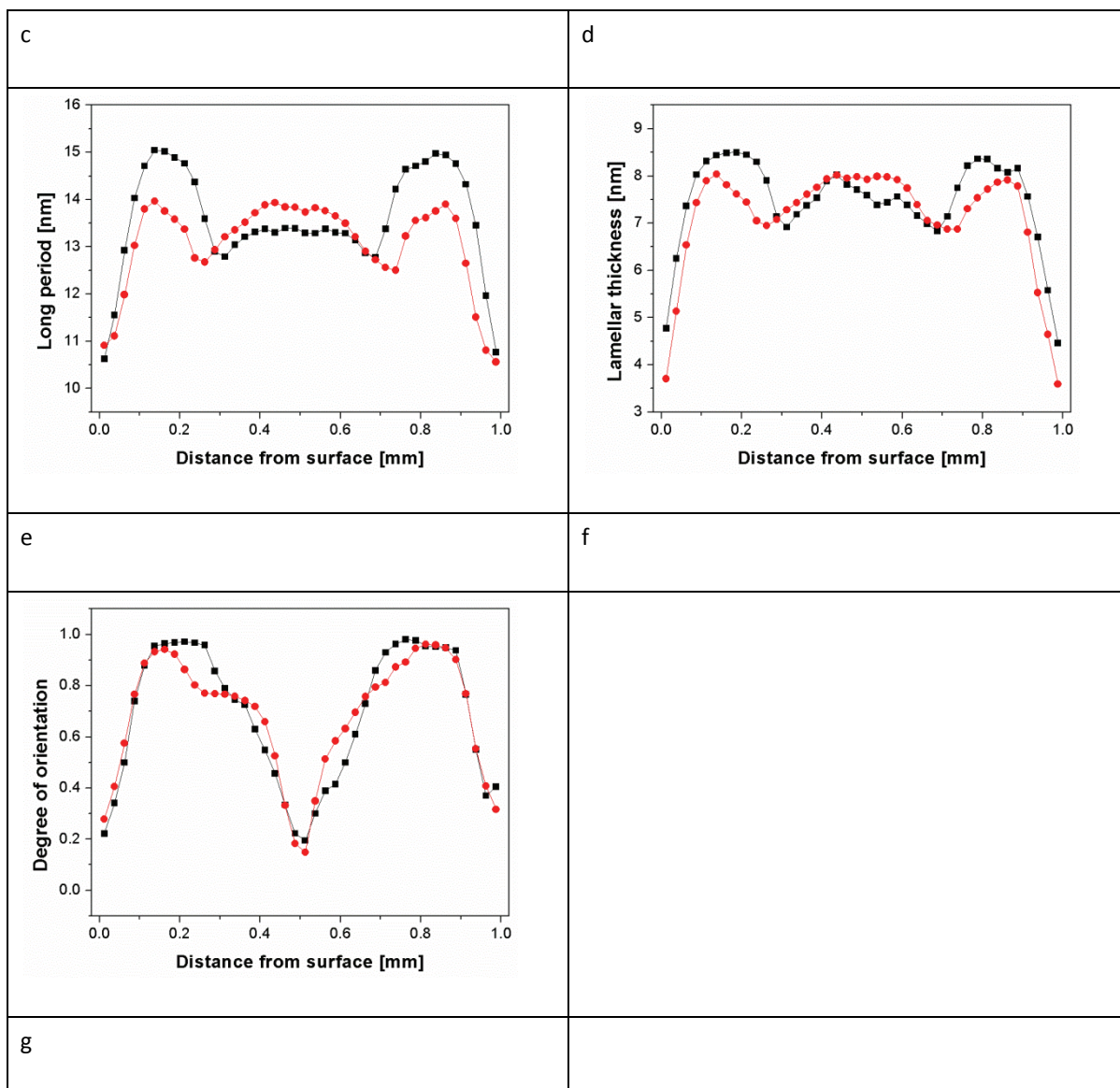


Fig. 52 Distributions of overall crystallinity (a),  $\alpha$ -crystallinity (b),  $\beta$ -crystallinity (c),  $\gamma$ -crystallinity (d), long period (e), lamellar thickness (f) and orientation degree (g) for injection-moulded Bpp2 sample at position 1 (■) and 2 (●)

## 6.5 Structural development of injection-moulded $\beta$ -iPP under deformation

### 6.5.1 Influence of concentration of $\beta$ -nucleating agent-preliminary results

In the last chapter we analysed the morphological distributions for injection-moulded iPP nucleated with various concentrations of  $\beta$ -nucleating agent. In this section, their deformation behaviour will be investigated. Firstly the results for undeformed and deformed (strain = 300%) injection-moulded iPP samples with different concentrations of  $\beta$ -nucleating agent will be discussed. The strain of 300% is



selected, since morphology at this strain may reflect the key features of plastic deformation. The stretching deformation experiments were performed with strain rate of 0.1 mm/s at 90°C.

Fig. 53 and Fig. 54 display the WAXS and SAXS patterns of undeformed injection-moulded iPP samples with different concentrations of  $\beta$ -nucleating agent. As can be seen, all of the samples exhibit a highly oriented structure.

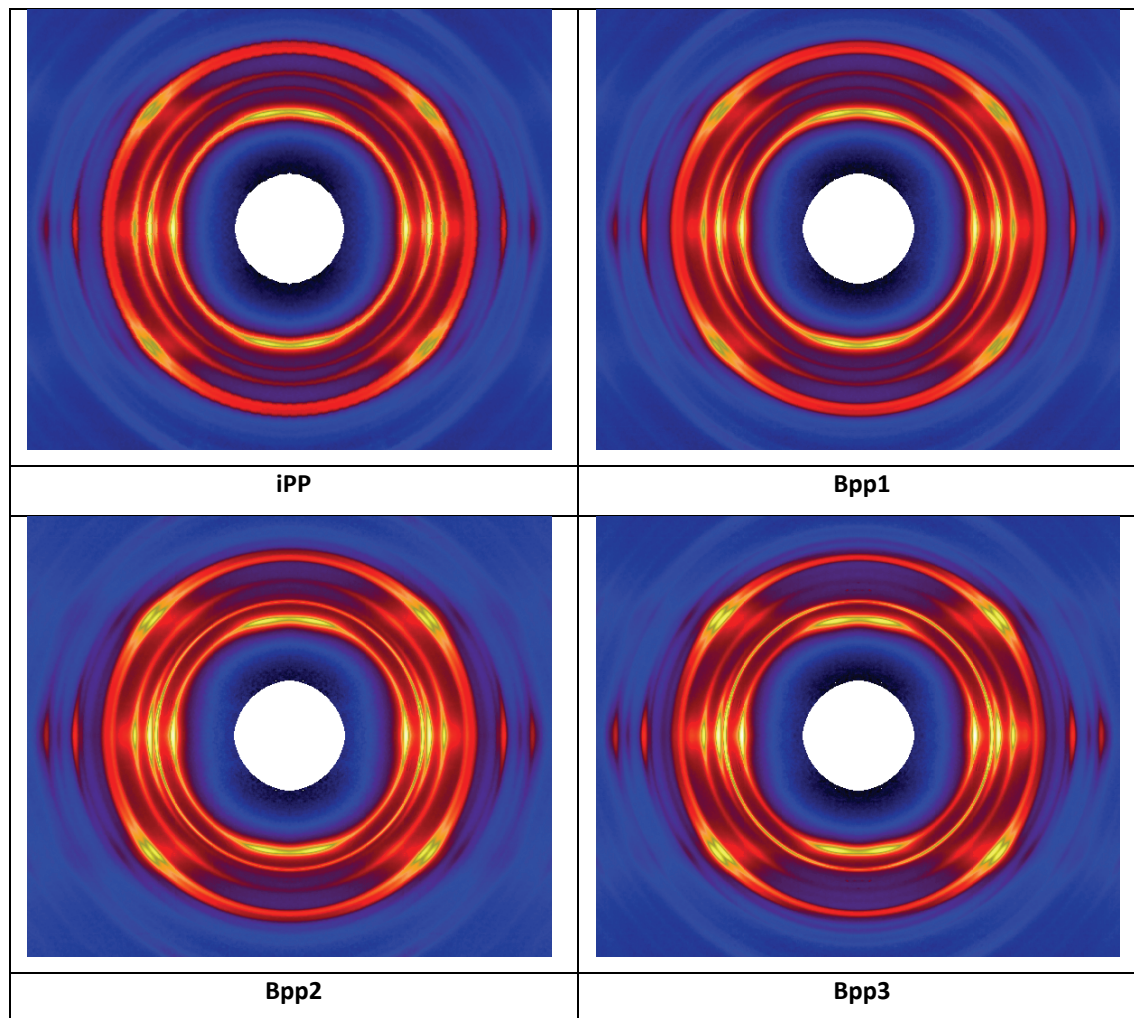


Fig. 53 WAXS patterns of undeformed injection-moulded iPP samples with different concentrations of  $\beta$ -nucleating agent, injection direction is vertical

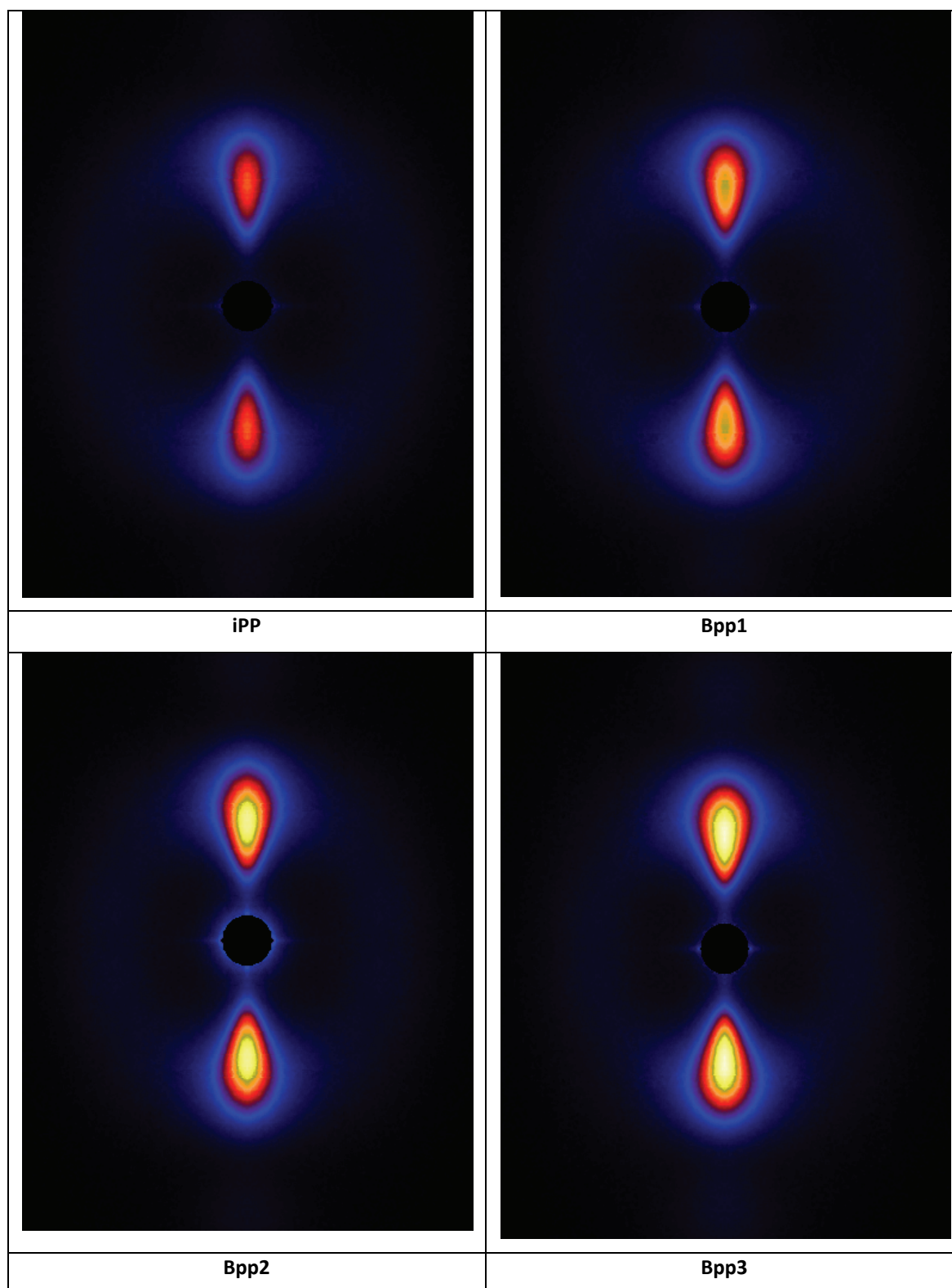


Fig. 54 SAXS patterns for undeformed injection-moulded iPP samples with different concentrations of  $\beta$ -nucleating agent, injection direction is vertical

Fig. 55 shows the integrated intensities in meridional and equatorial direction for the SAXS-patterns shown in Fig. 54 using the following expressions:

$$I_{equator} = \int_{0.084}^{1.43} \int_{-10^{\circ}}^{10^{\circ}} I(q, \varphi) d\varphi dq \quad (25)$$

and

$$I_{meridian} = \int_{0.084}^{1.43} \int_{80^{\circ}}^{100^{\circ}} I(q, \varphi) d\varphi dq \quad (26)$$

The SAXS scattering intensities are related to the electronic density contrast and to the volume fraction of the objects. It can be seen that the intensity at the meridian is much higher than that at equator. The intensity at equator is almost independent of the concentration of  $\beta$ -nucleating agent, while the intensity at meridian increases with increasing concentration of  $\beta$ -nucleating agent indicating that lamellar structure becomes more perfect as the concentration of the nucleating agent increases.

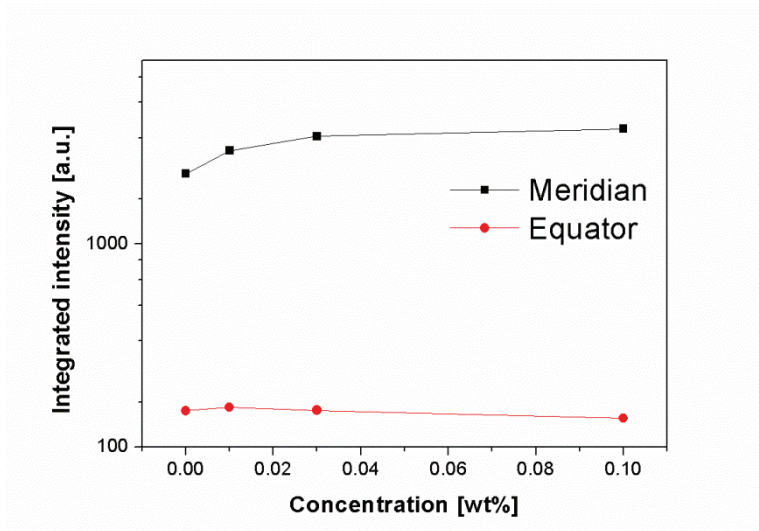


Fig. 55 Integrated intensity along meridian and equator for undeformed injection-moulded iPP as a function of  $\beta$ -nucleating agent concentrations,  $T = 90^{\circ}\text{C}$

Fig. 56 shows the 2D-SAXS patterns of iPP samples nucleated with various concentrations of  $\beta$ -nucleating agent stretched to strain of about 300% at  $90^{\circ}\text{C}$ . It can be observed that with increasing concentration of  $\beta$ -nucleating agent, the scattering intensity tends to increase. This can also be clearly seen in Fig. 57. Combining with the shape of SAXS patterns, it can be inferred that voids and cavities along the stretching direction exist in the deformed iPP samples and their volume increases with increasing concentration of  $\beta$ -nucleating agent. The increased volume of void and cavity is thus

possibly associated with the  $\beta$  to  $\alpha$  phase transition. To elucidate this phenomenon, the SAXS and WAXS data are further analyzed.

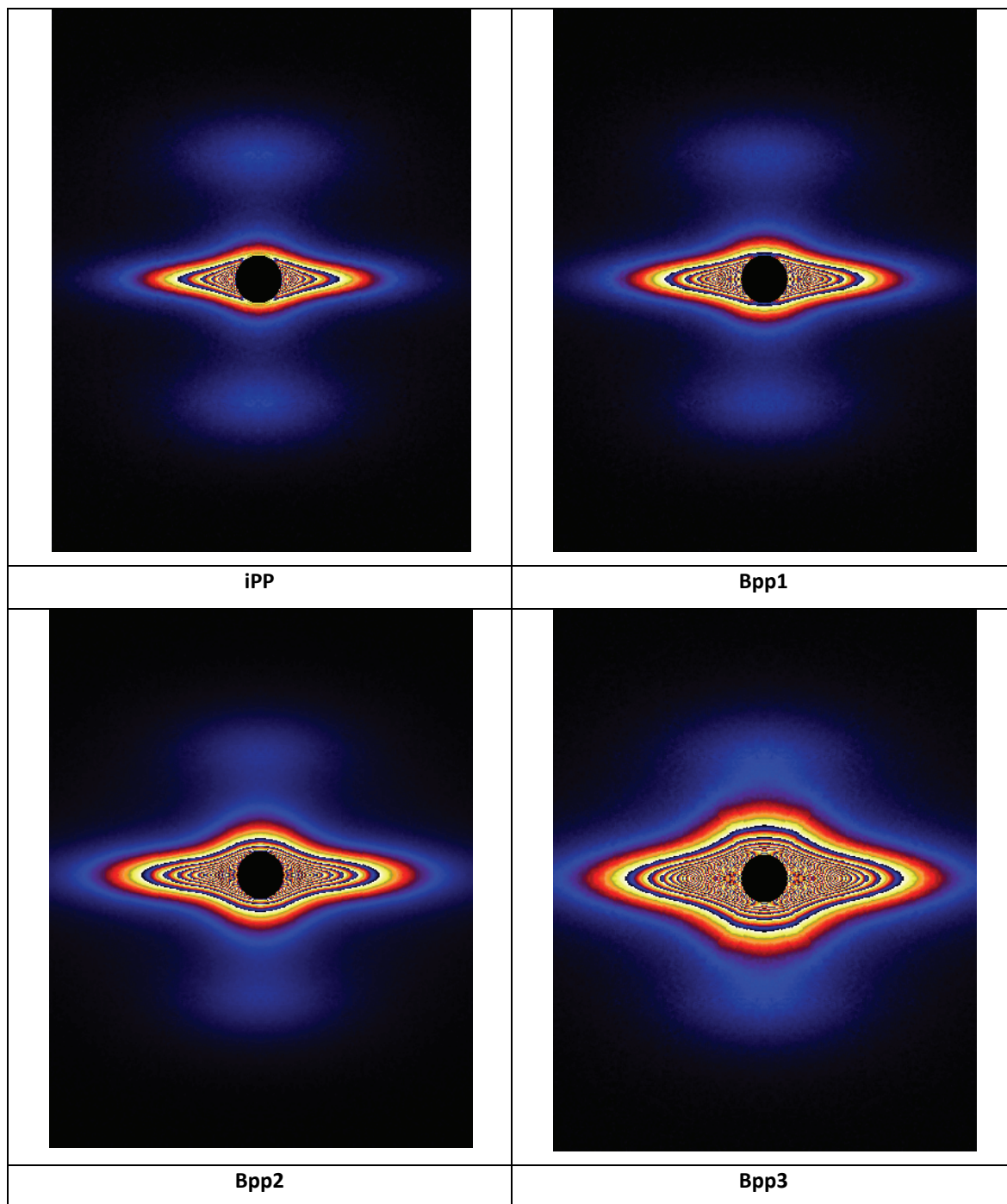


Fig. 56 SAXS patterns of iPP with different amount of  $\beta$ -nucleating agents at strain of 300%. Strain rate 0.1 mm/s.  $T = 90^\circ\text{C}$ , both injection and stretching directions are vertical, linear-scale intensity



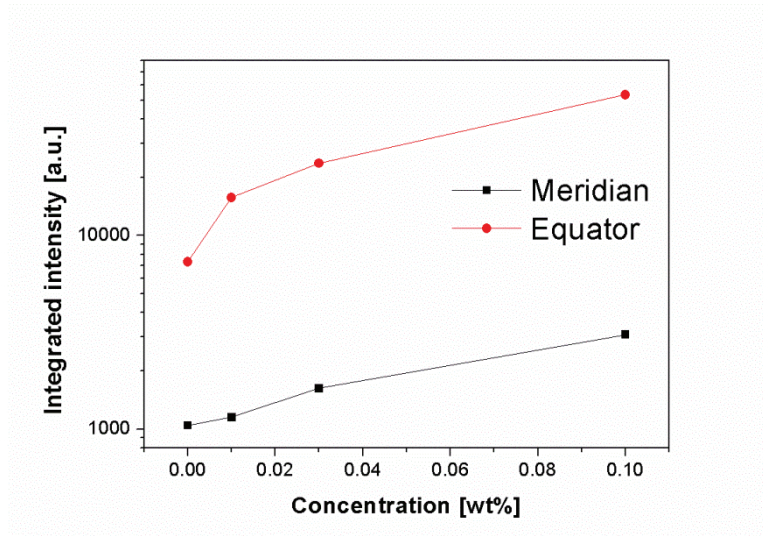


Fig. 57 Integrated intensity along meridian and equator (according to equation 25 and 26 ) for deformed injection-moulded iPP with stretching rate of 0.1 mm/s and strain of 300% as a function of  $\beta$ -nucleating agent concentrations,  $T = 90^\circ\text{C}$

Fig. 58 shows the change of long period of deformed and undeformed injection-moulded samples as a function of  $\beta$ -nucleating agent concentrations. It can be seen that the long period increases with increasing NJS concentration for undeformed samples. As discussed in the last chapter, the increased long period can be mainly attributed to the following two reasons: 1, increased crystallization temperature; 2, increased  $\beta$ -content with relatively thick lamellae thickness compared to  $\alpha$ -lamellae. After stretching to 300%, the long period of  $\beta$ -nucleated iPP samples decreases to a constant value of 13.4 nm. This indicates that the deformation process promotes the fragmentation and rearrangement of crystallites followed the formation of thinner lamellae [94]. In addition, it is expected that the destruction of the thicker lamellae, which are more stable, may need higher stress and thus higher stress concentration was generated around the lamellae leading to formation of more voids and cavities.

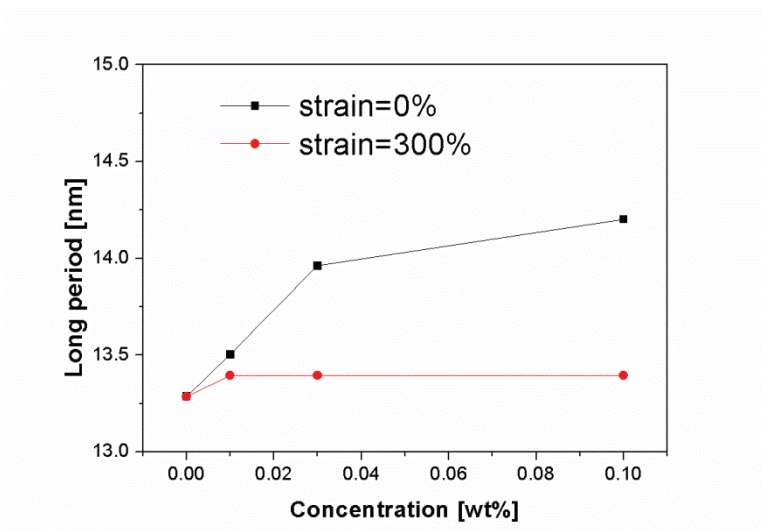


Fig. 58 The change of long period of deformed and undeformed injection-moulded samples as a function of  $\beta$ -nucleating agent concentrations,  $T = 90^\circ\text{C}$ , stretching rate = 0.1 mm/s, taken from meridian

Fig. 59 displays the 2D-WAXS patterns of iPP samples nucleated with various concentrations of  $\beta$ -nucleating agent stretched to strain of about 300%. It is seen that those patterns are more or less identical regardless of the presence of weak  $\beta$ -(3 0 0) reflection in Bpp2 and Bpp3. Fig. 60 shows the corresponding crystallinity of those undeformed and deformed samples. It can be seen that the crystallinity of undeformed samples is more or less similar with values of around 0.53. After stretching to 300%, it decreases to a value of around 0.47 indicating the destruction of crystals occurred during the deformation process.

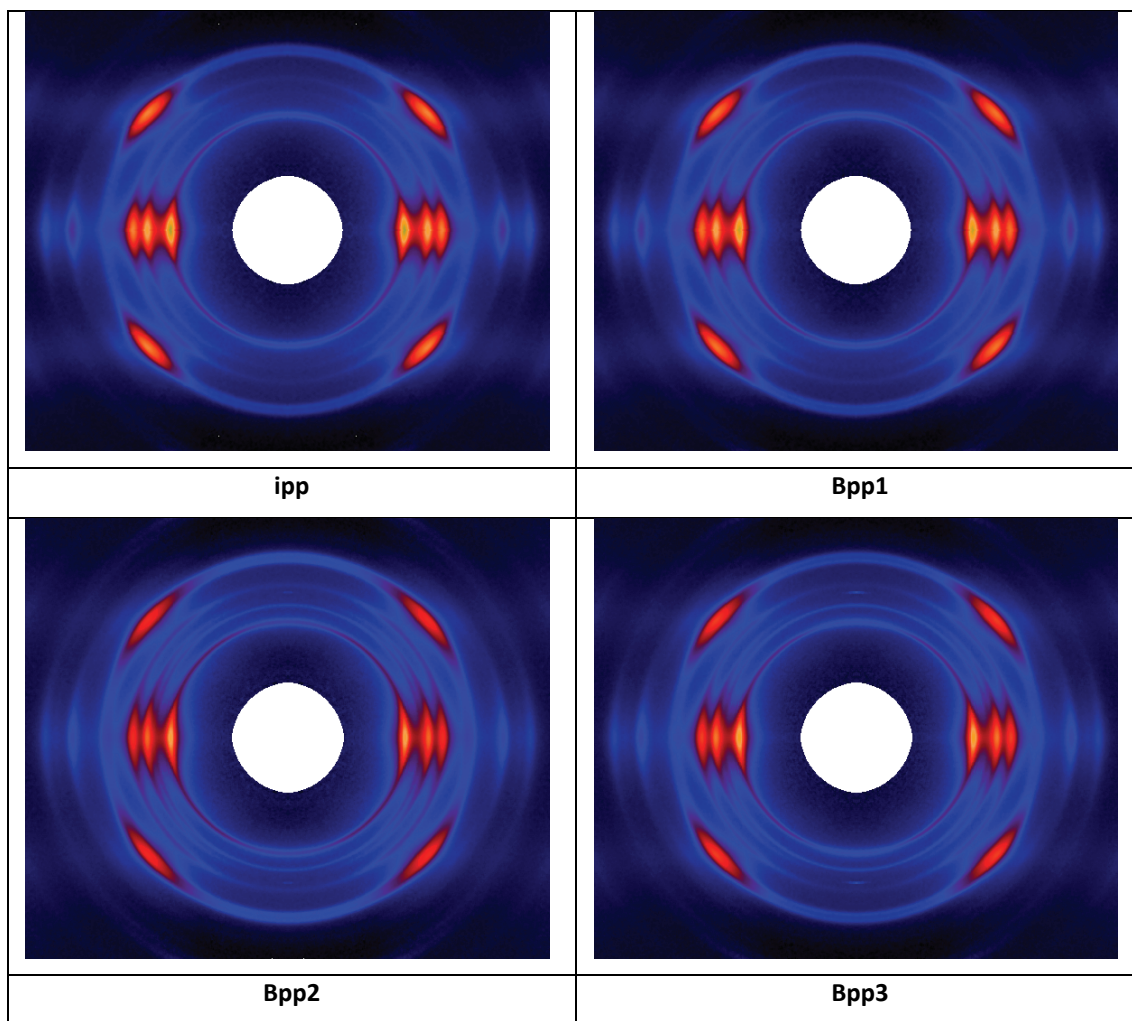


Fig. 59 WAXS patterns of iPP with different amount of  $\beta$ -nucleating agents at strain of 300%, stretching rate = 0.1 mm/s,  $T = 90^\circ\text{C}$

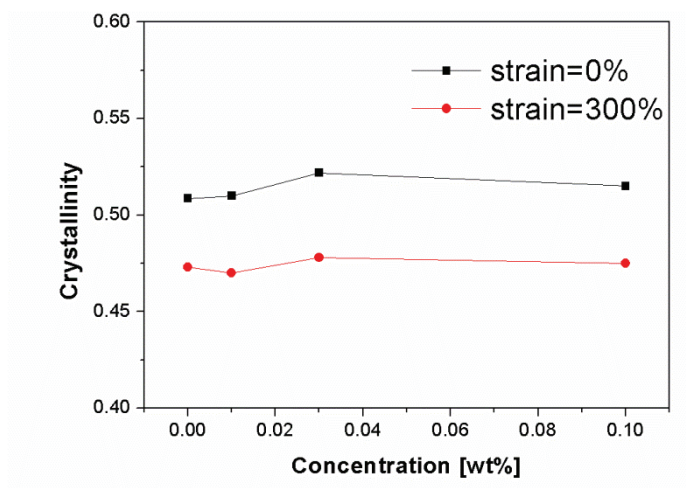


Fig. 60 Crystallinity of deformed and undeformed injection-moulded iPP samples as a function of  $\beta$ -nucleating agent concentrations,  $T = 90^\circ\text{C}$ , stretching rate = 0.1 mm/s

Fig. 61 shows  $K_\beta$  value of those iPP samples calculated based on 2D-WAXS patterns in Fig. 53 and Fig. 59. It is found that the  $\beta$ -content increases with increasing NJS concentration. After stretching to 300%, the  $\beta$ -content decreases in all of the samples indicating the transformation of  $\beta$  to other phases. In addition, it seems that such transformation in Bpp3 with higher  $\beta$ -content is more pronounced than that in Bpp2 with relatively lower  $\beta$ -content.

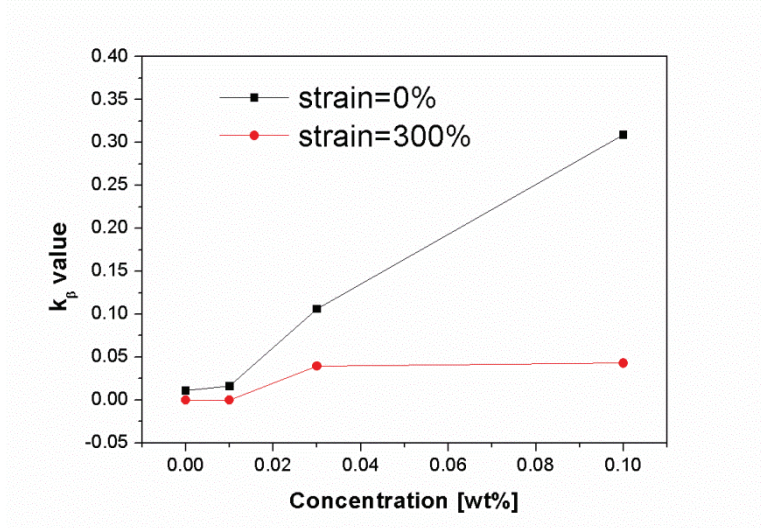


Fig. 61  $K_\beta$  value of deformed and undeformed injection-moulded iPP samples as a function of  $\beta$ -nucleating agent concentrations,  $T = 90^\circ\text{C}$ , stretching rate = 0.1 mm/s

Fig. 62 shows the change of crystal size for those deformed and undeformed iPP samples. It can be seen that the crystal size increases with increasing NJS concentration, which is consistent with the results in Fig. 59. After stretching to 300%, the crystal size markedly decreased which is also consistent with the results in Fig. 59, indicating that destruction of crystals occurred followed by the formation of smaller crystals during the deformation process.



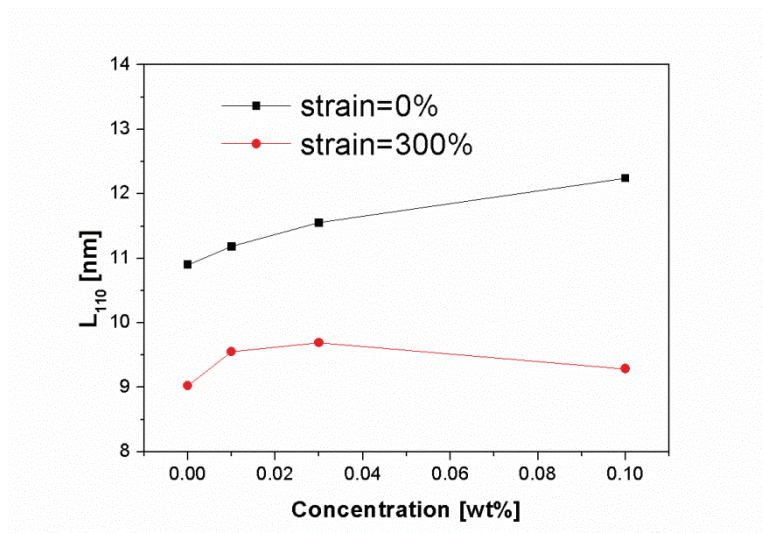


Fig. 62 Crystallite size in the normal direction of the (1 1 0) reflection plane of deformed and undeformed injection-moulded iPP samples as a function of  $\beta$ -nucleating agent concentrations,  $T = 90^\circ\text{C}$ , stretching rate = 0.1 mm/s

Fig. 63 shows the change of orientation degree, based on the  $\alpha$ -(0 4 0) lattice plane, of those deformed and undeformed iPP samples. It is found that the orientation degree increases with increasing NJS concentration for the undeformed iPP samples. The orientation degree of sample is averaged from its different layers. As discussed in last chapter, highly oriented  $\alpha$ -crystals are dominant in the shear layer of all the iPP samples. The core region of pure iPP and Bpp1 is mainly composed of little oriented  $\alpha$ -crystals which leading to decrease their overall orientation degree. With increasing NJS concentration (Bpp2 and Bpp3), the shear layer is widened and there are less  $\alpha$ -crystals in the core region, both factors increasing the overall orientation degree. After stretching to 300%, all samples exhibit similar orientation degree with values of around 0.55. The increase of orientation degree in pure iPP, Bpp1 and Bpp2 may be attributed to the alignment of crystals including the new formed small crystals to the stretching direction, while the decrease of orientation degree in Bpp3 can be mainly attributed to the destruction and rearrangement of crystals in shear layer as well as the formation of more  $\alpha$ -crystals with relatively less orientation degree.

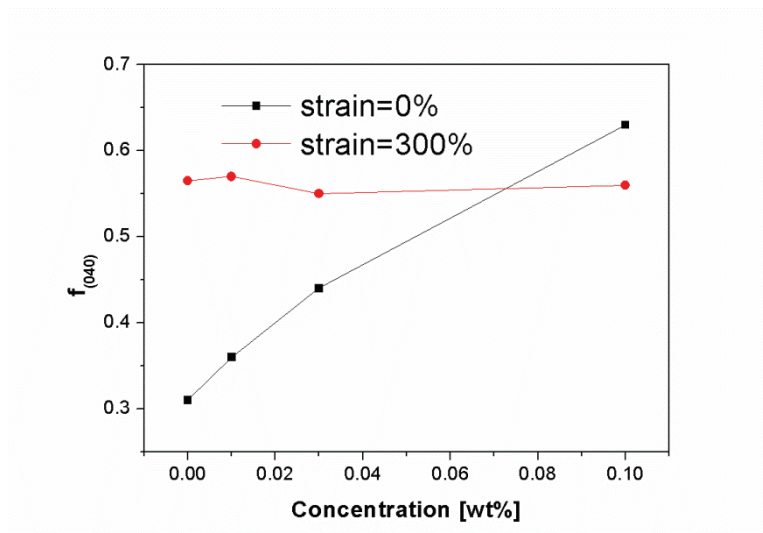


Fig. 63 Orientation parameter of the lattice plane (0 4 0) for deformed and undeformed injection-moulded iPP samples as a function of  $\beta$ -nucleating agent concentrations,  $T = 90\text{ }^{\circ}\text{C}$ , stretching rate = 0.1 mm/s

## 6.5.2 Influence of thermomechanical history on the injection-moulded samples

### 6.5.2.1 Mechanical behaviour of injection-moulded samples under uniaxial stretching

The true stress-strain curves upon uniaxial stretching of injection-moulded Bpp2 samples at different positions (see Fig. 7) of injection-moulded plate under stretching rate of 0.1 mm/s at  $90\text{ }^{\circ}\text{C}$  are shown in Fig. 64. The strains are limited to around 300%, since it is already sufficient to follow the key structure variations by synchrotron X-ray during deformation. It is found that the sample at position 1 (Bpp2-in-1) exhibits higher true stretching stresses than that at position 2 (Bpp2-in-2) over the given deformation process. The mechanical behaviour of polymers is closely associated with its initial structure and its subsequent variation caused by stretching. Hence, it is assumed that the difference of stress-strain curves of the injection-moulded Bpp2 samples under stretching may be correlated with their different experienced thermomechanical histories during the injection moulding processing and their different structure evolution upon stretching. This assumption will be further confirmed by the in-situ WAXS and SAXS analysis in the following sections.

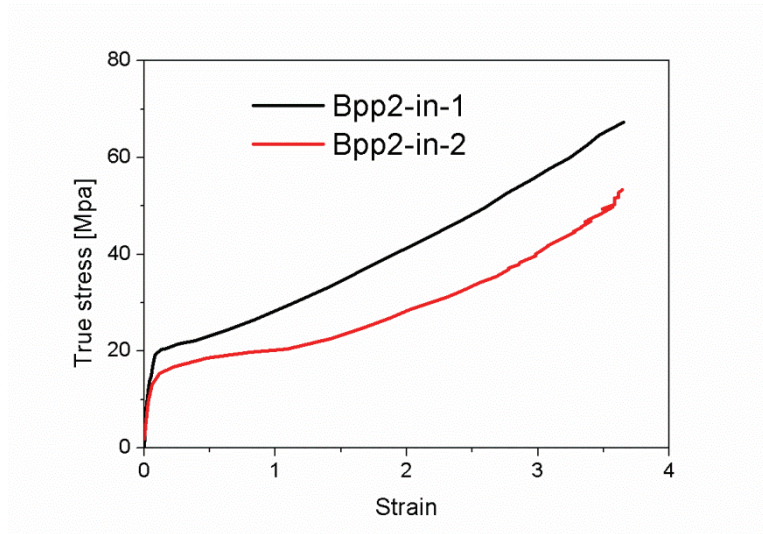


Fig. 64 True stress-strain curves of Bpp2 samples at different position.  $T = 90\text{ }^{\circ}\text{C}$ , stretching rate = 0.1 mm/s.

### 6.5.2.2 In-situ WAXS analysis

To elucidate the crystalline textural variations during stretching, a series of 2D-WAXS patterns for Bpp2 samples taken from different positions of the injection-moulded plate are shown as a function of strains in Fig. 65. In the original 2D-WAXS patterns (strain = 0) of both samples, six rings from inside to outside represent the diffractions of  $\alpha$ -(1 1 0),  $\beta$ -(3 0 0),  $\alpha$ -(0 4 0),  $\alpha$ -(1 3 0),  $\beta$ -(3 1 1)/ $\alpha$ -(1 1 1) and  $\alpha$ -(0 4 1), respectively. All of the rings show arc-like diffractions indicating the existence of oriented structure. To compare the orientation degree of these two samples (strain = 0),  $\alpha$ -(0 4 0) diffraction ring was analyzed by Hermans' function and it is found that Bpp2-in-1 with  $f_H = 0.44$  exhibits higher crystal orientation than the Bpp2-in-2 with  $f_H = 0.36$ . It is reasonable since the former underwent higher shear rate during the injection moulding processing. In addition, it can be observed that upon stretching to strain of around 0.75 the arc-like scattering rings tend to be isotropic and the scattering intensity at equator of the rings of  $\alpha$ -(1 1 0),  $\beta$ -(3 0 0),  $\alpha$ -(0 4 0) and  $\alpha$ -(1 3 0) lattice planes becomes weaker indicating the destruction of the oriented crystalline structure of both  $\alpha$ - and  $\beta$ -crystals during the initial stretching. Further stretching to strain of 3.7, all of the quasi isotropic scattering rings become concentrated arc-like and the scattering intensity at the arc-centre increases indicating rearrangement of crystallites and/or the formation of newly oriented structure [88]. Upon stretching, the true stress increases continuously with the strain (Fig. 64), which drives the chain disentanglements and the orientation in amorphous phase, promoting the formation of new oriented crystals. There is a dynamic balance between the formation of new crystals in amorphous phases and the breakage of existing crystals under the large local stress. Nevertheless, the rearrangement of crystallites may also play a role in the enhanced diffraction intensity at the arc-centre of each scattering ring.

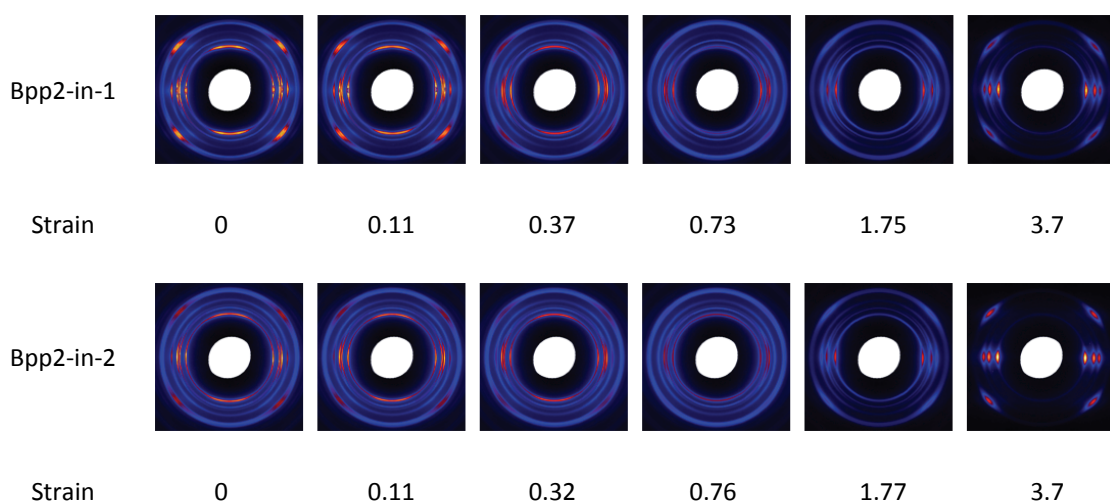


Fig. 65 Selected WAXS patterns of Bpp2 samples at position 1 and position 2 taken at different applied strains as indicated on the graph.  $T = 90\text{ }^{\circ}\text{C}$ , stretching rate = 0.1 mm/s, stretching direction is vertical, linear-scale intensity without thickness correction.

In order to clearly elucidate the individual variation of crystalline phase, the circular-integrated WAXS intensity profiles of Bpp2 samples at different positions taken at various strains are presented in Fig. 66. It is found that the intensity of all crystalline peaks decreases with increasing strains. One reason for this is that the thickness of sample gradually decreases with increasing strains leading to reduction of total scattering intensity. In addition, it can be seen that the  $\beta$ -(3 0 0) reflection peak of Bpp2-in-2 disappears at strain of 3.7 while that of Bpp2-in-1 remains to a certain extent at the same strain. This result suggests that the  $\beta$ -phase of Bpp2-in-1 exhibits high stability compared with that of Bpp2-in-2. This phenomenon will be elucidated in detail later.

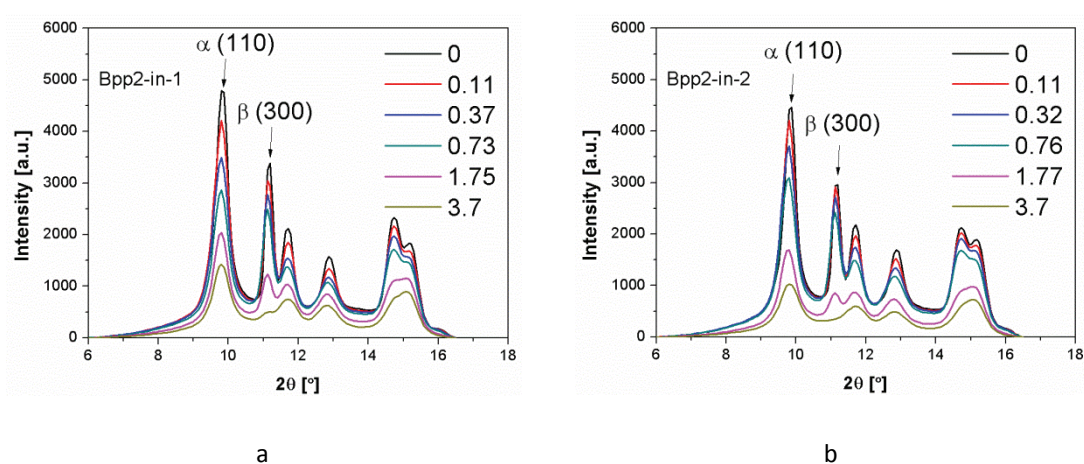


Fig. 66 Circular-integrated WAXS profiles of Bpp2 samples at position 1 (a) and position 2 (b) taken at different applied strains as indicated on the graph.  $T = 90\text{ }^{\circ}\text{C}$ , stretching rate = 0.1 mm/s.

Fig. 67 displays the evolution of overall crystallinity of these two samples. It is seen that the crystallinity decreases with increasing strains indicating the destruction of crystalline structure and reaches a plateau from strain of around 1 for both samples. The crystallinity of Bpp2-in-1 then remains almost unchanged until strain of 3.7, while for Bpp2-in-2 it starts to slightly decrease from strain of around 3.0. In contrast to the continuous decrease of overall crystallinity at the initial deformation range (strain from 0 to around 0.75), the relative amount of beta crystals increases with increasing strains before 0.75 with the tendency of Bpp2-in-1 being more remarkable than that of Bpp2-in-2 (Fig. 68 a). To take a close look, two circular-integrated WAXS intensity profiles of Bpp2 samples at position 1 taken at strain of 0 and 0.73 are shown in Fig. 68 b. Upon stretching to strain of 0.73, the intensity of main  $\alpha$ -reflection peak such as (1 1 0) and (0 4 0) decreased more pronounced than that of  $\beta$ -reflection peak (3 0 0). In fact, the  $K_\beta$  value of the original Bpp2-in-1 sample (strain = 0) is 0.202 and it increases to 0.249 upon stretching to strain of 0.73. As already discussed in the last chapter, the injection-moulded sample consists of 3 characteristic layers: skin layer, shear layer and core layer. The skin and shear layers play a key role in determining the mechanical properties of polymer by bearing the main load during initial deformation. The  $\alpha$ -phase as a dominant crystalline phase in these two layers thus underwent the higher stress and was destructed faster than the  $\beta$ -phase existed mainly in the core layer (Fig. 52 b and c). Another possible reason for the increase of relative amount of beta crystals may be associated with the evolution of  $\gamma$ -phase, which is mainly existed in the shear layer (Fig. 52 d). Although the  $\gamma$ -peak (1 1 7) is not well identified in Fig. 68 b, one may observe that the curve part in  $\gamma$ -(1 1 7) reflection becomes more concave upon stretching to 0.73 indicating the destruction of the  $\gamma$ -phase. The  $\gamma$ -phase may transform into disordered modifications intermediated between  $\alpha$ - and  $\gamma$ -phase [150]. Whether such disordered modifications do contributions to the  $\beta$ -(3 0 0) diffraction remains an open question. Further stretching to strain of 3.7, it can be seen that the  $K_\beta$  value of both samples decreases remarkably which is mainly associated with the  $\beta$  to  $\alpha$  phase transition (note that the overall crystallinity of both samples remains almost constant during this further stretching). In addition, it is observed that the  $K_\beta$  value of Bpp2-in-1 decreases slower than that of Bpp2-in-2, which is ascribed to its wider shear layer and possibly to its larger  $\gamma$ -content (Fig. 52) retarding the transformation process.

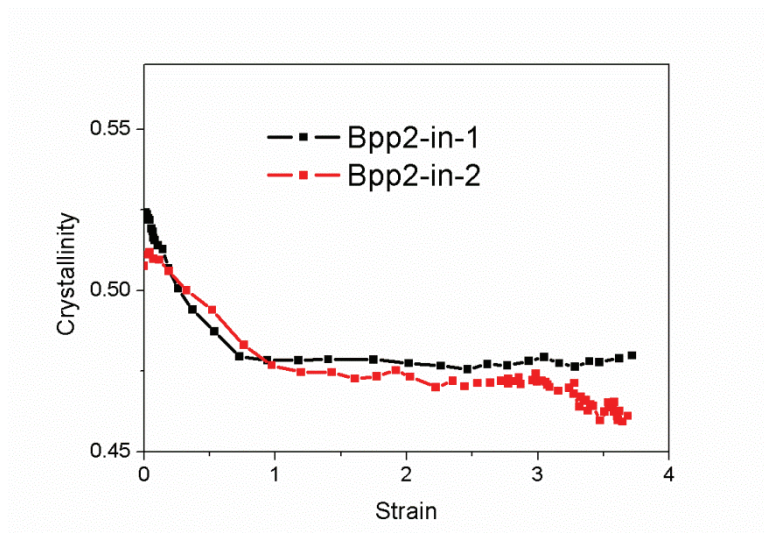


Fig. 67 Variation of overall crystallinity of Bpp2 samples at different positions with strains.  $T = 90^{\circ}\text{C}$ , stretching rate = 0.1 mm/s

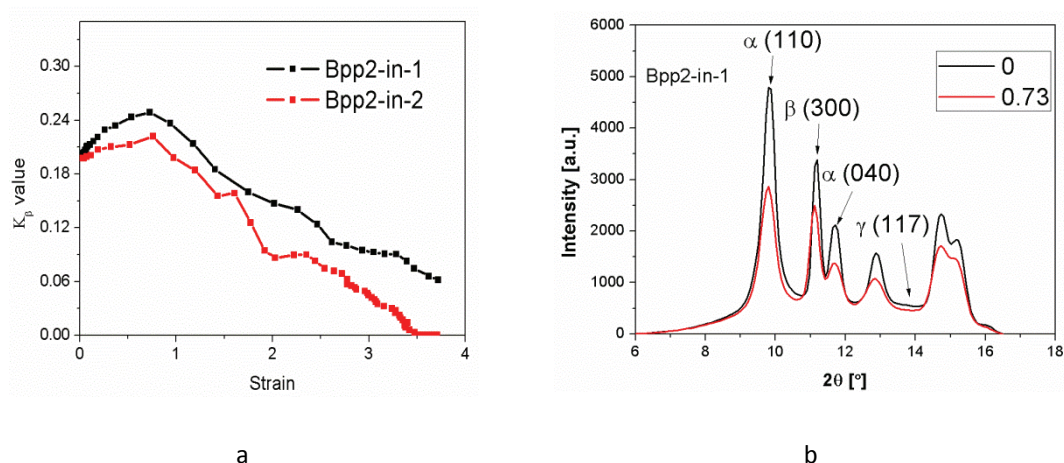


Fig. 68 Variation of the  $K_{\beta}$  value of Bpp2 samples at different positions with strains (a) and selected circular-integrated WAXS profiles of Bpp2 sample at position 1 taken at different applied strains as indicated on the graph (b).  $T = 90^{\circ}\text{C}$ , stretching rate = 0.1 mm/s

### 6.5.2.3 In-situ SAXS analysis

In-situ SAXS analysis is a powerful tool to study the evolution of cavitation and lamellar structures of semi-crystalline polymers during deformation. The SAXS scattering intensity is primarily determined by the difference of the electron densities and the volume fraction of objects, including the scattering of microvoids and cavities in the low  $q$  range as well as the lamellar structure between crystalline and amorphous phases. The scattering of cavities is much more intense than that of lamellar structure due to the strongly different electron densities. Selected 2D-SAXS patterns for Bpp2 samples taken from different positions of injection-moulded plate are displayed as a function of strains in Fig. 69. For the



reason of better visualization, the scattering patterns are shown with log-scale intensity. Both undeformed samples (strain = 0) exhibit a distinct two-spot pattern in the meridional direction indicating the presence of the layer-like lamellar structure, which is perpendicular to the injection direction and exhibits long period of 13.9 and 12.7 nm for Bpp2-in-1 and Bpp2-in-2, respectively. The scattering intensity of the two spots in the Bpp2-in-1 sample is much higher than that in Bpp2-in-2. The former one underwent higher shear rate which is beneficial for the alignment of molecular chains and thus for the formation of more ordered and perfect lamellar structure leading to enhance the electron density difference of the system and therefore increase the scattering intensity. The ordered structure of the former one can also be further confirmed by the presence of weak peaks (termed as second ordered scattering peaks) near the two spots in the meridional direction. The existence of such peaks indicates that oriented lamellar layers are well correlated, i.e. the spacing between the lamellar layers becomes quite uniform [151].

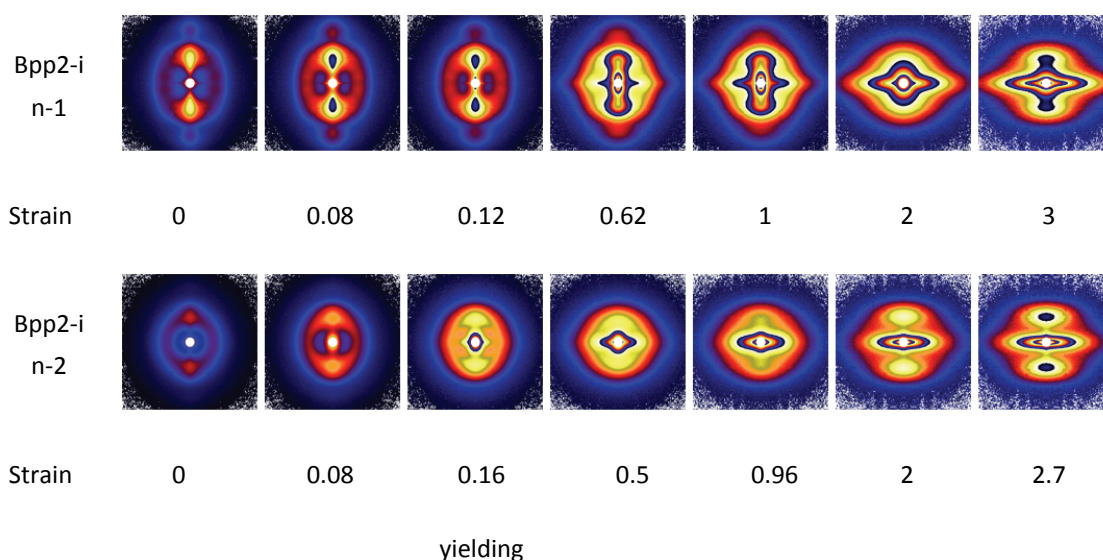


Fig. 69 Selected SAXS patterns of Bpp2 samples at position 1 and position 2 taken at different applied strains as indicated on the graph.  $T = 90^\circ\text{C}$ , stretching rate = 0.1 mm/s, stretching direction is vertical, log-scale intensity with thickness correction

Upon stretching, the variation of 2D-SAXS patterns of both samples generally shows similar trend. As an example of Bpp2-in-1 sample, a series of changes, which are assigned into two strain regions separated by yield point, can be observed as follows:

1. Upon stretching to the yield point with strain of 0.12, the overall scattering intensity obviously increases and the distinct two spots from the lamellar structure still exist. In this region, the lamellae show no significant variation and the amorphous phase between crystalline lamellae is stretched first. Hence, the increase of intensity is ascribed to the deformation of amorphous phase along stretching direction, which enhances the contrast of the electron densities between crystalline and amorphous

phases. Due to the extension of amorphous phase, the long spacing along the stretching direction increases from 13.9 to 14.6 nm. In addition, the scattering intensity in the low  $q$  range ( $q < 0.15 \text{ nm}^{-1}$ ) quickly increases which is attributed to the formation of cavities. The scattering from the cavities is not uniform, which is elongated in the meridional direction, indicating that the cavities are ellipsoid-like and orient perpendicular to the stretching direction.

2. Further stretching to strain of 3.7, the SAXS patterns continue to provide information for revealing the evolution process of cavitation and lamellar structure. The elongation of scattering patterns at low  $q$  range gradually varies from meridional to equatorial direction, which is ascribed to the orientation variation of cavities from perpendicular to parallel to stretching direction. In addition, the scattering intensity at the low  $q$  range remarkably increases indicating the generation of more cavities and/or quick propagation of the cavities during the stretching. In this region, the necking occurs and the neck propagates with the strain in the specimen. During the necking, crystal deformation may occur including crystallite shearing, slips and fragmentation, etc. Stress concentration is expected to exist in the vicinity of the crystals with relatively high plastic resistance. In the course of deformation of the crystals, the cavitation usually occurs which is primarily associated with the stress concentration. On the other hand, the occurrence of cavities in turn increases the local stress and promotes the deformation of crystallites. For the development of lamellar structure, the scattering from the lamellar layer is strongly mixed with that from the cavities, especially at strains from 0.62 to 2. However, the evolution of the second ordered peaks may give us some additional information. It is found that the second ordered peaks gradually disappear upon stretching indicating that lamellae with their normal parallel to the stretching direction lose their positional correlation. At strain of about 3 a two-spot scattering pattern forms on the meridian indicating the formation of well-oriented and correlated layered-like lamellae with long period of around 13.4 nm being apparently smaller than that at small strains from 0 to 0.12. The above results suggested that the increased stress promotes the fragmentation and/or rearrangement of crystallites followed the formation of new thinner lamellae with their normal parallel to the stretching direction.

Though the Bpp2-in-2 exhibits similar deformation process as Bpp2-in-1, there exist some certain differences. It is found that the elongation of scattering patterns for Bpp2-in-2 at low  $q$  range varies fast from meridional to equatorial direction compared with that for Bpp2-in-1 at the equivalent strains from around 0.12 to 2. This indicates that the cavities in Bpp2-in-2 are easier to reorient from perpendicular to parallel to the stretching direction. This higher 'mobility' may be associated with the originally less ordered and less perfect lamellar structure in shear layer having relatively lower plasticity resistance. Another apparent difference is that the two-spot pattern appears earlier for Bpp2-in-2 (strain = 2) than that for Bpp2-in-1 (strain = 3) during the plastic deformation. This indicates that new ordered lamellar structure with its normal parallel to the stretching direction are easily to be formed in Bpp2-in-2 via the rearrangement of crystalline blocks and/or stress-induced recrystallization



process. This phenomenon may also be related to their different morphological features mentioned above, determined by the processing history.

### 6.5.3 In-situ WAXS and SAXS analysis of $\beta$ -iPP stretched with various stretching rates

The stretching deformation behaviour of polymers depends on the strain rate. In the current thesis two distinct stretching rates, i.e. 0.1 and 1 mm/s, are selected, which may present two remarkably different strain rates, roughly as 0.02 and 0.2 s<sup>-1</sup>, respectively. In the following, the stretching rates of 0.1 and 1 mm/s are termed as low and high strain rate, respectively. The sample used in the following sections (if not specially mentioned) is Bpp2-in-1. The true stress-strain curves upon uniaxial drawing of the Bpp2 samples under different stretching rates at 90 °C are shown in Fig. 70. It is seen that the higher strain rate leads to higher true stress at the same strain. In addition, it seems that strain hardening occurs from strain of around 4 under low strain rate leading to rapidly increase the stress. At strain of 5.1, the stresses under these two strain rates are close. It is speculated that the difference of the stress-strain curves of Bpp2 samples under different strain rates may be associated with their different structure evolution and deformation behaviour upon stretching. This speculation will be further confirmed by the in-situ WAXS and SAXS analysis in the following sections.

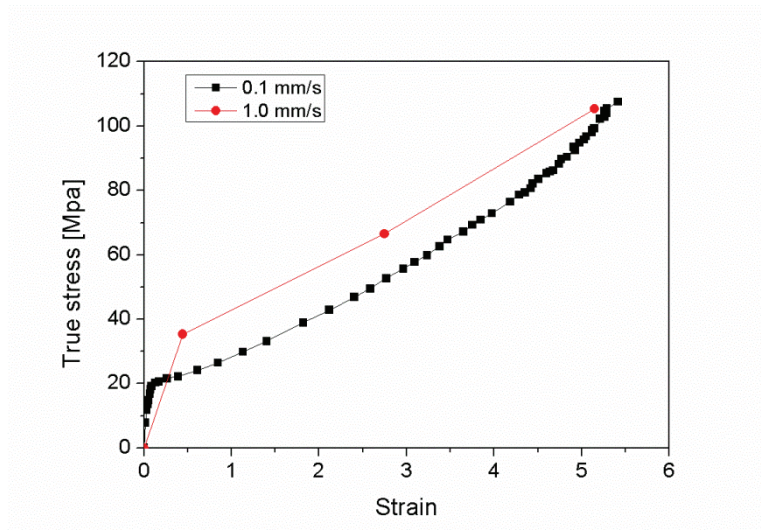


Fig. 70 True stress-strain curves for Bpp2 samples at position 1, uniaxially drawn under stretching rate of 0.1 and 1.0 mm/s at temperature of 90 °C

#### 6.5.3.1 In-situ WAXS analysis

A series of 2D-WAXS patterns for injection-moulded Bpp2 samples taken under different stretching rates are shown as a function of strains in Fig. 71 (Note: Only few WAXS patterns which correlated with the few recorded strain points in Fig. 70 are presented). It is found that the diffraction intensity of crystalline peaks under high stretching rate is relatively weak at strain > 2.7 compared with that under low stretching rate. This indicates that less amount of oriented crystals exist at the large strains under

high strain rate. As mentioned above, there is a dynamic balance between the formation of new crystals in amorphous phases and the breakage of existing crystals upon stretching. It seems that the formation of new crystals is restrained under high strain rate. This is consistence with Mahendrasingam et al. who reported that fast strain rate may delay the onset of crystallization of deformed polymer [97, 100]. On the other hand, profuse new oriented crystals formed at large strains under low strain rate, as revealed by the WAXS patterns at strains of 2.75 and 5.1, which should be responsible for the strain hardening occurring from strain of around 4 under low strain rate.

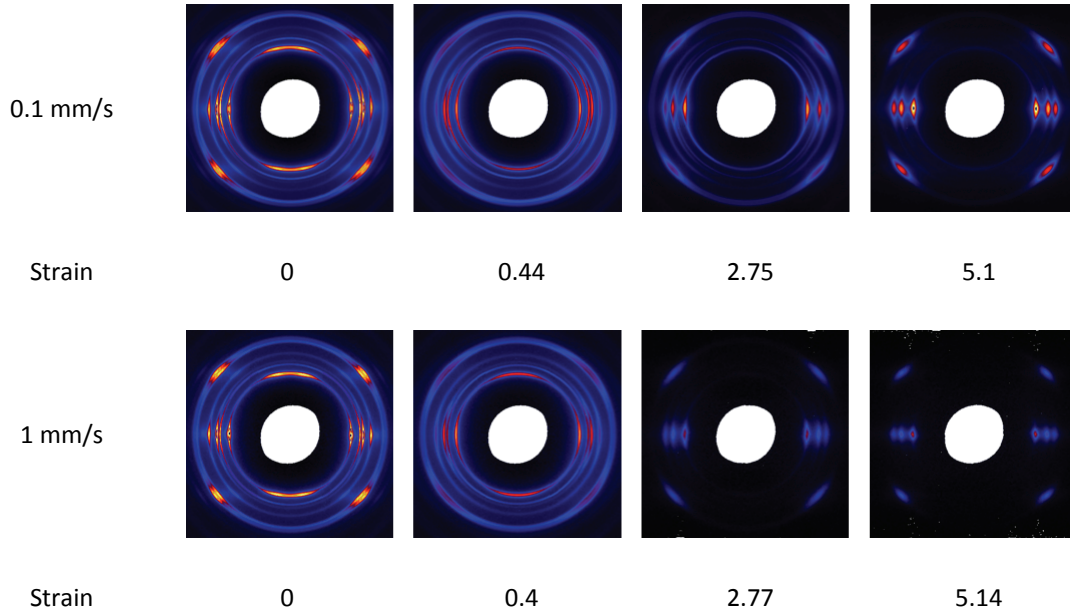


Fig. 71 Selected WAXS patterns of Bpp2 samples at position 1, uniaxially drawn under stretching rate of 0.1 and 1.0 mm/s taken at different applied strains as indicated on the graph.  $T = 90\text{ }^{\circ}\text{C}$ , stretching direction is vertical, linear-scale intensity without thickness correction

In order to check the individual variation of crystalline phase, the circular-integrated WAXS intensity profiles of Bpp2 samples stretched to the strain of around 2.75 under different strain rates are presented in Fig. 72. It is found that the  $\beta$ -(3 0 0) peak can be clearly observed under low strain rate, while it almost disappears under high strain rate indicating that the  $\beta$  to  $\alpha$  transition and/or destruction of  $\beta$ -phase proceed relatively fast under high strain rate. This result is consistence with that of Takahashi et al. who reported that the crystal transition of polymers proceeded more efficiently at higher stretching rate during uniaxial stretching at constant tensile temperature [101].

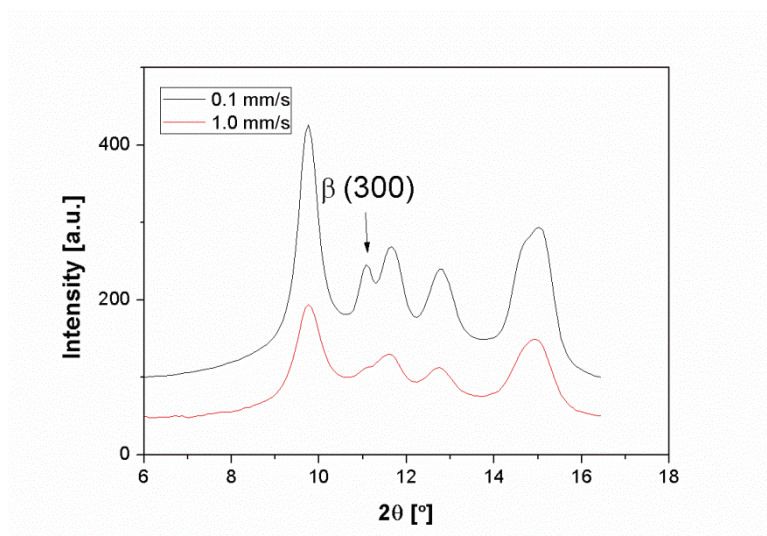


Fig. 72 WAXS intensity curves of Bpp2 samples at position 1 stretched to about 275% under stretching rate of 0.1 and 1.0 mm/s at 90 °C

#### 6.5.3.2 In-situ SAXS analysis

A series of 2D-SAXS patterns for injection-moulded Bpp2 samples taken under different stretching rates are shown as a function of strains in Fig. 73 (Note: only the SAXS patterns correlated with the few recorded strain points are presented). Upon stretching, the evolution of 2D-SAXS patterns of Bpp2 samples stretched under different stretching rates generally shows similar trend, indicating the presence of similar structure transition. The cavities gradually reorient from the perpendicular to parallel to the stretching direction. From strain of around 4.9, a two-spot pattern in the meridional direction was clearly observed, indicating the formation of well-oriented and correlated layered-like lamellae with their normal parallel to the stretching direction.

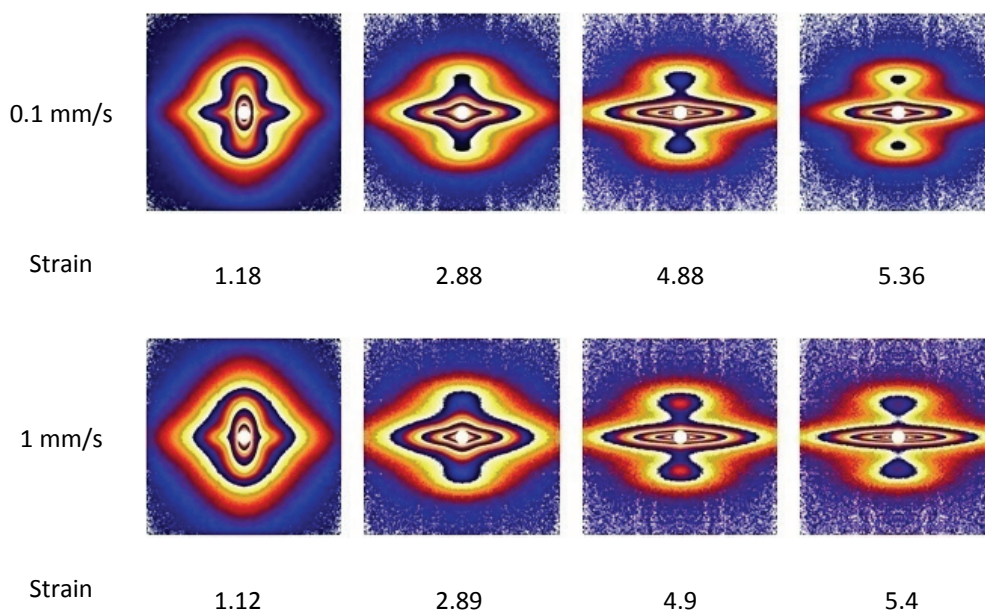


Fig. 73 Selected SAXS patterns of Bpp2 samples at position 1, uniaxially drawn under stretching rate of 0.1 and 1.0 mm/s taken at different applied strains as indicated on the graph.  $T = 90\text{ }^{\circ}\text{C}$ , stretching direction is vertical, log-scale intensity with thickness correction

#### 6.5.4 Structure variation of tensile-deformed $\beta$ -iPP at elevated temperatures - A comparison between compression- and injection-moulded samples

Two samples are used in this study: One is aforementioned injection-moulded Bpp2 sample at position 1 termed as Bpp2-in-1 and the other one is compression-moulded sample which is prepared by heating injection-moulded Bpp2 plates to  $200\text{ }^{\circ}\text{C}$  for 10 min in a vacuum press and then cooling down to room temperature at  $15\text{ K/min}$ . The purpose of this study is to further investigate how the structure and morphology of polymer may influence its mechanical properties and its structure evolution during deformation at elevated temperatures.

Simultaneous synchrotron SAXS (complete) and WAXS (partial) experiments according to [78] were performed at beamline BW4 at HASYLAB, DESY, Hamburg. The WAXS images were captured by a tilted Pilatus 300K detector which was determined to have a tilt angle of  $23.3^{\circ}$  and was able to capture the main interesting equatorial scattering with respect to the stretching direction. The distance between the sample and the point of normal incidence was 198 mm. Since the main crystalline diffractions including  $\beta$ -(3 0 0),  $\alpha$ -(0 4 0) and  $\alpha$ -(1 3 0) reflections concentrated on the equator during the deformation, the changes of equatorial scattering may reflect the evolution of crystalline structure during the deformation. The data processing for the partially recorded WAXS pattern are shown in Fig. 74. Only the selected region in WAXS pattern (Fig. 74 b) will be considered in the following sections.

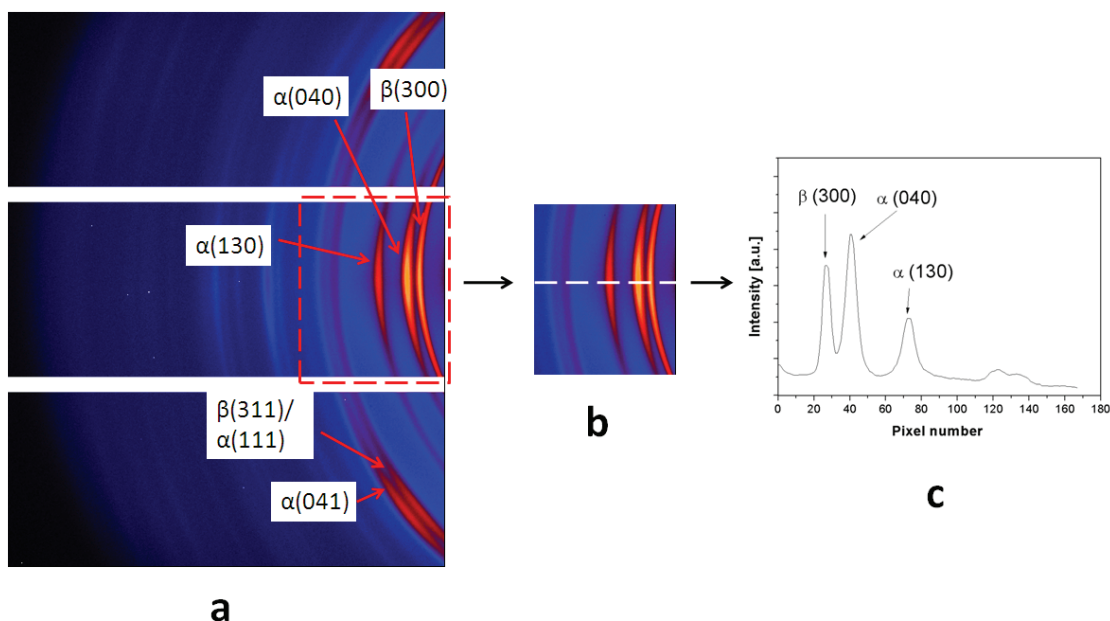


Fig. 74 Illustration of data processing for tilted WAXS patterns: (a) original WAXS pattern with stretching direction being vertical, the main reflections are indicated on the graph; (b) selected WAXS pattern section from (a), this section reflects the variation of equatorial scattering with respect to stretching direction; (c) linear WAXS profile taken from the intensity in the equatorial direction of 2D WAXS pattern (indicated as broken line in (b))

#### 6.5.4.1 Mechanical behaviour of injection- and compression-moulded samples under uniaxial stretching

The true stress-strain curves upon uniaxial stretching of injection- and compression-moulded Bpp2 samples under stretching rate of 0.02 mm/s at two different elevated temperatures of 70 and 110 °C are shown in Fig. 75. The strains were limited to around 300%, since it is already sufficient to follow the key structure variations by synchrotron X-ray during deformation. It is found that the injection-moulded sample exhibits higher true stretching stress at relatively lower temperature of 70 °C than the compression-moulded sample at the same temperature as well as the same injection-moulded sample at relatively higher temperature of 110 °C over the given deformation process (Note: the tensile experiment for compression-moulded sample was also performed at 110 °C, however, the stretching rate is 0.12 mm/s, thus the curve is not shown here). The different mechanical behaviour is assumed to be related to their different initial morphology and their different structure evolution upon stretching at different temperatures. This assumption will be further confirmed by the in-situ simultaneous WAXS and SAXS analysis in the following sections.



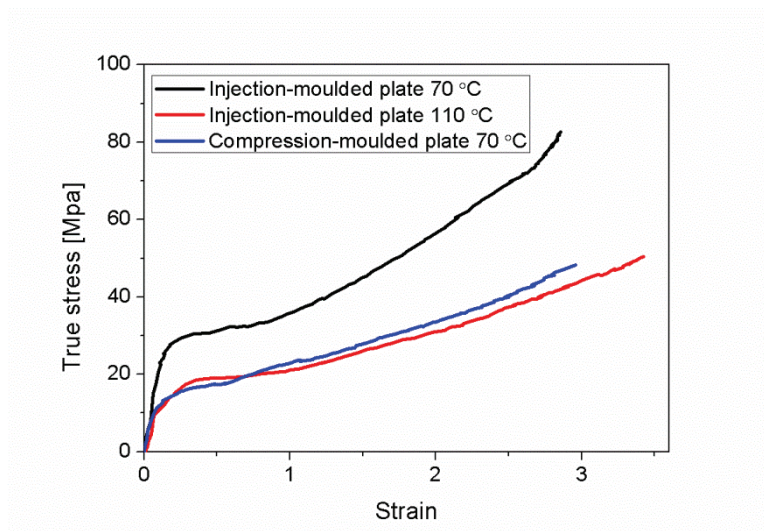


Fig. 75 True stress-strain curves of injection- and compression-moulded Bpp2 samples at given temperatures indicated on the graph. Stretching rate = 0.02 mm/s.

#### 6.5.4.2 Stretching at 70°C

A series of 2D SAXS and WAXS patterns for compression- and injection-moulded Bpp2 samples stretched at 70 °C are shown as a function of strains in Fig. 76 and Fig. 77, respectively. As expected, the original scattering patterns (strain = 0) of the two samples are quite distinct from one another indicating the presence of remarkably different morphology in both samples. For the compression-moulded sample, the original 2D SAXS and WAXS patterns seems nearly isotropic indicating that there is no obvious orientation in the undeformed sample. The long period calculated from the SAXS pattern is 18.4 nm. In addition, the original WAXS pattern exhibits 2 very strong diffraction rings corresponding to  $\beta$ -(3 0 0) and  $\beta$ -(3 1 1) (from inner to outer), respectively, indicating that the  $\beta$ -crystalline phase is overwhelmingly dominant in the crystalline phase of compression-moulded Bpp2 sample. On the other hand, for the injection-moulded sample highly oriented structure, as discussed in the previous sections, can be deduced from the original X-ray patterns. And the original WAXS pattern indicates that  $\alpha$ - and  $\beta$ -phases coexist with the  $\alpha$ -phase being more pronounced. The initial morphologic structure of polymer may strongly influence its mechanical properties.  $\beta$ -iPP exhibits lower crystal density, melting temperature and fusion enthalpy than  $\alpha$ -iPP. The corresponding mechanical properties of  $\beta$ -iPP thus differ significantly to that of  $\alpha$ -iPP. It is reported that the  $\beta$ -iPP shows a low E-modulus and yield stress compared to  $\alpha$ -iPP [15]. This may be the main reason that the true stretching stress of injection-moulded sample is higher than that of the compression-moulded sample at 70 °C.

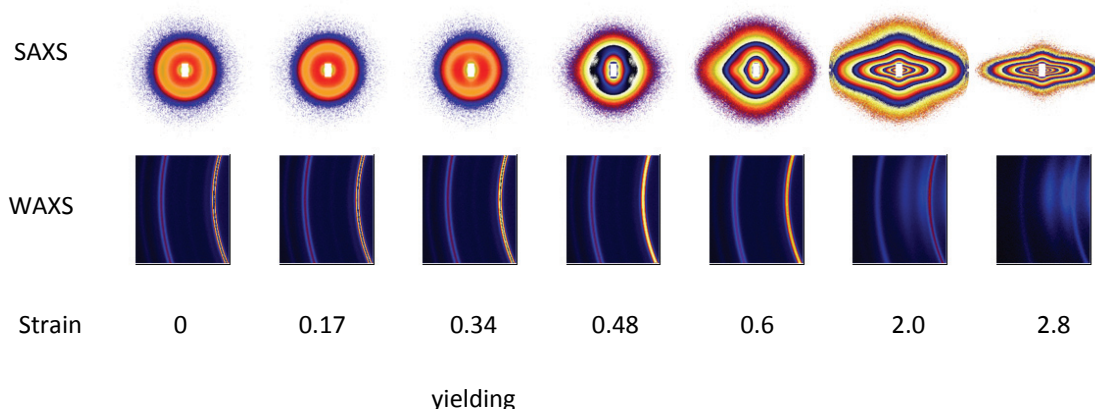


Fig. 76 Selected SAXS and WAXS patterns of compression-moulded Bpp2 samples taken at different applied strains as indicated on the graph. Stretching direction is vertical,  $T = 70\text{ }^{\circ}\text{C}$ , stretching rate =  $0.02\text{ mm/s}$ , with thickness correction, log-scale intensity for SAXS patterns, linear-scale intensity for WAXS patterns

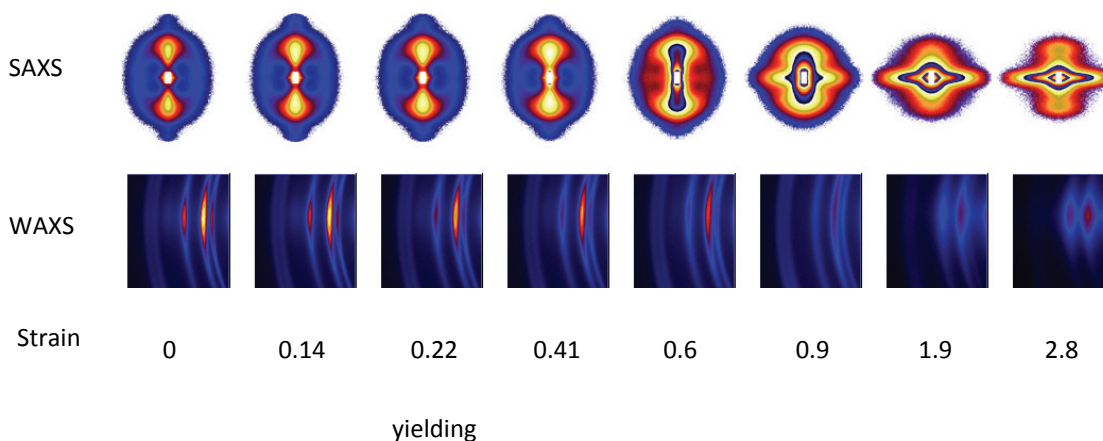


Fig. 77 Selected SAXS and WAXS patterns of injection-moulded Bpp2 samples taken at different applied strains as indicated on the graph. Stretching direction is vertical,  $T = 70\text{ }^{\circ}\text{C}$ , stretching rate =  $0.02\text{ mm/s}$ , with thickness correction, log-scale intensity for SAXS patterns, linear-scale intensity for WAXS patterns

Upon stretching to yielding, the slight increase of intensity from the lamellar structure in both samples is attributed to the deformation of amorphous phase along stretching direction, which enhances the contrast of the electron densities between crystalline and amorphous phases. With further stretching, cavities form which initially orient perpendicular and then gradually reorient parallel to the stretching direction. The scattering intensity of cavities in compression-moulded sample is obviously larger than that in injection-moulded sample, indicating the generation of more cavities. It turns out that the cavitation of polymer is sensitive to its thermomechanical history. The cooling rate in the compression moulding process is significantly lower than that in injection moulding process. This may lead to formation of relatively large and perfect crystals in compression-moulded sample, which exhibit high

plastic resistance facilitating the occurrence of cavitation [102]. On the other hand, due to the density difference with the density of  $\alpha$ -crystals being higher than that of  $\beta$ -crystals, volume contraction is a nature result of  $\beta$  to  $\alpha$  transformation upon stretching. It was reported that  $\beta$  to  $\alpha$  transformation was associated with microvoiding [152].

In order to elucidate the individual variation of crystalline phase, the linear WAXS intensity profiles of compression- and injection-moulded Bpp2 samples taken from the equatorial slice of 2D WAXS patterns at different strains are presented in Fig. 78 and Fig. 79, respectively. For the compression-moulded sample, it is found that the diffraction intensity of  $\beta$ -(3 0 0) peaks decreases with increasing strains in both samples. One reason for this is that the thickness of sample gradually decreases with increasing strains leading to reduction of total scattering intensity. The other reasons may only be destruction of  $\beta$ -crystals, occurrence of  $\beta$  to  $\alpha$  transition and/or orientation of  $\beta$ -crystals. Upon stretching to strain of 0.6, no sign of  $\beta$  to  $\alpha$  transition is observed (Fig. 78) and the corresponding  $\beta$ -(3 0 0) and (3 1 1) diffraction rings in Fig. 76 are nearly isotropic indicating that the influence of orientation of  $\beta$ -crystals can be principally ruled out. It is further noted that the intensity curves obtained at strains from 0 to 0.6 are almost coincident (excluding the peak regions of  $\beta$ -crystals), implying that the change of thickness plays a minor role in the intensity reduction in this deformation region, thus the main reason for the intensity reduction is associated with the destruction of  $\beta$ -crystals during the initial deformation. With further stretching to higher strain, the diffraction peaks of  $\alpha$ -crystals appear suggesting the occurrence of  $\beta$  to  $\alpha$  transformation. The  $\beta$  to  $\alpha$  transition mechanism is still under much debate. Stress-induced polymeric phase transformations can be mainly explained by solid martensitic-like phase transition or partial melting-recrystallization processes [125]. For long time the melting and recrystallization theory is dominant in the literatures related to  $\beta$  to  $\alpha$  transformation, however, without any clear physical evidence. The  $\beta$  to  $\alpha$  martensitic transformation seems problematic since due to the different chain helical handedness in  $\alpha$ - and  $\beta$ -crystals it involves a 'chain rewinding' process, which has been considered impossible in solid state. Until recently, it was demonstrated by Xu et al. that it was also possible since the presence of conformational defects in polymer chains may gradually reverse the helical handedness of iPP chains during compression deformation [153]. Nevertheless, our result, i.e. destruction of  $\beta$ -crystals during the initial stretching deformation, tends to support the melting-recrystallization theory. In addition, it can be seen that upon stretching to strain of around 0.34 the  $\beta$ -(3 0 0) reflection peak shift to higher pixel number corresponding to higher  $q$  value (or higher scattering angle) in inserted illustration in Fig. 78, indicating that in transversal direction the interplanar distance of  $\beta$ -(3 0 0) is shortened during the stretching. With further stretching the interplanar distance remains constant. Similar results are also found in the injection-moulded sample (Fig. 79), and it is consistent with Schneider, who found that the deformation in the crystalline phase is limited and suggested that the deformation in amorphous phase is mainly responsible for the extension of polymers at large strains [78]. From Fig. 79 it can also be observed that the  $\beta$ -(3 0 0) diffraction peak of injection-moulded sample nearly disappears from strain of around 1.9. Combined with the two-spot SAXS pattern at strain of 2.8 (Fig. 77), it can be



inferred that the scattering of the two spots is resulted from the highly oriented  $\alpha$ -crystalline lamellae. In contrast, no apparent scattering from crystalline lamellae is observed in the SAXS pattern of compression-moulding sample at the same strain (Fig. 76), possibly due to the very strong scattering from cavities.

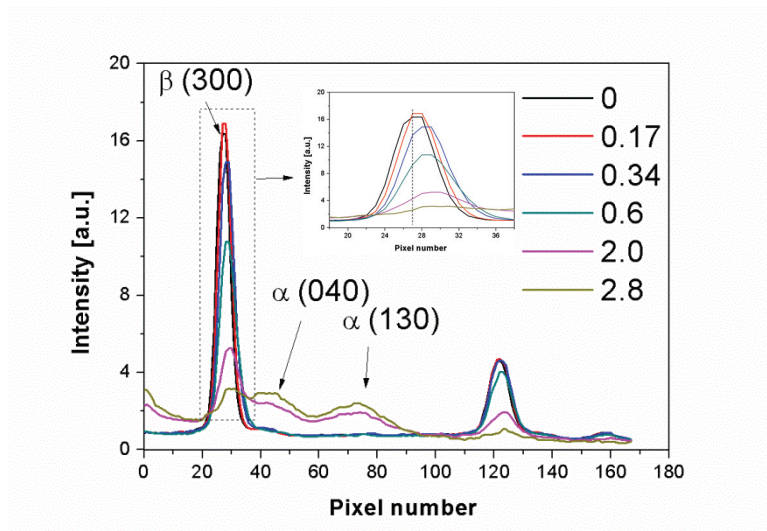


Fig. 78 Linear WAXS profiles of compression-moulded Bpp2 samples taken from the intensity in the equatorial direction of 2D WAXS patterns at different strains.  $T = 70\text{ }^{\circ}\text{C}$ , stretching rate = 0.02 mm/s

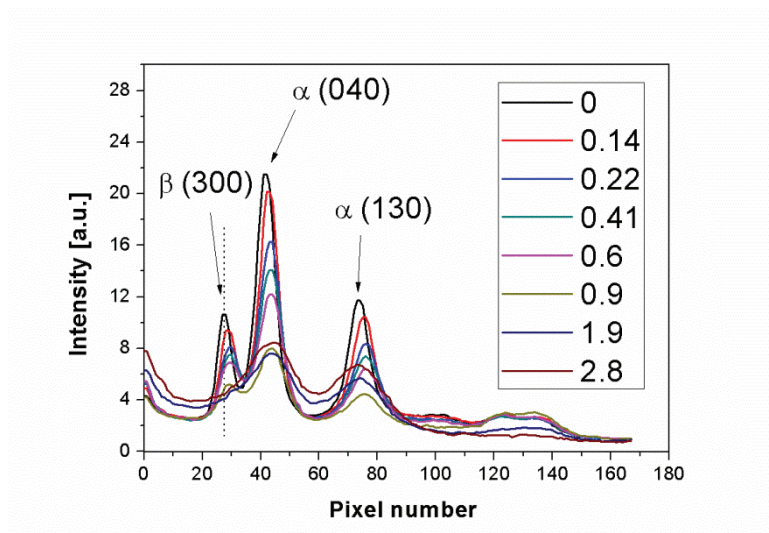


Fig. 79 Linear WAXS profiles of injection-moulded Bpp2 samples taken from the intensity in the equatorial direction of 2D WAXS patterns at different strains.  $T = 70\text{ }^{\circ}\text{C}$ , stretching rate = 0.02 mm/s.

#### 6.5.4.3 Stretching at $110\text{ }^{\circ}\text{C}$

As mentioned above, the compression-moulded sample is stretched with obviously different stretching rate of 0.12 mm/s at  $110\text{ }^{\circ}\text{C}$ , however, the X-ray data will also be analyzed and shown later for a reason of semi-qualitative comparison. Here, attention is firstly paid to the injection-moulded sample.

A series of 2D SAXS and WAXS patterns for injection-moulded Bpp2 samples stretched at  $110\text{ }^{\circ}\text{C}$  with the same stretching rate of 0.02 mm/s as that at  $70\text{ }^{\circ}\text{C}$  are shown as a function of strains in Fig. 80. From the SAXS patterns it can be found that the cavitation doesn't occur during the stretching which may be ascribed to the higher chain mobility at higher stretching temperature. Upon stretching the equatorial scattering from the lamellar structure gradually disappears indicating the destruction or rearrangement of crystalline lamellae with their normal perpendicular to the stretching direction. The second ordered peak in the meridional direction readily disappears upon stretching from strain of 0.21 to 0.94 implying that the original lamellae with their normal parallel to the stretching direction disorder to a certain extent upon stretching. At the same time, the scattering intensity of the two-spot pattern decreases gradually with increasing strain indicating the occurrence of fragmentation of the lamellae. With further stretching, the two-spot intensity increases at strain of 1.97 and then decreases at strain of 3.4 suggesting the coexistence of destruction of original lamellae and formation of new lamellar stacks. The intensity of equatorial streak at low  $q$  range becomes stronger from strain of 0.94 suggesting the formation of strain-induced fibrillar structure. The evolution of meridional long period with strain is presented in Fig. 81. It is found that the original long period is 14.5 nm, obviously higher than that of 13.9 nm at  $70$  and  $90\text{ }^{\circ}\text{C}$ , indicating that the crystallization of the Bpp2 sample is nearly

completed above 90 °C but below 110 °C during the injection moulding process. Upon stretching, the long period readily increases to strain of about 1, remains almost constant until strain of 1.97, and increases further to about 17.0 nm, i.e. being 2.5 nm higher than that in initial undeformed state, at the strain of 3.4. Similar results have been found by Jiang et al., who investigated the high density-polyethylene stretched at elevated temperature and explained the increase of long period with strains by the melt and recrystallization of original lamellar crystallites at a temperature, under which the crystallization is not finished during the preparation processing [23].

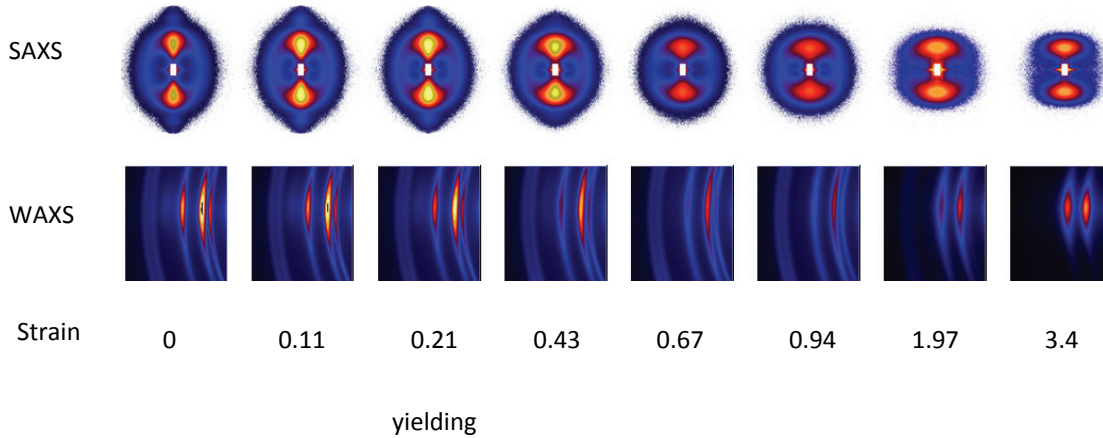


Fig. 80 Selected SAXS and WAXS patterns of injection-moulded Bpp2 samples taken at different applied strains as indicated on the graph. Stretching direction is vertical,  $T = 110\text{ }^{\circ}\text{C}$ , stretching rate = 0.02 mm/s, with thickness correction, log-scale intensity for SAXS patterns, linear-scale intensity for WAXS patterns.

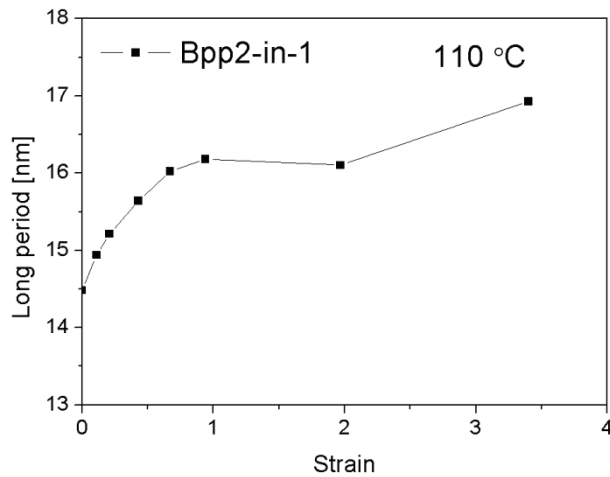


Fig. 81 The change of meridional long period of injection-moulded Bpp2 samples stretched at 110 °C as a function of strain. Stretching rate = 0.02 mm/s.

The linear WAXS intensity profiles of the injection-moulded Bpp2 samples taken from the intensity in the equatorial direction of 2D WAXS patterns at different strains are presented in Fig. 82. It is found that peak position of  $\beta$ -(3 0 0) remains almost unchanged, which is different to the stretching at 70 °C. This may be associated with the higher chain mobility at higher temperature.

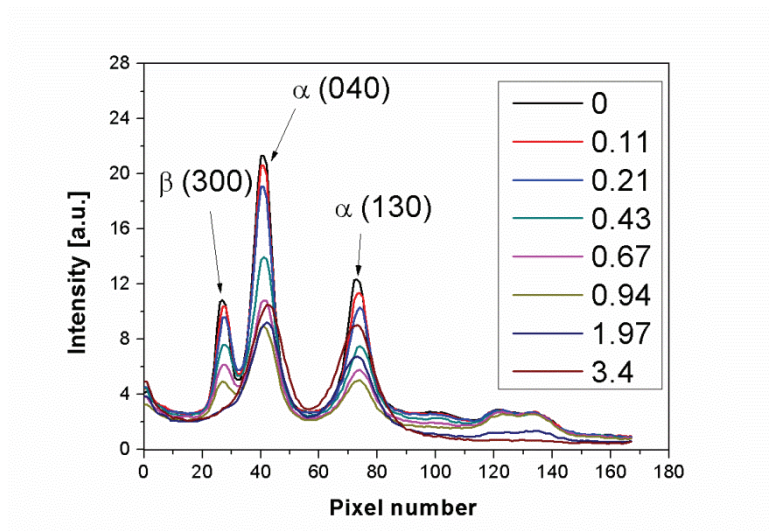


Fig. 82 Linear WAXS profiles of injection-moulded Bpp2 samples taken from the intensity in the equatorial direction of 2D WAXS patterns at different strains. T = 110 °C, stretching rate = 0.02 mm/s.

A series of 2D SAXS and WAXS patterns for compression-moulded Bpp2 samples stretched at 110°C with obviously high stretching rate of 0.12 mm/s are shown as a function of strains in Fig. 83. Upon stretching, the appearance of strong equatorial streaks in SAXS pattern indicates that cavities form and orient parallel to the stretching direction. This is different to that of injection-moulded sample, in which no cavitation has been detected by SAXS. Although the quick stretching rate may easily initiate the formation of cavities, the appearance of such equatorial streak in SAXS pattern is typical for  $\beta$ -rich iPP sample during stretching [138, 154]. In addition, the two-spot patterns are also observed at large strains (strain > 2.5). In contrast, no such pattern is observed in compression-moulded sample at 70 °C upon stretching to strain of around 5.1 (Fig. 76, the patterns at strain > 2.8 are not shown). The appearance of the two-spot pattern in the meridional direction at 110 °C indicates the presence of oriented lamellae with their normal parallel to the stretching direction. WAXS patterns at 110 °C indicate the occurrence of  $\beta$  to  $\alpha$  transformation.

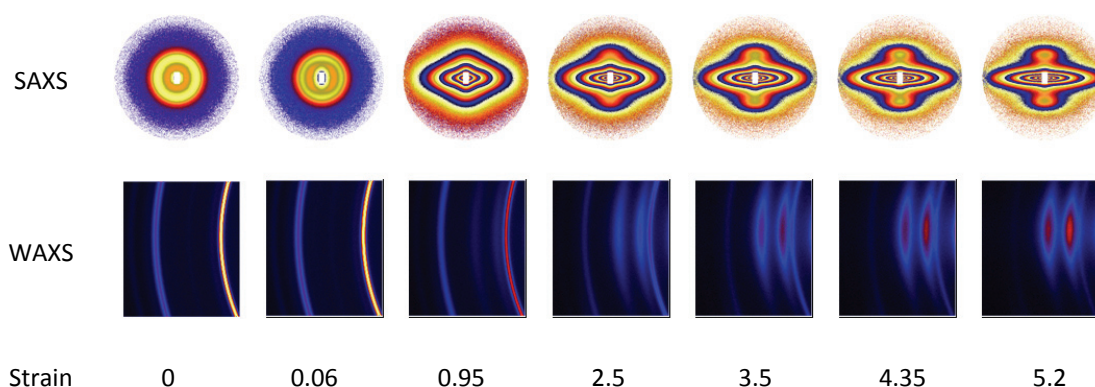


Fig. 83 Selected SAXS and WAXS patterns of compression-moulded Bpp2 samples taken at different applied strains as indicated on the graph. Stretching direction is vertical,  $T = 110\text{ }^{\circ}\text{C}$ , stretching rate =  $0.12\text{ mm/s}$ , with thickness correction, log-scale intensity for SAXS patterns, linear-scale intensity for WAXS patterns.

The linear WAXS intensity profiles of the compression-moulded Bpp2 samples taken from the intensity in the equatorial direction of 2D WAXS patterns at different strains are presented in Fig. 84. Similar to the injection-moulded sample stretched at  $110\text{ }^{\circ}\text{C}$  (Fig. 82), it is also found that peak position of  $\beta$ -(3 0 0) remains almost unchanged upon stretching, which is possible associated with the higher chain mobility at higher stretching temperature. In addition, combining with Fig. 83 it is observed that unoriented  $\beta$ -phase gradually transformed into oriented  $\alpha$ -phase during stretching.

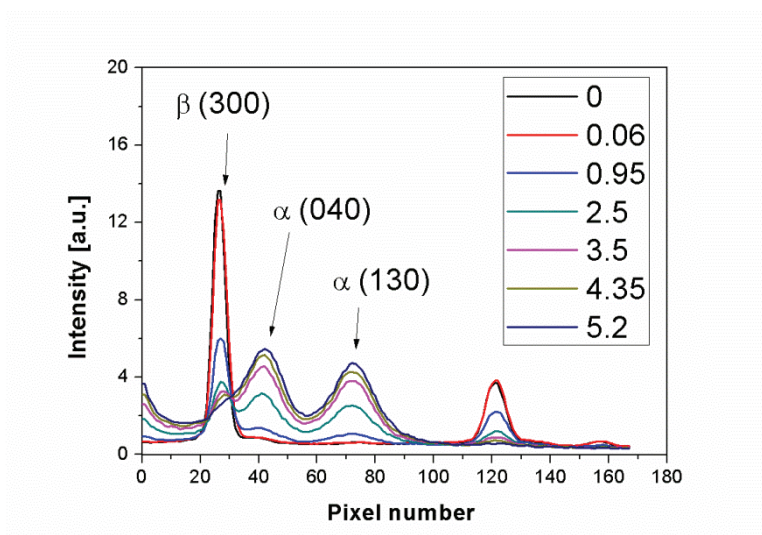


Fig. 84 Linear WAXS profiles of compression-moulded Bpp2 samples taken from the intensity in the equatorial direction of 2D WAXS patterns at different strains.  $T = 110\text{ }^{\circ}\text{C}$ , stretching rate =  $0.12\text{ mm/s}$ .

## 7 Conclusion

The object of this thesis was to investigate the influence of various thermomechanical histories on the crystallization and deformation behaviour of  $\beta$ -nucleated iPP by time-resolved synchrotron WAXS and SAXS techniques. The nucleation and growth behaviour of  $\beta$ -nucleated iPP with different content of  $\beta$ -nucleating agents at the early stage of shear induced crystallization was firstly studied. The crystallization kinetics was described by a simplified Avrami equation. It was found that the  $\beta$ -nucleating agent at different concentrations displayed different morphologies in iPP melt and their presence strongly influenced the crystallization kinetics. At small concentration, the  $\beta$ -nucleating agent completely dissolved in the iPP melt at the beginning of isothermal crystallization and recrystallized in the form of fine crystals during subsequent isothermal crystallization, which had high selectivity to induce the formation of nearly pure  $\beta$ -crystals without specific orientation. The application of shear did not change the  $\beta$ -nucleating ability of the NJS. On the other hand, for the iPP samples with high content of  $\beta$ -nucleating agent, there were a large amount of recrystallized NJS particles existing in the iPP melt at the beginning of isothermal crystallization. These particles exhibited dual nucleating ability and their  $\beta$ -nucleating ability increased with time under quiescent condition. However, under shear, the  $\beta$ -nucleating ability was strongly retarded which was possibly related to the formation of a large amount of oriented  $\alpha$ -nuclei surrounding the particles inhibiting the formation of  $\beta$ -crystals on the surface of  $\beta$ -nucleating agent particles. Nevertheless, a few amount of  $\beta$ -crystal content was formed during the isothermal crystallization and it can be mainly attributed to the  $\alpha$  to  $\beta$  growth transition taking place on the  $\alpha$ -row nuclei. In addition, it was found that the addition of  $\beta$ -nucleating agent was beneficial for the molecular alignment during processing and the anisotropic particles were much more effective to align the molecular chains in the flow direction compared to the isotropic one. Moreover, the SAXS results indicate that the shear strongly changes the lamellar stacking manner which is mainly associated with the change of content ratio between  $\alpha$ - and  $\beta$ -crystals as well as the stretching of molecular chains under shear.

Special attention was paid to the  $\beta$ -nucleated iPP with anisotropic needle-like shape of nucleating agent particles in the melt prior to application of shear. The influence of various shear rate and shear temperatures on the crystallization process was investigated. It was found that the overall crystallization rate of this  $\beta$ -nucleated iPP unexpectedly decreased at low shear rates of 2 and 10 s<sup>-1</sup> compared with that under quiescent condition, which was attributed to the strong reduction of  $\beta$ -nucleating efficiency after application of shear. Nevertheless, upon application of shear (shear rate from 2 to 50 s<sup>-1</sup>) the overall crystallization rate increased with increasing shear rate which is mainly associated with the increased  $\alpha$ -crystallization rate. However, the higher the shear rate was, the lower the  $\beta$ -content can be obtained in the final solid state. In addition, the dimensionality of crystal growth geometry basically decreased while the long period of lamellar structure tended to slightly increase as the shear rate increased from 2 to 50 s<sup>-1</sup>. The possible explanation could be given in this way that the higher shear rate is beneficial for the formation of crystals with higher orientation degree as well as

the formation of thicker and more stable lamellae. The crystallization temperature plays a crucial role in the shear-induced crystallization process of polymers. The crystallization rate increased while the dimensionality of crystal growth geometry basically decreased with decreasing temperature. Higher temperature ( $T \geq 143\text{ }^{\circ}\text{C}$ ) suppressed whereas the lower temperature ( $T \leq 138\text{ }^{\circ}\text{C}$ ) promoted the formation of  $\beta$ -crystals. Nevertheless, the  $\beta$ -content was always minor in  $\beta$ -nucleated iPP sheared under various temperatures, not only during the given isothermal crystallization, but also in final solid state. By analyzing the WAXS patterns at solid state for  $\beta$ -nucleated iPP sheared at higher temperatures (143 and 150  $^{\circ}\text{C}$ ), it was further verified that the presence of  $\beta$ -crystals formed during the isothermal shear-induced crystallization with relatively high shear rate of  $50\text{ s}^{-1}$  can be mainly attributed to the  $\alpha$  to  $\beta$  growth transition taking place on the  $\alpha$ -row nuclei. In addition, an abnormal evolution of long period, i.e. long period obviously increased with time, was found at  $\beta$ -nucleated iPP sheared at 133  $^{\circ}\text{C}$ . The reason remains unknown and it is possibly associated with the increase of  $\beta$ -content.

Compared to shear flow, extensional flow is much more effective for orienting the polymer chains and accelerating the crystallization. Inspired from the fiber spinning process, in which extensional flow is dominant, a novel melt draw experiment was designed which was able to realize a high extension of molecular chains. It was found that the addition of  $\beta$ -nucleating agent strongly influenced the extension induced crystallization process. In-situ WAXS measurement showed that 6 well-defined spots on the main  $\beta$ -reflection (3 0 0) developed with time under the presence of  $\beta$ -nucleating agent indicating that oriented  $\beta$ -crystals grew with their chain axis aligned perpendicular to the melt drawing direction during the isothermal extension induced crystallization. Small angle X-ray scattering (SAXS) revealed that the existence of  $\beta$ -nucleating agent promoted the formation of shish. In addition, a distinct 4-spot SAXS pattern was observed indicating that well-oriented lamellar structure was formed in  $\beta$ -nucleated iPP during the extension induced crystallization and it was demonstrated that the scattering of the spots perpendicular to drawing direction (equatorial scattering) was mainly attributed to the oriented  $\beta$ -lamellae, initiated by the needle-like  $\beta$ -nucleating agent and not the oriented  $\alpha$ -row crystals, as occurred in the above shear-induced crystallization. This study indicated that the oriented  $\beta$ -lamellae and shish-kebab structure developed simultaneously in  $\beta$ -nucleated iPP during the extension induced crystallization.

The mechanical properties of iPP depend strongly on its crystallinity, crystal orientation and morphology as determined by preparation conditions. Before investigating the deformation behaviour of  $\beta$ -nucleated iPP with defined thermomechanical history prepared by traditional injection moulding process, samples were scanned by synchrotron X-ray microbeam to construct their overall morphological distributions, including distributions of crystallinity, lamellar thickness and orientation, etc. It was found that in  $\beta$ -nucleated iPP prepared by conventional injection moulding the outer layer (skin and shear layer) was dominated by highly oriented  $\alpha$ -form crystals, while the core layer was rich in  $\beta$ -crystals. In addition, the presence of  $\beta$ -nucleating particles significantly widened the shear layer.

The presence of nucleating agent particles promoted the alignment of molecular chains and induced more oriented nuclei. Thus overall crystallization occurred at higher temperature leading to the formation of thicker lamellae in the shear layer. The long period increased with increasing concentration of  $\beta$ -nucleating agent in the core layer, since the  $\beta$ -nucleating agent may promote the formation of  $\beta$ -crystals at high crystallization temperature leading to increase the lamellar stacking distance. The influence of thermomechanical history on the morphological distributions of  $\beta$ -nucleated iPP was also studied. It was found that higher shear rate was beneficial for the formation of more  $\gamma$ -crystals and thicker lamellae in the shear layer as well as the formation of wider shear layer.

Based on the above investigation on the morphological distributions of injection-moulded  $\beta$ -nucleated iPP, these morphology-identified samples were investigated by in-situ synchrotron X-ray measurements coupled with mechanical testing to follow the structure evolution during deformation at elevated temperatures. It was found that voids and cavities along the stretching direction existed in the deformed iPP samples and their volume increased with increasing concentration of  $\beta$ -nucleating agent. The increased volume of void and cavity was associated with the  $\beta$  to  $\alpha$  phase transition. The higher the concentration of  $\beta$ -nucleating agent used, the more the  $\beta$ -crystals transformed into the  $\alpha$ -crystals during the deformation, thus the more the cavities were generated due to the density difference between  $\alpha$ - and  $\beta$ -crystals. Upon stretching the fragmentation and rearrangement of crystallites occurred following the formation of thinner lamellae.

The mechanical behaviour of  $\beta$ -nucleated iPP was closely associated with its initial structure and its subsequent variation caused by stretching. The sample experienced with higher shear rate during injection moulding process exhibited higher true stretching stresses during the deformation process, since higher shear rate was beneficial for the formation of wider shear layer with more ordered and perfect lamellar structure, which endowed the polymer with improved mechanical properties. The relative amount of  $\beta$ -crystals in this sample decreased slower, which was ascribed to its wider shear layer and possibly to its larger  $\gamma$ -content retarding the  $\beta$  to  $\alpha$  transformation process. In addition, it was found that the  $\alpha$ -phase as a dominant crystalline phase in the skin and shear layers was destructed faster than the  $\beta$ -phase existed mainly in the core layer, which was attributed to the higher stress bore by the outer layer. Upon stretching, cavities formed with their orientation changing from perpendicular to parallel to the stretching direction and ordered lamellar structure appeared with its normal parallel to the stretching direction. It was found that cavities in sample experienced with lower shear rate were easier to reorient. This higher 'mobility' may be associated with the originally less ordered and perfect lamellar structure in shear layer having relatively lower plasticity resistance. In addition, the ordered lamellar structure was easier to be formed via the rearrangement of crystalline blocks and/or stress-induced recrystallization process.

The stretching deformation behaviour of polymers depended on the strain rate. The higher strain rate led to higher true stress at the same strain. It was found that the  $\beta$  to  $\alpha$  transition and/or destruction



of  $\beta$ -phase proceeded relatively fast under high strain rate. In addition, the strain-induced crystallization was restrained under high strain rate.

Stretching temperature played an important role in the deformation process. The higher stretching temperature led to lower stretching stress. It was found that the lower stretching temperature promoted the initiation of cavitation, while high stretching temperature stimulated the crystallite deformation without cavitation and formation of well-oriented and correlated layered-like lamellae with folded chains, which was associated with higher chain mobility under higher temperature.

Finally, a comparison of deformation behaviour between compression- and injection-moulded  $\beta$ -nucleated iPP samples was made. Thermomechanical history played an important role in the original morphological structure of polymer.  $\beta$ -phase was dominant in the crystalline structure of compression-moulded sample, while  $\alpha$ -phase was more pronounced in injection-moulded sample. It turned out that the cavitation of polymer upon stretching was also sensitive to its thermomechanical history. More cavities were generated in the compression-moulded sample during deformation. In addition, by analyzing structure evolution of the  $\beta$ -rich compression-moulded sample, it was found that basically the  $\beta$  to  $\alpha$  transformation was a two-step process, i.e. melting-recrystallization process.

## **8 Recommendation for further work**

1. The influence of concentration of  $\beta$ -nucleating agent, drawing rate and drawing temperature on the extension-induced crystallization process needs to be studied further.
2. Deformation mechanism of different layers of injection-moulded sample needs to be further explored. This can be realized by the morphological scan measurement for deformed injection-moulded sample.
3. Effects of concentration of  $\beta$ -nucleating agent, stretching rate and stretching temperature on the deformation behaviour of compression-moulded  $\beta$ -nucleated iPP need to be further studied.

## 9 Reference

1. Soccio, M., et al., *Aliphatic poly(propylene dicarboxylate)s: Effect of chain length on thermal properties and crystallization kinetics*. Polymer, 2007. **48**(11): p. 3125-3136.
2. Lotz, B., *What can polymer crystal structure tell about polymer crystallization processes?* The European Physical Journal E, 2000. **3**(2): p. 185-194.
3. Strobl, G., *From the melt via mesomorphic and granular crystalline layers to lamellar crystallites: A major route followed in polymer crystallization?* The European Physical Journal E, 2000. **3**(2): p. 165-183.
4. Somani, R.H., I. Sics, and B.S. Hsiao, *Thermal stability of shear-induced precursor structures in isotactic polypropylene by rheo-X-ray techniques with couette flow geometry*. Journal of Polymer Science Part B: Polymer Physics, 2006. **44**(24): p. 3553-3570.
5. Soccio, M., et al., *Effect of transesterification reactions on the crystallization behaviour and morphology of poly(butylene/diethylene succinate) block copolymers*. European Polymer Journal, 2009. **45**(1): p. 171-181.
6. Sommer, J.-U., *Theoretical Aspects of the Equilibrium State of Chain Crystals*, in *Progress in Understanding of Polymer Crystallization*, G. Reiter and G. Strobl, Editors. 2007, Springer Berlin Heidelberg. p. 19-45.
7. Bassett, D.C., *Polymer morphology: Pure and applied*. Journal of Macromolecular Science, Part B, 1996. **35**(3-4): p. 277-294.
8. Varga, J., *Supermolecular structure of isotactic polypropylene*. Journal of Materials Science, 1992. **27**(10): p. 2557-2579.
9. Wen, H., et al., *Time-Resolved Synchrotron SAXS Observations on Sheared Syndiotactic Poly(propylene) Crystallization Process*. Macromolecular Chemistry and Physics, 2008. **209**(16): p. 1721-1729.
10. Zhang, B., et al., *Formation of [beta]-cylindrites under supercooled extrusion of isotactic polypropylene at low shear stress*. Polymer, 2011. **52**(9): p. 2075-2084.
11. Cavallo, D., et al., *Flow Memory and Stability of Shear-Induced Nucleation Precursors in Isotactic Polypropylene*. Macromolecules, 2010. **43**(22): p. 9394-9400.
12. Chen, Y.H., et al., *Competitive Growth of alpha- and beta-Crystals in beta-Nucleated Isotactic Polypropylene under Shear Flow*. Macromolecules, 2010. **43**(16): p. 6760-6771.
13. Xu, J.-Z., et al., *Graphene Nanosheets and Shear Flow Induced Crystallization in Isotactic Polypropylene Nanocomposites*. Macromolecules, 2011. **44**(8): p. 2808-2818.

14. Zhao, G.Y., et al., *Effect of Shear on the Crystallization of the Poly(ether ether ketone)*. Journal of Polymer Science Part B-Polymer Physics, 2010. **48**(2): p. 220-225.
15. Varga, J.,  *$\beta$ -MODIFICATION OF ISOTACTIC POLYPROPYLENE: PREPARATION, STRUCTURE, PROCESSING, PROPERTIES, AND APPLICATION*. Journal of Macromolecular Science, Part B, 2002. **41**(4-6): p. 1121-1171.
16. Chen, Y.-H., et al., *Unusual Tuning of Mechanical Properties of Isotactic Polypropylene Using Counteraction of Shear Flow and  $\beta$ -Nucleating Agent on  $\beta$ -Form Nucleation*. Macromolecules, 2009. **42**(12): p. 4343-4348.
17. Huo, H., et al., *Influence of Shear on Crystallization Behavior of the  $\beta$  Phase in Isotactic Polypropylene with  $\beta$ -Nucleating Agent*. Macromolecules, 2004. **37**(7): p. 2478-2483.
18. Byelov, D., et al., *Crystallization under shear in isotactic polypropylene containing nucleators*. Polymer, 2008. **49**(13-14): p. 3076-3083.
19. Kotek, J., et al., *The effect of specific beta-nucleation on morphology and mechanical behavior of isotactic polypropylene*. Journal of Applied Polymer Science, 2002. **85**(6): p. 1174-1184.
20. Yamaguchi, M., et al., *Plywood-like structure of injection-moulded polypropylene*. Polymer, 2010. **51**(25): p. 5983-5989.
21. Yamaguchi, M., et al., *Anomalous molecular orientation of isotactic polypropylene sheet containing N,N'-dicyclohexyl-2,6-naphthalenedicarboxamide*. Polymer, 2009. **50**(6): p. 1497-1504.
22. Phulkerd, P., et al., *Anomalous mechanical anisotropy of  $\beta$  form polypropylene sheet with N,N'-dicyclohexyl-2,6-naphthalenedicarboxamide*. Polymer, 2011. **52**(21): p. 4867-4872.
23. Jiang, Z., et al., *Structural evolution of tensile deformed high-density polyethylene at elevated temperatures: Scanning synchrotron small- and wide-angle X-ray scattering studies*. Polymer, 2009. **50**(16): p. 4101-4111.
24. Strobl, G., *The Semicrystalline State*, in *The Physics of Polymers*. 2007, Springer Berlin Heidelberg. p. 165-222.
25. Liu, X.Y., *Heterogeneous nucleation or homogeneous nucleation?* Journal of Chemical Physics, 2000. **112**(22): p. 9949-9955.
26. Hu, W., *Intramolecular Crystal Nucleation*, in *Progress in Understanding of Polymer Crystallization*, G. Reiter and G. Strobl, Editors. 2007, Springer Berlin Heidelberg. p. 47-63.
27. Hoffman, J.D., G.T. Davis, and J.I. Lauritzen, *Treatise on solid state chemistry, edited by N.B.Hannay (Plenum, New York, 1976), Vol. 3, Chap. 7*.
28. Hoffman, J.D., *Theoretical aspects of polymer crystallization with chain folds: Bulk polymers*. Polymer Engineering & Science, 1964. **4**(4): p. 315-362.

29. Lauritzen, J.I. and J.D. Hoffman, *Formation of Polymer Crystals with Folded Chains from Dilute Solution*. Journal of Chemical Physics, 1959. **31**(6): p. 1680-1681.
30. Sadler, D.M. and G.H. Gilmer, *Rate-Theory Model of Polymer Crystallization*. Physical Review Letters, 1986. **56**(25): p. 2708-2711.
31. Sadler, D.M. and G.H. Gilmer, *Selection of lamellar thickness in polymer crystal growth: A rate-theory model*. Physical Review B, 1988. **38**(8): p. 5684-5693.
32. Liu, Y.-X. and E.-Q. Chen, *Polymer crystallization of ultrathin films on solid substrates*. Coordination Chemistry Reviews, 2010. **254**(9–10): p. 1011-1037.
33. Olmsted, P.D., et al., *Spinodal-Assisted Crystallization in Polymer Melts*. Physical Review Letters, 1998. **81**(2): p. 373-376.
34. Matsuba, G., et al., *Conformational Change and Orientation Fluctuations Prior to the Crystallization of Syndiotactic Polystyrene*. Macromolecules, 1999. **32**(26): p. 8932-8937.
35. Wang, H., *Small Angle Scattering Study of Polyethylene Crystallization from Solutions*, in *Progress in Understanding of Polymer Crystallization*, G. Reiter and G. Strobl, Editors. 2007, Springer Berlin Heidelberg. p. 169-178.
36. Stribeck, N., et al., *SAXS Study of Oriented Crystallization of Polypropylene from a Quiescent Melt*. Macromolecules, 2007. **40**(13): p. 4535-4545.
37. Keller, A. and S. Sawada, *On the interior morphology of bulk polyethylene*. Die Makromolekulare Chemie, 1964. **74**(1): p. 190-221.
38. Bassett, D.C., A.M. Hodge, and R.H. Olley, *On the Morphology of Melt-Crystallized Polyethylene II. Lamellae and their Crystallization Conditions*. Proceedings of the Royal Society of London. A. Mathematical and Physical Sciences, 1981. **377**(1768): p. 39-60.
39. Li, L., et al., *Direct Observation of Growth of Lamellae and Spherulites of a Semicrystalline Polymer by AFM*. Macromolecules, 2000. **34**(2): p. 316-325.
40. Bassett, D.C. and R.H. Olley, *On the lamellar morphology of isotactic polypropylene spherulites*. Polymer, 1984. **25**(7): p. 935-943.
41. Norton, D.R. and A. Keller, *The spherulitic and lamellar morphology of melt-crystallized isotactic polypropylene*. Polymer, 1985. **26**(5): p. 704-716.
42. Li, L. and W.H. de Jeu, *Shear-Induced Crystallization of Poly(butylene terephthalate): A Real-Time Small-Angle X-ray Scattering Study*. Macromolecules, 2004. **37**(15): p. 5646-5652.
43. Kumaraswamy, G., A.M. Issaian, and J.A. Kornfield, *Shear-Enhanced Crystallization in Isotactic Polypropylene. 1. Correspondence between in Situ Rheo-Optics and ex Situ Structure Determination*. Macromolecules, 1999. **32**(22): p. 7537-7547.
44. Janeschitz-Kriegl, H. and G. Eder, *Shear induced crystallization, a relaxation phenomenon in polymer melts: A re-collection*. Journal of Macromolecular Science Part B-Physics, 2007. **46**(3): p. 591-601.

45. Kalay, G. and M.J. Bevis, *Processing and physical property relationships in injection-molded isotactic polypropylene. 1. Mechanical properties*. Journal of Polymer Science Part B: Polymer Physics, 1997. **35**(2): p. 241-263.
46. Kalay, G. and M.J. Bevis, *Processing and physical property relationships in injection-molded isotactic polypropylene. 2. Morphology and crystallinity*. Journal of Polymer Science Part B: Polymer Physics, 1997. **35**(2): p. 265-291.
47. Somani, R.H., et al., *Flow-induced shish-kebab precursor structures in entangled polymer melts*. Polymer, 2005. **46**(20): p. 8587-8623.
48. Graham, R.S., *Modelling flow-induced crystallisation in polymers*. Chemical Communications, 2014. **50**(27): p. 3531-3545.
49. Shen, B., et al., *Shear-Induced Crystallization at Polymer–Substrate Interface: The Slippage Hypothesis*. Macromolecules, 2011. **44**(17): p. 6919-6927.
50. Mykhaylyk, O.O., et al., *Control of Structural Morphology in Shear-Induced Crystallization of Polymers*. Macromolecules, 2010. **43**(5): p. 2389-2405.
51. De Gennes, P.G., *Coil-stretch transition of dilute flexible polymers under ultrahigh velocity gradients*. J. Chem. Phys. , 1974. **60**(12): p. 5030-5042.
52. Keum, J.K., et al., *Probing nucleation and growth behavior of twisted kebabs from shish scaffold in sheared polyethylene melts by in situ X-ray studies*. Polymer, 2007. **48**(15): p. 4511-4519.
53. Mackley, M.R. and A. Keller, *Flow induced crystallization of polyethylene melts*. Polymer, 1973. **14**(1): p. 16-20.
54. Pope, D.P. and A. Keller, *A study of the chain extending effect of elongational flow in polymer solutions*. Colloid and Polymer Science, 1978. **256**(8): p. 751-756.
55. Miles, M.J. and A. Keller, *Conformational relaxation time in polymer solutions by elongational flow experiments: 2. Preliminaries of further developments: chain retraction; identification of molecular weight fractions in a mixture*. Polymer, 1980. **21**(11): p. 1295-1298.
56. Mackley, M.R., F.C. Frank, and A. Keller, *Flow-induced crystallization of polyethylene melts*. Journal of Materials Science, 1975. **10**(9): p. 1501-1509.
57. Farrell, C.J., et al., *Conformational relaxation time in polymer solutions by elongational flow experiments: 1. Determination of extensional relaxation time and its molecular weight dependence*. Polymer, 1980. **21**(11): p. 1292-1294.
58. Kimata, S., et al., *Molecular Basis of the Shish-Kebab Morphology in Polymer Crystallization*. Science, 2007. **316**(5827): p. 1014-1017.
59. Nogales, A., et al., *Shear-induced crystallization of isotactic polypropylene with different molecular weight distributions: in situ small- and wide-angle X-ray scattering studies*. Polymer, 2001. **42**(12): p. 5247-5256.

60. Avila-Orta, C.A., et al., *Shear-induced crystallization of isotactic polypropylene within the oriented scaffold of noncrystalline ultrahigh molecular weight polyethylene*. Polymer, 2005. **46**(20): p. 8859-8871.
61. Duplay, C., et al., *Shear-induced crystallization of polypropylene: Influence of molecular weight*. Journal of Materials Science, 2000. **35**(24): p. 6093-6103.
62. Zuo, F., et al., *Thermal Stability of Shear-Induced Shish-Kebab Precursor Structure from High Molecular Weight Polyethylene Chains*. Macromolecules, 2006. **39**(6): p. 2209-2218.
63. Smook, J. and A. Pennings, *Elastic flow instabilities and shish-kebab formation during gel-spinning of ultra-high molecular weight polyethylene*. Journal of Materials Science, 1984. **19**(1): p. 31-43.
64. Zhang, C., et al., *Formation of cylindrite structures in shear-induced crystallization of isotactic polypropylene at low shear rate*. Polymer, 2007. **48**(4): p. 1105-1115.
65. Shen, B., et al., *Mechanism for Shish Formation under Shear Flow: An Interpretation from an in Situ Morphological Study*. Macromolecules, 2013. **46**(4): p. 1528-1542.
66. Kanaya, T., et al., *Hierarchic Structure of Shish-Kebab by Neutron Scattering in a Wide Q Range*. Macromolecules, 2007. **40**(10): p. 3650-3654.
67. Yan, T., et al., *Critical Strain for Shish-Kebab Formation*. Macromolecules, 2009. **43**(2): p. 602-605.
68. Tian, N., et al., *Extension Flow Induced Crystallization of Poly(ethylene oxide)*. Macromolecules, 2011. **44**(19): p. 7704-7712.
69. Cui, K., et al., *Self-Acceleration of Nucleation and Formation of Shish in Extension-Induced Crystallization with Strain Beyond Fracture*. Macromolecules, 2012. **45**(13): p. 5477-5486.
70. Hobbs, J.K., *Crystallization Kinetics*, in *Encyclopedia of Polymer Science and Technology*. 2002, John Wiley & Sons, Inc.
71. Agarwal, P.K., et al., *Shear-Induced Crystallization in Novel Long Chain Branched Polypropylenes by in Situ Rheo-SAXS and -WAXD*. Macromolecules, 2003. **36**(14): p. 5226-5235.
72. Phillips, A., P.-W. Zhu, and G. Edward, *Polystyrene as a versatile nucleating agent for polypropylene*. Polymer, 2010. **51**(7): p. 1599-1607.
73. Vega, J., D. Hristova, and G. Peters, *Flow-induced crystallization regimes and rheology of isotactic polypropylene*. Journal of Thermal Analysis and Calorimetry, 2009. **98**(3): p. 655-666.
74. Chen, Y.-H., et al., *In Situ Synchrotron X-ray Scattering Study on Isotactic Polypropylene Crystallization under the Coexistence of Shear Flow and Carbon Nanotubes*. Macromolecules, 2011. **44**(20): p. 8080-8092.
75. Keum, J.K., F. Zuo, and B.S. Hsiao, *Formation and Stability of Shear-Induced Shish-Kebab Structure in Highly Entangled Melts of UHMWPE/HDPE Blends*. Macromolecules, 2008. **41**(13): p. 4766-4776.

76. Zhang, W. and J.A. Martins, *Shear-induced nonisothermal crystallization of low-density polyethylene*. Polymer, 2007. **48**(21): p. 6215-6220.
77. Sperling, L.H., *Mechanical Behavior of Polymers*, in *Introduction to Physical Polymer Science*. 2005, John Wiley & Sons, Inc. p. 557-612.
78. Schneider, K., *Investigation of structural changes in semi-crystalline polymers during deformation by synchrotron X-ray scattering*. Journal of Polymer Science Part B: Polymer Physics, 2010. **48**(14): p. 1574-1586.
79. Li, J.X. and W.L. Cheung, *On the deformation mechanisms of  $\beta$ -polypropylene: 1. Effect of necking on  $\beta$ -phase PP crystals*. Polymer, 1998. **39**(26): p. 6935-6940.
80. Peterlin, A., *Molecular model of drawing polyethylene and polypropylene*. Journal of Materials Science, 1971. **6**(6): p. 490-508.
81. Flory, P.J. and D.Y. Yoon, *Molecular morphology in semicrystalline polymers*. Nature, 1978. **272**(5650): p. 226-229.
82. Juska, T. and I.R. Harrison, *A criterion for craze formation*. Polymer Engineering & Science, 1982. **22**(12): p. 766-776.
83. Popli, R. and L. Mandelkern, *Influence of structural and morphological factors on the mechanical properties of the polyethylenes*. Journal of Polymer Science Part B: Polymer Physics, 1987. **25**(3): p. 441-483.
84. Bartczak, Z. and E. Lezak, *Evolution of lamellar orientation and crystalline texture of various polyethylenes and ethylene-based copolymers in plane-strain compression*. Polymer, 2005. **46**(16): p. 6050-6063.
85. Seguela, R. and F. Rietsch, *Double yield point in polyethylene under tensile loading*. Journal of Materials Science Letters, 1990. **9**(1): p. 46-47.
86. Men, Y., J. Rieger, and G. Strobl, *Role of the entangled amorphous network in tensile deformation of semicrystalline polymers*. Phys Rev Lett. , 2003. **29**(91): p. 095502.
87. Bao, R., et al., *Deformation-induced morphology evolution during uniaxial stretching of isotactic polypropylene: effect of temperature*. Colloid and Polymer Science, 2012. **290**(3): p. 261-274.
88. Chen, Y., et al., *Structure Evolution upon Uniaxial Drawing Skin- and Core-Layers of Injection-Molded Isotactic Polypropylene by In Situ Synchrotron X-ray Scattering*. Journal of Polymer Science Part B: Polymer Physics, 2013. **51**(22): p. 1618-1631.
89. Samon, J.M., J.M. Schultz, and B.S. Hsiao, *Study of the cold drawing of nylon 6 fiber by in-situ simultaneous small- and wide-angle X-ray scattering techniques*. Polymer, 2000. **41**(6): p. 2169-2182.
90. Ran, S., et al., *Structural and Morphological Studies of Isotactic Polypropylene Fibers during Heat/Draw Deformation by in-Situ Synchrotron SAXS/WAXD*. Macromolecules, 2001. **34**(8): p. 2569-2578.
91. Kawakami, D., et al., *Deformation-Induced Phase Transition and Superstructure Formation in Poly(ethylene terephthalate)*. Macromolecules, 2004. **38**(1): p. 91-103.



92. Stoclet, G., et al., *New Insights on the Strain-Induced Mesophase of Poly(d,l-lactide): In Situ WAXS and DSC Study of the Thermo-Mechanical Stability*. *Macromolecules*, 2010. **43**(17): p. 7228-7237.
93. Zhang, X., et al., *Structure variation of tensile-deformed amorphous poly(l-lactic acid): Effects of deformation rate and strain*. *Polymer*, 2011. **52**(18): p. 4141-4149.
94. Zhang, X., et al., *Deformation-mediated superstructures and cavitation of poly (l-lactide): In-situ small-angle X-ray scattering study*. *Polymer*, 2012. **53**(2): p. 648-656.
95. Schneider, K., et al., *The Study of Cavitation in HDPE Using Time Resolved Synchrotron X-ray Scattering During Tensile Deformation*. *Macromolecular Symposia*, 2006. **236**(1): p. 241-248.
96. Cai, J., B.S. Hsiao, and R.A. Gross, *Real-Time Structure Changes during Uniaxial Stretching of Poly( $\omega$ -pentadecalactone) by in Situ Synchrotron WAXD/SAXS Techniques*. *Macromolecules*, 2011. **44**(10): p. 3874-3883.
97. Mahendrasingam, A., et al., *Time resolved study of oriented crystallisation of poly(lactic acid) during rapid tensile deformation*. *Polymer*, 2005. **46**(16): p. 6009-6015.
98. Pluta, M. and A. Galeski, *Plastic Deformation of Amorphous Poly(l/dl-lactide): Structure Evolution and Physical Properties*. *Biomacromolecules*, 2007. **8**(6): p. 1836-1843.
99. Sadler, D.M. and P.J. Barham, *Structure of drawn fibres: 1. Neutron scattering studies of necking in melt-crystallized polyethylene*. *Polymer*, 1990. **31**(1): p. 36-42.
100. Blundell, D.J., et al., *Orientation prior to crystallisation during drawing of poly(ethylene terephthalate)*. *Polymer*, 2000. **41**(21): p. 7793-7802.
101. Takahashi, K., et al., *Crystal transformation from the  $\alpha$ - to the  $\beta$ -form upon tensile drawing of poly(l-lactic acid)*. *Polymer*, 2004. **45**(14): p. 4969-4976.
102. Pawlak, A. and A. Galeski, *Plastic Deformation of Crystalline Polymers: The Role of Cavitation and Crystal Plasticity*. *Macromolecules*, 2005. **38**(23): p. 9688-9697.
103. Liu, G., et al., *Effect of elastomer on crystalline transition and deformation behavior of isotactic polypropylene*. *Polymer*, 2013. **54**(4): p. 1440-1447.
104. Pawlak, A. and A. Galeski, *Cavitation during Tensile Deformation of Polypropylene*. *Macromolecules*, 2008. **41**(8): p. 2839-2851.
105. Gahleitner, M., et al., *Crystallinity and mechanical properties of PP-homopolymers as influenced by molecular structure and nucleation*. *Journal of Applied Polymer Science*, 1996. **61**(4): p. 649-657.
106. Peacock, A.J. and A. Calhoun, *Polypropylene*, in *Polymer Science*. 2006, Hanser. p. 285-297.
107. Mao, Y., *Polymorphism, Preferred Orientation and Morphology of Propylene-Based Random Copolymer Subjected to External Force Fields*. *Stony Brook University, Ph.D. thesis*, 2011.

108. Mathieu, C., et al., "Multiple" nucleation of the (010) contact face of isotactic polypropylene,  $\alpha$  phase. *Polymer*, 2000. **41**(19): p. 7241-7253.
109. Mao, Y., et al., *Wide-Angle X-ray Scattering Study on Shear-Induced Crystallization of Propylene-1-Butylene Random Copolymer: Experiment and Diffraction Pattern Simulation*. *Macromolecules*, 2011. **44**(3): p. 558-565.
110. Natta, G. and P. Corradini, *Structure and properties of isotactic polypropylene*. *Il Nuovo Cimento Series 10*, 1960. **15**(1): p. 40-51.
111. Meille, S.V., et al., *Structure of .beta.-Isotactic Polypropylene: A Long-Standing Structural Puzzle*. *Macromolecules*, 1994. **27**(9): p. 2615-2622.
112. Meille, S.V., S. Bruckner, and W. Porzio,  $\gamma$ -Isotactic polypropylene. *A structure with nonparallel chain axes*. *Macromolecules*, 1990. **23**(18): p. 4114-4121.
113. De Rosa, C., et al., *Crystallization Behavior and Mechanical Properties of Regiodefective, Highly Stereoregular Isotactic Polypropylene: Effect of Regiodefects versus Stereodefects and Influence of the Molecular Mass*. *Macromolecules*, 2005. **38**(22): p. 9143-9154.
114. Housmans, J.-W., et al., *Structure-property relations in molded, nucleated isotactic polypropylene*. *Polymer*, 2009. **50**(10): p. 2304-2319.
115. dissertation-fischer, *Physical Properties of novel polypropylene*. 2009.
116. Zhao, S., Z. Cai, and Z. Xin, *A highly active novel  $\beta$ -nucleating agent for isotactic polypropylene*. *Polymer*, 2008. **49**(11): p. 2745-2754.
117. Stocker, W., et al., *Epitaxial Crystallization and AFM Investigation of a Frustrated Polymer Structure: Isotactic Poly(propylene),  $\beta$  Phase*. *Macromolecules*, 1998. **31**(3): p. 807-814.
118. Varga, J. and A. Menyhárd, *Effect of Solubility and Nucleating Duality of N,N'-Dicyclohexyl-2,6-naphthalenedicarboxamide on the Supramolecular Structure of Isotactic Polypropylene*. *Macromolecules*, 2007. **40**(7): p. 2422-2431.
119. Dong, M., et al., *Crystallization behavior and morphological development of isotactic polypropylene with an aryl amide derivative as  $\beta$ -form nucleating agent*. *Journal of Polymer Science Part B: Polymer Physics*, 2008. **46**(16): p. 1725-1733.
120. Phulkerd, P., et al., *Plastic deformation behavior of polypropylene sheet with transversal orientation*. *Journal of Polymer Science Part B: Polymer Physics*, 2013. **51**(11): p. 897-906.
121. Phulkerd, P., et al., *Structure and mechanical anisotropy of injection-molded polypropylene with a plywood structure*. *Polym J*, 2014. **46**(4): p. 226-233.
122. Kawai, T., et al., *Crystal orientation of  $\beta$ -phase isotactic polypropylene induced by magnetic orientation of N,N'-dicyclohexyl-2,6-naphthalenedicarboxamide*. *Polymer*, 2002. **43**(26): p. 7301-7306.

123. Karger-kocsis, J. and J. Varga, *Effects of  $\beta$ - $\alpha$  transformation on the static and dynamic tensile behavior of isotactic polypropylene*. Journal of Applied Polymer Science, 1996. **62**(2): p. 291-300.
124. Huy, T.A., et al., *Molecular deformation mechanisms of isotactic polypropylene in  $\alpha$ - and  $\beta$ -crystal forms by FTIR spectroscopy*. Journal of Polymer Science Part B: Polymer Physics, 2004. **42**(24): p. 4478-4488.
125. Lezak, E., Z. Bartczak, and A. Galeski, *Plastic deformation behavior of  $\beta$ -phase isotactic polypropylene in plane-strain compression at room temperature*. Polymer, 2006. **47**(26): p. 8562-8574.
126. Li, J.X., W.L. Cheung, and C.M. Chan, *On deformation mechanisms of  $\beta$ -polypropylene 3. Lamella structures after necking and cold drawing*. Polymer, 1999. **40**(13): p. 3641-3656.
127. Luo, F., et al., *New Understanding in Tuning Toughness of  $\beta$ -Polypropylene: The Role of  $\beta$ -Nucleated Crystalline Morphology*. Macromolecules, 2009. **42**(23): p. 9325-9331.
128. Van der Beek, M.H.E., G.W.M. Peters, and H.E.H. Meijer, *Influence of Shear Flow on the Specific Volume and the Crystalline Morphology of Isotactic Polypropylene*. Macromolecules, 2006. **39**(5): p. 1805-1814.
129. Somani, R.H., et al., *Shear-Induced Molecular Orientation and Crystallization in Isotactic Polypropylene: Effects of the Deformation Rate and Strain*. Macromolecules, 2005. **38**(4): p. 1244-1255.
130. Li, L. and L. Zhang, *The influence of thermoelastomers on the crystallization behavior of isotactic polypropylene under shear*. Journal of Polymer Science Part B: Polymer Physics, 2006. **44**(8): p. 1188-1198.
131. Patil, N., et al., *A Study on the Chain-Particle Interaction and Aspect Ratio of Nanoparticles on Structure Development of a Linear Polymer*. Macromolecules, 2010. **43**(16): p. 6749-6759.
132. Phillips, A.W., et al., *Shish Formation and Relaxation in Sheared Isotactic Polypropylene Containing Nucleating Particles*. Macromolecules, 2011. **44**(9): p. 3517-3528.
133. DESY, [http://photon-science.desy.de/facilities/petra\\_iii/index\\_eng.html](http://photon-science.desy.de/facilities/petra_iii/index_eng.html). 2014.
134. IPF, <http://www.ipfdd.de/Strain-induced-crystallization-in-natura.2706.0.html?&L=1>. 2014.
135. Pecharsky, V. and P. Zavaliy, *Fundamentals of Diffraction, in Fundamentals of Powder Diffraction and Structural Characterization of Materials*. 2009, Springer US. p. 133-149.
136. Martin, G.C., *Physical Properties of Polymers Handbook, 2nd ed Edited by James E. Mark (University of Cincinnati, OH). Springer Science + Business Media, LLC: New York. 2007*. Journal of the American Chemical Society, 2007. **130**(3): p. 0-1111.

137. Turner-Jones, A. and A.J. Cobbold, *The  $\beta$  crystalline form of isotactic polypropylene*. Journal of Polymer Science Part B: Polymer Letters, 1968. **6**(8): p. 539-546.
138. Bao, R.-Y., et al., *Deformation-induced structure evolution of oriented  $\beta$ -polypropylene during uniaxial stretching*. Polymer, 2013. **54**(3): p. 1259-1268.
139. Hermans, J.J., et al., *Quantitative evaluation of orientation in cellulose fibres from the X-ray fibre diagram*. Recueil des Travaux Chimiques des Pays-Bas, 1946. **65**(6): p. 427-447.
140. Somani, R.H., et al., *Structure Development during Shear Flow-Induced Crystallization of i-PP: In-Situ Small-Angle X-ray Scattering Study*. Macromolecules, 2000. **33**(25): p. 9385-9394.
141. Supaphol, P., J.E. Spruiell, and J.-S. Lin, *Isothermal melt crystallization and melting behaviour of syndiotactic polypropylene*. Polymer International, 2000. **49**(11): p. 1473-1482.
142. Bischoff White, E., H. Henning Winter, and J. Rothstein, *Extensional-flow-induced crystallization of isotactic polypropylene*. Rheologica Acta, 2012. **51**(4): p. 303-314.
143. Zhou, J.-J., et al., *Atomic force microscopy study of the lamellar growth of isotactic polypropylene*. Polymer, 2005. **46**(12): p. 4077-4087.
144. Ruland, W., *The evaluation of the small-angle scattering of lamellar two-phase systems by means of interface distribution functions*. Colloid & Polymer Science, 1977. **255**(5): p. 417-427.
145. Zhu, P.-w., et al., *Morphological Development of Oriented Isotactic Polypropylene in the Presence of a Nucleating Agent*. Macromolecules, 2006. **39**(5): p. 1821-1831.
146. Kumaraswamy, G., et al., *Shear-Enhanced Crystallization in Isotactic Polypropylene. In-Situ Synchrotron SAXS and WAXD*. Macromolecules, 2004. **37**(24): p. 9005-9017.
147. Zhong, G.-J. and Z.-M. Li, *Injection molding-induced morphology of thermoplastic polymer blends*. Polymer Engineering & Science, 2005. **45**(12): p. 1655-1665.
148. Zhu, P.-W., G. Edward, and L. Nichols, *Effect of additives on distributions of lamellar structures in sheared polymer: a study of synchrotron small-angle x-ray scattering*. Journal of Physics D: Applied Physics, 2009. **42**(24): p. 245406.
149. Zhu, P.-w. and G. Edward, *Distribution of Shish-Kebab Structure of Isotactic Polypropylene under Shear in the Presence of Nucleating Agent*. Macromolecules, 2004. **37**(7): p. 2658-2660.
150. Auriemma, F. and C. De Rosa, *Stretching Isotactic Polypropylene: From "cross- $\beta$ " to Crosshatches, from  $\gamma$  Form to  $\alpha$  Form*. Macromolecules, 2006. **39**(22): p. 7635-7647.

151. Somani, R.H., L. Yang, and B.S. Hsiao, *Effects of high molecular weight species on shear-induced orientation and crystallization of isotactic polypropylene*. Polymer, 2006. **47**(15): p. 5657-5668.
152. Karger-Kocsis, J. and P.P. Shang, *A modulated dsc study on the strain-induced  $\beta \rightarrow \alpha$ -transformation in a  $\beta$ -form isotactic polypropylene*. Journal of Thermal Analysis and Calorimetry, 1998. **51**(1): p. 237-244.
153. Xu, W., D.C. Martin, and E.M. Arruda, *Finite strain response, microstructural evolution and  $\beta \rightarrow \alpha$  phase transformation of crystalline isotactic polypropylene*. Polymer, 2005. **46**(2): p. 455-470.
154. Cai, Z., et al., *Real time synchrotron SAXS and WAXS investigations on temperature related deformation and transitions of  $\beta$ -iPP with uniaxial stretching*. Polymer, 2012. **53**(7): p. 1593-1601.

## Acknowledgments

First of all, I would like to express my deep gratitude to Prof. Gert Heinrich for offering me this opportunity of doing a PhD at the Leibniz Institute of Polymer Research Dresden (IPF). I would also like to thank him for his guidance, encouragement and support throughout my PhD study.

My sincerest thanks go to Dr. Schneider for bringing me to an interesting research field and giving me the freedom to independently conduct my PhD work, for his guidance and support throughout my research work. He always had an open door for me and provided many helpful discussions.

I also would like to thank Prof. René Androsch for agreeing to serve as second referee on the doctoral committee.

I am indebted to Dr. Stephan Roth, Dr. Jan Perlich, Dr. Bernd Struth and many other scientists at DESY. Synchrotron X-ray experiments are the core of this work, which would not be possible without their expertise and assistance.

Special thank goes to Mr. Liam A Killough from RiKA International Limited for kindly providing an important raw material.

I am grateful to Mr. Bernd Kretzschmar for providing support and advice for carrying out extrusion and melt injection molding, to Mr. Dietmar Krause for the sample preparation, to Mr. Dirk Zimmerhäckel for providing support for the device fabrication, to Mr. Torsten Hofmann for the in-house X-ray scattering measurement, to Mrs. Maria Auf der Landwehr for the microscopic measurement, to Mr. Holger Scheibner and Mr. Karsten Scheibe for mechanical testing, to Mrs. Liane Häussler and Mrs. Sabine Krause for DSC measurement. My gratitude extends to Prof. Edith Mäder, Dr. Petra Pötschke, Dr. Sven Pegel, Dr. Beate Krause, Mrs. Uwe Reuter for use of their labors and equipments, which have been important to the success of my study.

I would like to thank Dr. Ines Kühnert, Dr. Roland Vogel, Dr. Shanglin Gao, Dr. Chuanfu Luo for their valuable time and discussions, which have helped me achieve a deep understanding of my work and find some of the challenges along the way.

I would like to thank Prof. Heinrich and Prof. Manfred Stamm for their support during my application for the completion grant.

For financial support during my PhD thesis I would like to thank the IPF Dresden and the Graduate Academy Dresden. I am also grateful to the DESY facility for financing the beamtimes at HASYLAB.

Lots of colleagues in IPF helped me a lot either in my study or in my life in Dresden. Herein, I would like to give my acknowledgement to them, especially Dr. Rongchuan Zhuang, Mr. Debdipta Basu, Mr. Kai ke, Dr. Gaurav Kasaliwal, Dr. Shanglin Gao, Dr. Xiuqin Zhang, Dr. Guoming Liu, Mr. Guido Sebastian Sommer, Mr. Kai Huang, Dr. Kalaivani Subramaniam, Mr. Yinhu Deng, Dr. Xuezheng Cao, Dr. Yaoming Zhang, Mr. Roberto Lambardi, Dr. Arnaud Vieyres, Ms. Kristina Eichhorn, Dr. Pengcheng Ma, Dr. Victoria Dutschk, Dr. Alfredo Calvimontes.

Finally and most importantly, I would like to thank my wife Cuiting, who is caring for our newborn daughter Yanyi and in the meantime pursuing her PhD degree, for her encouragement, support, and love. You offer me strength, joy, motivation and happiness. But words can not express my gratitude. Here I would also like to convey a special piece of thanks to Yanyi for giving me a lot of delicious time. I should not forget to thank my parents Mr. Guodong Chen and Mrs. Meiying Lin. They always encouraged me to keep on, believed in my success, gave me the freedom and rights to choose the way to go and helped me in some difficult moments. I additionally thank my wonderful sister Jianping and all the rest of my extended family for their love and friendship.

## Publications and presentation

### Publications:

- 1, **Chen, J.**; Vogel, R.; Werner, S.; Heinrich, G.; Clausse, D.; Dutschk, V., Influence of the particle type on the rheological behavior of Pickering emulsions. Colloids and Surfaces A: Physicochemical and Engineering Aspects 2011, 382 (1–3), 238-245
- 2, Dutschk, V.; **Chen, J.**; Petzold, G.; Vogel, R.; Clausse, D.; Ravera, F.; Liggieri, L., The role of emulsifier in stabilization of emulsions containing colloidal alumina particles. Colloids and Surfaces A: Physicochemical and Engineering Aspects 2012, 413 (0), 239-247
- 3, Zhang, X.; Schneider, K.; Liu, G.; **Chen, J.**; Brüning, K.; Wang, D.; Stamm, M., Structure variation of tensile-deformed amorphous poly(l-lactic acid): Effects of deformation rate and strain. Polymer 2011, 52 (18), 4141-4149
- 4, Zhang, X.; Schneider, K.; Liu, G.; **Chen, J.**; Brüning, K.; Wang, D.; Stamm, M., Deformation-mediated superstructures and cavitation of poly (l-lactide): In-situ small-angle X-ray scattering study. Polymer 2012, 53 (2), 648-656
- 5, **Chen, J.**; Schneider, K.; Kretzschmar, B.; Heinrich, G., Nucleation and growth behavior of  $\beta$ -nucleated iPP during shear induced crystallization investigated by in-situ synchrotron WAXS and SAXS. Polymer 2014, 55, DOI: 10.1016/j.polymer.2014.07.058

### Presentation:

- 1, **Chen, J.**; Schneider, K.; Vogel, R.; Perlich, J. Struth. B, Brüning, K, Structural formation and development of  $\beta$ -nucleated iPP investigated by in-situ synchrotron WAXS and SAXS. S-Polymer 2012, Kerkrade, The Netherlands (oral)
- 2, **Chen, J.**; Schneider, K., Deformation behaviour of  $\beta$ -nucleated iPP investigated by in-situ WAXS/SAXS. PPS-29 2013, Nürnberg, Germany (poster)
- 3, **Chen, J.**; Schneider, K., In-situ synchrotron X-ray study on the extension induced crystallization of  $\beta$ -nucleated iPP. EP-2013 2013, Xiamen, China (poster)



## List of figures

Fig. 1	Strobl's model for the formation of polymer crystallites.....	8
Fig. 2	A schematic illustration of shish-kebab structure. During flow induced crystallization, extended chains firstly crystallized giving rise to shishes, which were served as nucleation templates for the subsequent formation of folded-chain lamellae (kebabs) [47, 48] .....	10
Fig. 3	General chemical structure of polypropylene.....	16
Fig. 4	Schematic illustration of chemical structure of 3 stereoisomers of polypropylene: (a) isotactic; (b) syndiotactic; (c) atactic .....	16
Fig. 5	Schematic illustration of $3_1$ helix conformation of polypropylene; (a) side view, (b) top view (chain-axis projection) [115] .....	17
Fig. 6	Schematic illustration of different unit cells of iPP. (a) $\alpha$ -phase, monoclinic, 4 chains per unit cell, $a = 0.665$ nm, $b = 2.096$ nm, $c = 0.65$ nm and $\beta = 99.2^\circ$ . (b) $\beta$ -phase, trigonal, 3 chains per unit cell, $a = b = 1.103$ nm, $c = 0.65$ nm. The helices in above two phases are schematized in chain-axis projection and the triangles define the methyl carbon positions. (c) $\gamma$ -phase structure with non-parallel chain packing, orthorhombic, $a = 0.854$ nm, $b = 0.993$ nm and $c = 4.241$ nm. For a better presentation, the structure is projected along one of a-b plane diagonals. Symbols R and L indicate the right- and left-handed helical chains, respectively [2]. .....	18
Fig. 7	The specimen positions in the injection moulding sheet .....	22
Fig. 8	Experimental setup, the fixed and rotating plate were made from kapton windows .....	23
Fig. 9	Sketch of morphological scan measurement .....	24
Fig. 10	Petra III experimental hall Max-von-Laue (blue) provides the world most brilliant synchrotron radiation source through storage ring [133] .....	24
Fig. 11	Custom-made miniature tensile machine used in the synchrotron X-ray measurement [134]	25
Fig. 12	Experimental setup for melt drawing.....	25
Fig. 13	Geometrical illustration of Bragg's model using 2D lattice .....	27
Fig. 14	Morphology of $\beta$ -nucleating agent at different concentrations in the iPP melt (0.01 (a), 0.03 (b) and 0.1 wt% (c)) .....	31

Fig. 15	The overall crystallinity as a function of time during the quiescent crystallization at 138 °C	32
Fig. 16	Avrami plots of $\ln(X_t)$ vs $\ln(t)$ for quiescent isothermal crystallization of iPP containing different concentrations of $\beta$ -nucleating agent at 138°C.....	33
Fig. 17	The $K_\beta$ (relative amount of $\beta$ -crystals) value as a function of time during the quiescent crystallization at 138 °C.....	36
Fig. 18	PLM micrograph of Bpp1, quiescently crystallized at 138°C, $t_c = 1.5$ min.....	36
Fig. 19	The long period as a function of time during the quiescent crystallization at 138 °C.....	37
Fig. 20	The overall crystallinity of iPP with different concentrations of $\beta$ -nucleating agent as a function of time during the quiescent crystallization (solid symbols) and flow-induced crystallization with shear rate of 50 /s (open symbols) at 138 °C.....	38
Fig. 21	Avrami plots of $\ln(X_t)$ vs $\ln(t)$ for shear-induced crystallization of iPP containing different amounts of $\beta$ -nucleating agent at 138 °C.....	38
Fig. 22	The $K_\beta$ value (relative amount of $\beta$ -crystals) of iPP with different concentrations of $\beta$ -nucleating agent as a function of time during the quiescent crystallization (solid symbols) and flow-induced crystallization with shear rate of 50 /s at 138 °C (open symbols) .....	39
Fig. 23	The $\alpha$ -crystallinity of iPP with different concentrations of $\beta$ -nucleating agent as a function of time during the quiescent crystallization (solid symbols) and flow-induced crystallization with shear rate of 50 /s at 138 °C (open symbols) .....	40
Fig. 24	The $\beta$ -crystallinity of iPP with different concentrations of $\beta$ -nucleating agent as a function of time during the quiescent crystallization(solid symbols) and flow-induced crystallization with shear rate of 50 /s at 138 °C (open symbols) .....	41
Fig. 25	The orientation degree, calculated from (0 4 0) reflection, of iPP with different concentrations of $\beta$ -nucleating agent as a function of time during flow-induced crystallization with shear rate of 50 /s at 138 °C .....	42
Fig. 26	2D-WAXS patterns for sheared iPP nucleated with different concentrations of NJS at the end of given isothermal crystallization at 138 °C. For enhancing the scattering contrast a modification was applied here, i.e., by subtraction of the original pattern with the pattern just prior to the application of shear .....	43

Fig. 27	The long period of iPP with different concentrations of $\beta$ -nucleating agent as a function of time during flow-induced crystallization with shear rate of 50 /s at 138 °C .....	46
Fig. 28	Crystallization process for iPP with $\beta$ -nucleating particles under shear. (a) before application of shear, both the $\beta$ -nucleating agent particles and molecular chains were randomly distributed; (b) after applying shear, a lot of oriented $\alpha$ -row nuclei were formed near but not necessary on the surface of oriented anisotropic particles and unoriented isotropic particles; (c) The nuclei mainly grow into $\alpha$ -crystals, however, little $\beta$ -crystals may also be formed by the $\alpha$ to $\beta$ growth transition.....	47
Fig. 29	The overall crystallinity of Bpp2 as a function of time during shear-induced crystallization with different shear rates from 0 to 50 s <sup>-1</sup> at 138 °C .....	48
Fig. 30	The $\alpha$ -crystallinity of Bpp2 as a function of time during shear-induced crystallization with different shear rates from 0 to 50 s <sup>-1</sup> at 138 °C .....	50
Fig. 31	The $\beta$ -crystallinity of Bpp2 as a function of time during shear-induced crystallization with different shear rates from 0 to 50 s <sup>-1</sup> at 138 °C .....	51
Fig. 32	The development of long period for Bpp2 as a function of time during shear-induced crystallization with different shear rates from 0 to 50 s <sup>-1</sup> at 138 °C .....	52
Fig. 33	The $K_\beta$ value of Bpp2 as a function of time during shear-induced crystallization with different shear rates from 0 to 50 s <sup>-1</sup> at 138 °C .....	53
Fig. 34	The overall crystallinity of Bpp2 as a function of time during shear-induced crystallization under different temperatures ranging from 133 to 150 °C, shear rate = 50 s <sup>-1</sup> .....	54
Fig. 35	The $K_\beta$ value of Bpp2 as a function of time during shear-induced crystallization under different temperatures ranging from 133 to 150 °C, shear time = 5 s, shear rate = 50 s <sup>-1</sup> .....	55
Fig. 36	The $\alpha$ -crystallinity of Bpp2 as a function of time during shear-induced crystallization under different temperatures ranging from 133 to 150 °C, shear time = 5 s, shear rate = 50 s <sup>-1</sup> .....	56
Fig. 37	The $\beta$ -crystallinity of Bpp2 as a function of time during shear-induced crystallization under different temperatures ranging from 133 to 150 °C, shear time = 5 s, shear rate = 50 s <sup>-1</sup> .....	56
Fig. 38	Selected 2D-WAXS patterns for sheared Bpp2. For enhancing the scattering contrast a modification was applied here, i.e., by subtraction of the original pattern with the pattern just prior to the application of shear. (a) at the end of given isothermal crystallization at 143 °C; (b) at the solid state after isothermal crystallization at 143 °C; (c) at the solid state after isothermal crystallization at	

150 °C; (d) azimuthal plot of (3 0 0) reflection for 2D-WAXS pattern in (b); (e) azimuthal plot of (3 0 0) reflection for 2D-WAXS pattern in (c)..... 57

Fig. 39 The development of long period for Bpp2 as a function of time during shear-induced crystallization under different temperatures ranging from 133 to 143 °C, shear time = 5 s, shear rate =  $50\text{ s}^{-1}$  58

Fig. 40 Needle-like  $\beta$ -nucleating agent crystals in iPP melt (0.03 wt %) at 138 °C..... 59

Fig. 41 Selected WAXS patterns of Bpp2 after drawing at 138 °C. Drawing direction is vertical .... 60

Fig. 42 Selected WAXS patterns of iPP after drawing at 138 °C. Drawing direction is vertical..... 60

Fig. 43 Overall crystallinity over time for Bpp2 and iPP after drawing at 138 °C..... 61

Fig. 44 Selected SAXS pattern of Bpp2 after drawing. Drawing direction is vertical ..... 63

Fig. 45 Selected SAXS pattern of pure iPP after drawing. Drawing direction is vertical ..... 63

Fig. 46 Changes of long period with time ..... 64

Fig. 47 Changes of integrated scattered intensity in equatorial and meridional direction for Bpp2 64

Fig. 48 Overall and individual crystallinity over time for Bpp2 after drawing at 138 °C..... 65

Fig. 49 Schematic illustration of the skin-core morphology of injection-moulded sample [147].... 66

Fig. 50 Distributions of overall crystallinity (a),  $\alpha$ -crystallinity (b),  $\beta$ -crystallinity (c),  $\gamma$ -crystallinity (d), long period (e), lamellar thickness (f) and orientation degree (g) for iPP samples at position 1 within an injection-moulded iPP plate with different amount of nucleating agent: Pure iPP (■), Bpp1 (●), Bpp2 (▲) and Bpp3 (▼)..... 68

Fig. 51 Linear WAXS intensity profiles of Bpp2 at position 1 (a) and 2 (b), both taken at 0.22 mm away from the surface of the injection-moulded plates ..... 70

Fig. 52 Distributions of overall crystallinity (a),  $\alpha$ -crystallinity (b),  $\beta$ -crystallinity (c),  $\gamma$ -crystallinity (d), long period (e), lamellar thickness (f) and orientation degree (g) for injection-moulded Bpp2 sample at position 1 (■) and 2 (●) ..... 72

Fig. 53 WAXS patterns of undeformed injection-moulded iPP samples with different concentrations of  $\beta$ -nucleating agent, injection direction is vertical ..... 73

Fig. 54	SAXS patterns for undeformed injection-moulded iPP samples with different concentrations of $\beta$ -nucleating agent, injection direction is vertical .....	74
Fig. 55	Integrated intensity along meridian and equator for undeformed injection-moulded iPP as a function of $\beta$ -nucleating agent concentrations, $T = 90\text{ }^{\circ}\text{C}$ .....	75
Fig. 56	SAXS patterns of iPP with different amount of $\beta$ -nucleating agents at strain of 300%. Strain rate 0.1 mm/s. $T = 90\text{ }^{\circ}\text{C}$ , both injection and stretching directions are vertical, linear-scale intensity. 76	
Fig. 57	Integrated intensity along meridian and equator (according to equation 25 and 26 ) for deformed injection-moulded iPP with stretching rate of 0.1 mm/s and strain of 300% as a function of $\beta$ -nucleating agent concentrations, $T = 90\text{ }^{\circ}\text{C}$ .....	77
Fig. 58	The change of long period of deformed and undeformed injection-moulded samples as a function of $\beta$ -nucleating agent concentrations, $T = 90\text{ }^{\circ}\text{C}$ , stretching rate = 0.1 mm/s, taken from meridian.....	78
Fig. 59	WAXS patterns of iPP with different amount of $\beta$ -nucleating agents at strain of 300%, stretching rate = 0.1 mm/s, $T = 90\text{ }^{\circ}\text{C}$ .....	79
Fig. 60	Crystallinity of deformed and undeformed injection-moulded iPP samples as a function of $\beta$ -nucleating agent concentrations, $T = 90\text{ }^{\circ}\text{C}$ , stretching rate = 0.1 mm/s .....	79
Fig. 61	$K_{\beta}$ value of deformed and undeformed injection-moulded iPP samples as a function of $\beta$ -nucleating agent concentrations, $T = 90\text{ }^{\circ}\text{C}$ , stretching rate = 0.1 mm/s .....	80
Fig. 62	Crystallite size in the normal direction of the (1 1 0) reflection plane of deformed and undeformed injection-moulded iPP samples as a function of $\beta$ -nucleating agent concentrations, $T = 90\text{ }^{\circ}\text{C}$ , stretching rate = 0.1 mm/s .....	81
Fig. 63	Orientation parameter of the lattice plane (0 4 0) for deformed and undeformed injection-moulded iPP samples as a function of $\beta$ -nucleating agent concentrations, $T = 90\text{ }^{\circ}\text{C}$ , stretching rate = 0.1 mm/s.....	82
Fig. 64	True stress-strain curves of Bpp2 samples at different position. $T = 90\text{ }^{\circ}\text{C}$ , stretching rate = 0.1 mm/s.....	83
Fig. 65	Selected WAXS patterns of Bpp2 samples at position 1 and position 2 taken at different applied strains as indicated on the graph. $T = 90\text{ }^{\circ}\text{C}$ , stretching rate = 0.1 mm/s, stretching direction is vertical, linear-scale intensity without thickness correction. ....	84

Fig. 66	Circular-integrated WAXS profiles of Bpp2 samples at position 1 (a) and position 2 (b) taken at different applied strains as indicated on the graph. T = 90 °C, stretching rate = 0.1 mm/s.....	84
Fig. 67	Variation of overall crystallinity of Bpp2 samples at different positions with strains. T = 90°C, stretching rate = 0.1 mm/s .....	86
Fig. 68	Variation of the $K_{\beta}$ value of Bpp2 samples at different positions with strains (a) and selected circular-integrated WAXS profiles of Bpp2 sample at position 1 taken at different applied strains as indicated on the graph (b). T = 90°C, stretching rate = 0.1 mm/s .....	86
Fig. 69	Selected SAXS patterns of Bpp2 samples at position 1 and position 2 taken at different applied strains as indicated on the graph. T = 90 °C, stretching rate = 0.1 mm/s, stretching direction is vertical, log-scale intensity with thickness correction .....	87
Fig. 70	True stress-strain curves for Bpp2 samples at position 1, uniaxially drawn under stretching rate of 0.1 and 1.0 mm/s at temperature of 90 °C .....	89
Fig. 71	Selected WAXS patterns of Bpp2 samples at position 1, uniaxially drawn under stretching rate of 0.1 and 1.0 mm/s taken at different applied strains as indicated on the graph. T = 90 °C, stretching direction is vertical, linear-scale intensity without thickness correction .....	90
Fig. 72	WAXS intensity curves of Bpp2 samples at position 1 stretched to about 275% under stretching rate of 0.1 and 1.0 mm/s at 90 °C.....	91
Fig. 73	Selected SAXS patterns of Bpp2 samples at position 1, uniaxially drawn under stretching rate of 0.1 and 1.0 mm/s taken at different applied strains as indicated on the graph. T = 90 °C, stretching direction is vertical, log-scale intensity with thickness correction .....	92
Fig. 74	Illustration of data processing for tilted WAXS patterns: (a) original WAXS pattern with stretching direction being vertical, the main reflections are indicated on the graph; (b) selected WAXS pattern section from (a), this section reflects the variation of equatorial scattering with respect to stretching direction; (c) linear WAXS profile taken from the intensity in the equatorial direction of 2D WAXS pattern (indicated as broken line in (b)) .....	93
Fig. 75	True stress-strain curves of injection- and compression-moulded Bpp2 samples at given temperatures indicated on the graph. Stretching rate = 0.02 mm/s. ....	94
Fig. 76	Selected SAXS and WAXS patterns of compression-moulded Bpp2 samples taken at different applied strains as indicated on the graph. Stretching direction is vertical, T = 70 °C, stretching rate = 0.02 mm/s, with thickness correction, log-scale intensity for SAXS patterns, linear-scale intensity for WAXS patterns .....	95

Fig. 77	Selected SAXS and WAXS patterns of injection-moulded Bpp2 samples taken at different applied strains as indicated on the graph. Stretching direction is vertical, $T = 70\text{ }^{\circ}\text{C}$ , stretching rate = 0.02 mm/s, with thickness correction, log-scale intensity for SAXS patterns, linear-scale intensity for WAXS patterns .....	95
Fig. 78	Linear WAXS profiles of compression-moulded Bpp2 samples taken from the intensity in the equatorial direction of 2D WAXS patterns at different strains. $T = 70\text{ }^{\circ}\text{C}$ , stretching rate = 0.02 mm/s.....	97
Fig. 79	Linear WAXS profiles of injection-moulded Bpp2 samples taken from the intensity in the equatorial direction of 2D WAXS patterns at different strains. $T = 70\text{ }^{\circ}\text{C}$ , stretching rate = 0.02 mm/s. 98	
Fig. 80	Selected SAXS and WAXS patterns of injection-moulded Bpp2 samples taken at different applied strains as indicated on the graph. Stretching direction is vertical, $T = 110\text{ }^{\circ}\text{C}$ , stretching rate = 0.02 mm/s, with thickness correction, log-scale intensity for SAXS patterns, linear-scale intensity for WAXS patterns. ....	99
Fig. 81	The change of meridional long period of injection-moulded Bpp2 samples stretched at $110\text{ }^{\circ}\text{C}$ as a function of strain. Stretching rate = 0.02 mm/s. ....	99
Fig. 82	Linear WAXS profiles of injection-moulded Bpp2 samples taken from the intensity in the equatorial direction of 2D WAXS patterns at different strains. $T = 110\text{ }^{\circ}\text{C}$ , stretching rate = 0.02 mm/s.	100
Fig. 83	Selected SAXS and WAXS patterns of compress-moulded Bpp2 samples taken at different applied strains as indicated on the graph. Stretching direction is vertical, $T = 110\text{ }^{\circ}\text{C}$ , stretching rate = 0.12 mm/s, with thickness correction, log-scale intensity for SAXS patterns, linear-scale intensity for WAXS patterns. ....	101
Fig. 84	Linear WAXS profiles of compression-moulded Bpp2 samples taken from the intensity in the equatorial direction of 2D WAXS patterns at different strains. $T = 110\text{ }^{\circ}\text{C}$ , stretching rate = 0.12 mm/s.....	101

## List of tables

Tab. 1	$\beta$ -nucleated iPP used in this study.....	21
Tab. 2	Kinetics parameters for iPP samples containing different concentrations of $\beta$ -nucleating agent during isothermal crystallization .....	34
Tab. 3	Crystallization states at 80 °C for iPP samples containing different concentrations of $\beta$ -nucleating agent. Firstly, the samples were isothermally crystallized at 138 °C for 280 s and then cooled to 80 °C, at which the crystallization was basically complete.....	35
Tab. 4	Kinetics parameters for Bpp2 during isothermal shear-induced crystallization with shear rates ranging from 0 to 50 s <sup>-1</sup> .....	49
Tab. 5	Crystallization states at 80 °C for Bpp2 after various shear steps. Firstly, the samples were isothermally crystallized at 138 °C for 280 s and then cooled to 80°C, at which the crystallization was basically complete. ....	51
Tab. 6	Kinetics parameters for Bpp2 during isothermal sheared-induced crystallization with shear rate of 50 s <sup>-1</sup> at different temperatures.....	54
Tab. 7	Crystallization states at 80 °C for Bpp2 after shearing the sample for 5 s with a shear rate of 50 s <sup>-1</sup> at various temperatures. Firstly, the samples were isothermally crystallized at a given temperature for 280 s and then cooled to 80°C, where the crystallization was basically complete. ....	57



## **Eidesstattliche Erklärung**

Hiermit versichere ich, dass ich die vorliegende Arbeit ohne unzulässige Hilfe Dritter und ohne Benutzung anderer als der angegebenen Hilfsmittel angefertigt habe; die aus fremden Quellen direkt oder indirekt übernommenen Gedanken sind als solche kenntlich gemacht.

Weitere Personen waren an der geistigen Herstellung der vorliegenden Arbeit nicht beteiligt. Insbesondere habe ich nicht die Hilfe eines kommerziellen Promotionsberaters in Anspruch genommen. Dritte haben von mir keine geldwerten Leistungen für Arbeiten erhalten, die in Zusammenhang mit dem Inhalt der vorgelegten Dissertation stehen.

Die Arbeit wurde bisher weder im Inland noch im Ausland in gleicher oder ähnlicher Form einer anderen Prüfungsbehörde vorgelegt und ist auch noch nicht veröffentlicht worden.

Die Promotionsordnung wird anerkannt.

Dresden, den 25.09.2014

